PRE- AND POST-BUCKLING ANALYSIS OF NANOBEAMS

A THESIS SUBMITTED TO
THE GRADUATE SCHOOL OF ENGINEERING AND SCIENCE
OF BILKENT UNIVERSITY
IN PARTIAL FULFILLMENT OF THE REQUIREMENTS FOR
THE DEGREE OF
MASTER OF SCIENCE
IN
MECHANICAL ENGINEERING

By
Onur Vardar
February 2019

PRE- AND POST-BUCKLING ANALYSIS OF NANOBEAMS
By Onur Vardar
February 2019

We certify that we have read this thesis and that in our opinion it is fully adequate, in scope and in quality, as a thesis for the degree of Master of Science.

Ali Javili (Advisor)

Mehmet Selim Hanay

Ercan Gürses

Approved for the Graduate School of Engineering and Science:

Ezhan Karaşan
Director of the Graduate School

ABSTRACT

PRE- AND POST-BUCKLING ANALYSIS OF NANOBEAMS

Onur Vardar
M.S. in Mechanical Engineering
Advisor: Ali Javili
February 2019

Interest in nanobeams is increasing as their application areas widen and new properties are discovered. These structures exhibit size dependent intrinsic properties that are absent in macroscale. This requires employment of new material models as bulk models by themself are not sufficient to describe the physics unless one considers the domain as a composite material, which is undesirable. In this work it was confirmed that incorporation of surface elasticity results in a good match with experiments. Moreover it was shown that due to lack of out-of-plane shear support of surfaces and curves, Euler beam assumptions fail for numerical implementations when the beam size reduces. This phenomenon was shown to be a severe drawback for curved energetic domains with a still noticable effect for surface energies. A geometrically nonlinear buckling model is proposed based on linear elastic material model. It is implemented in an ordinary differential equations solver and the solutions were confirmed to meet the finite element method (FEM) results to a very high degree. The theory is integrated with surface layers in which its accuracy was confirmed when compared with FEM results.

Keywords: Bistable beam, Snap-through, Buckling, Nanobeam, Surface effect.

ÖZET

NANOKİRİŞLERİN BURKULMA ÖNCESİ VE SONRASI ANALİZİ

Onur Vardar
Makine Mühendisliği, Yüksek Lisans
Tez Danışmanı: Ali Javili
Şubat 2019

Nanokirişlerin yeni özellikleri keşfedilip uygulama alanları çoğaldıkça üzerlerine yapılan araştırmalar yoğunlaşmaktadır. Bahsedilen yapılar makro ölçekte gözlemlenemeyen, boyutlarına bağlı değişken özellikler göstermektedirler. Bu durumda malzeme çoklu kütle bileşenlerinden oluşan bir kompozit şeklinde modellenmediği müddetçe, ki bu da istenilen bir durum değildir, bahsedilen değişken özellikler ancak yeni bir modelle gözlemlenebilir. Bu tezde yüzey esnekliği modelinin var olan kütlelere eklenmesinin deneylerle uyuşan sonuçlar çıkardığı gösterilmiştir. Ayrıca, bahsi geçen yüzeylerin ve çizgilerin düzlem dışı kesme dayanımı olmadığından Euler kirişi varsayımlarının küçülen boyutlar için hesapsal sonuçlarda geçersizleştiği gösterilmiştir. Bu durum çizgiler için ciddi derecede etkili olmakla birlikte yüzeylerde de etkisini görmek mümkündür. Kirişler için malzeme modeli doğrusal olan, geometrisi doğrusal olmayan bir burkulma formülasyonu sunulmuştur. Bu formülasyon sayısal olarak bir diferansiyel denklem çözücüye uygulanmıştır ve sonuçların sonlu elemanlar yöntemiyle elde edilen bulgularla oldukça yakın olduğu gösterilmiştir. Son olarak yüzey etkilerinin de hacme eklenmesiyle elde edilen sayısal sonuçların doğruluğu sonlu elemanlarla kıyaslanıp onaylanmıştır.

Anahtar sözcükler: İkikararlı kiriş, Burkulma, Nanokiriş, Yüzey etkisi.

Acknowledgement

First and foremost, I would like to thank Dr. Ali Javili for his unprecedented patience, support and positive attitude towards me through my journey. Without his expert opinions and guidance, I would have had countless difficulties many of which would be hard to overcome.

I would also like to acknowledge my dear friends Hande, Muhammet and Hammam for keeping my spirits up during the hardship we all endured together. Soheil Firooz also deserves a place here for generously offering me his technical expertise whenever I needed while preparing this thesis.

Last but not least I want to express my gratitudes to my family for their unconditional support. My father, mother, sister and my beloved niece Doğa: I feel blessed for having such a joyful and loving family.

I dedicate this thesis to my late cousin, Mert.

Contents

List of Figures

List of Tables

Nomenclature

$\boldsymbol{\varphi}$	Deformation map
$\boldsymbol{E}$	Green-Lagrange strain tensor
$\boldsymbol{F}$	Deformation gradient
$\boldsymbol{f}$	ınverse of deformation gradient
$\boldsymbol{I}$	Identity map in undeformed configurations
$\boldsymbol{i}$	Identity map in deformed configurations
$\boldsymbol{N}$	Outward unit normal vector to bulk
$\mathcal{B}_0$	3D bulk domain
$\mathcal{C}_j$	1D curve domains
$\mathcal{L}$	Lagrangian
$\mathcal{S}_i$	2D surface domains
ΔL	Length shortening of a beam
$\widehat{\boldsymbol{\varphi}}$	Restriction of deformation map to surface
$\widehat{\boldsymbol{C}}$	Surface right Cauchy-Green deformation tensor
$\widehat{\boldsymbol{F}}$	Surface projection of deformation gradient in current configuration
$\widehat{\boldsymbol{f}}$	Surface projection of the inverse of deformation gradient in deformed configuration

$\widehat{\boldsymbol{I}}$	Projection of identity map onto surface in reference configuration
$\widehat{\boldsymbol{i}}$	Projection of identity map onto surface in current configuration
$\widehat{\boldsymbol{N}}$	Outward unit normal vector to surface
$\widehat{\boldsymbol{P}}$	Surface Piola stress tensors
$\widehat{\boldsymbol{S}}$	Surface Piola-Kirchoff stress tensor
$\widehat{\lambda}$	First surface Lamé parameter
$\widehat{\mu}$	Second surface Lamé parameter
$\widehat{\mathbb{A}}$	Fourth order surface Piola stress elasticity tensor
$\widehat{\mathbb{C}}$	Fourth order surface Cauchy-Green stress elasticity tensor
$\widehat{A}$	Perimeter of the cross section of a beam
$\widehat{E}$	Young's modulus of surface
$\widehat{G}$	Shear modulus of surface
$\widehat{I}$	Second area moment of surface (cross-sectional)
$\widehat{J}$	Surface Jacobian of deformation gradient
κ	Curvature of a beam
Λ	Stretch of a beam
λ	First bulk Lamé parameter
μ	Second bulk Lamé parameter
ν	Poisson's ratio (bulk)
$\widetilde{\boldsymbol{\varphi}}$	Restriction of deformation map to curve
$\widetilde{\boldsymbol{C}}$	Curve right Cauchy-Green deformation tensor
$\widetilde{\boldsymbol{F}}$	Curve projection of deformation gradient in current configuration

$\widetilde{\boldsymbol{f}}$ Curve projection of the inverse of deformation gradient in deformed configuration

$\widetilde{\boldsymbol{I}}$ Projection of identity map onto curve in reference configuration

$\widetilde{\boldsymbol{i}}$ Projection of identity map onto curve in current configuration

$\widetilde{\boldsymbol{N}}$ Tangent unit normal vector to curve

$\widetilde{\boldsymbol{P}}$ Curve Piola stress tensors

$\widetilde{\boldsymbol{S}}$ Curve Piola-Kirchoff stress tensor

$\widetilde{\mu}$ Curve Lamé parameter

$\widetilde{\mathbb{A}}$ Fourth order curve Piola stress elasticity tensor

$\widetilde{\mathbb{C}}$ Fourth order curve Cauchy-Green stress elasticity tensor

$\widetilde{E}$ Young's modulus of curve

$\widetilde{I}$ Second area moment of curve (cross-sectional)

$\widetilde{J}$ Curve Jacobian of deformation gradient

$\mathbb{A}$ Fourth order Piola stress bulk elasticity tensor

$\mathbb{C}$ Fourth order Cauchy-Green bulk elasticity tensor

A Cross sectional area of a beam

C Error correction factor for Timoshenko beams

E Young's modulus of bulk

E_κ Total bending energy

E_Λ Total stretch energy

F Transverse force acting on a beam

G Shear modulus of bulk

H	Height of beam at transverse force application point
H_0	Height of beam at point of interest for first mode of buckling
I	Second area moment of bulk (cross-sectional)
J	Jacobian of deformation gradient
K_γ	Shear stiffnes of a beam
K_κ	Bending stiffnes of a beam (Chapter 3)
K_Λ	Stretch stiffnes of a beam
K_θ	Bending stiffnes of a beam (Chapter 4)
L	Undeformed length of a beam
P	End shortening force
R	Shear stiffnes to bending stiffness ratio
$\boldsymbol{C}$	Right Cauchy-Green deformation tensor
$\boldsymbol{P}$	Piola stress tensor
$\boldsymbol{S}$	Piola-Kirchoff stress tensor

Chapter 1

Introduction

This thesis incorporates surface and curve energy models in a finite element setting to study bending and buckling behaviors of nanobeams and nanowires. Nanobeams and nanowires are slender structures that typically have at least one sub-micron dimension. These type of structures have a wide range of use, such as nano-electromechanical systems that are used to sense nanoparticles with a high degree of accuracy [1]. The small sized nature of these devices brings along some other interesting properties. The work presented here aims to incorporate the size dependent behavior into the continuum mechanics framework and implement it in a numerical setting that is the Finite Element Method (FEM).

The mechanical properties of nanowires are size dependent and this fact has been well established in the past years [2, 3]. Various explanations for this phenomenon are proposed. This behavior is generally attributed to the existence of a layer of oxidation or some other form of coating around the beam. Since these layers have an average thickness that is not dependent on the diameter of the nanowires, they can be formulated with surface parameters. In this work, the surface energy formulation in a continuum mechanical framework is numerically implemented and the corresponding results are compared to experimental values from the literature.

Similar to bending of nanowires, buckling in nanobeams have become a frequent focus of research. The post buckling behavior of a beam had not been a focus of interest from an engineering standpoint since it is generally deemed a situation that has to be avoided. Though, with the invention of new production techniques and growing interest of study around buckling in nano scale, this situation is gradually changing. For instance in [4], a way to use double clamped buckled nanobeams as a non-volatile mechanical memory is suggested. Likewise, [5] discusses a micromechanical buckled beam that is forced to switch between its bistable modes through the use of an actuator that applies a transverse force at the middle of the beam. These research areas neccessitate inclusion of size dependent behavior of such structures.

1.1 Outline

The structure of the thesis is divided into three parts. In chapter 2, the continuum mechanics formulation of surface and curve energies are presented. The mathematical conventions and notations are briefly defined in the initial stage followed with the general variation calculations of bulk, surface and curve energies. The equivalent set of partial differential equations are derived as a result of this process. Then the specific energy models that are incorporated in the rest of the thesis are presented. The remaining part of the chapter explains the implementation of the theory in a finite element setting.

The chapter 2 begins by reminding briefly Euler and Timoshenko beam theories. The analytical equivalent stiffness terms are derived when taking surface and curve effects into consideration. Then these analytical results are compared to values obtained from finite element simulations and published experiments. The numerical results can be categorized into two groups: one assuming the validity of Euler beam theory and the other Timoshenko beam theory. A discussion on the validity of Euler beam assumptions are given.

Chapter 4 deals with bi-stable beams and buckling where an analytical model

for buckled beams that are subjected to transverse forces is proposed. Comparison of this model with similar studies found in the literature are discussed. Similar to beam bending study, equivalent stiffness terms are incorporated into the equation to take surface effects into account. The snap-through phenomenon on silicon nano beams are solved with the analytical model and it was found that the solutions match nonlinear finite elements results to a very high degree. In the last part of this chapter transformation of bending and stretch energies during the snap through process are presented for a wide range of compression amounts.

Chapter 2

Governing Equations and Material Modeling

2.1 Mathematical notations

The theory of continuum mechanics heavily revolves around the notion of tensors and a clear convention is an important aspect of the subject. One important notation is Einstein's summation convention. It relieves the theory from an encumbering baggage that is the summation symbol Σ in many cases. In its simplest form, it states that the summation symbol shall be dropped for any composite term in which an index symbol appears exactly twice. Composite term in this context is used to refer to a mathematical expression that consists of algebraic operations of terms, barring summation and subtraction. A simple example for this would be

$$a_i b_i = \sum_{i=1}^{N} a_i b_i = a_1 b_1 + a_2 b_2 + \cdots + a_N b_N \tag{2.1}$$

In this thesis, the tensors used to describe the physical phenomena are exclusively confined to zeroth, first, second and fourth orders. So we introduce them accordingly. One should note that the notation aims to differentiate between

these terms by going from lower case to upper case letters along with a change of calligraphic style. The notation is

$$\begin{aligned} \phi, \varphi &\rightarrow \text{scalar (lower case)} \\ \boldsymbol{u}, \boldsymbol{v} &\rightarrow \text{first order tensor (bold lower case)} \\ \boldsymbol{A}, \boldsymbol{B} &\rightarrow \text{second order tensor (bold upper case)} \\ \mathbb{C} &\rightarrow \text{fourth order tensor (calligraphic upper case).} \end{aligned} \tag{2.2}$$

The scalar product $\{\cdot\}$ of first order and second order tensors are defined as

$$\boldsymbol{u} \cdot \boldsymbol{v} = u_i v_i, \qquad (\boldsymbol{A} \cdot \boldsymbol{B})_{ij} = A_{ik} B_{kj}, \tag{2.3}$$

whereas the double contraction $\{:\}$ is defined with

$$\boldsymbol{A} : \boldsymbol{B} = A_{ij} B_{ij}, \qquad (\mathbb{C} \cdot \boldsymbol{B})_{ij} = C_{ijkl} B_{kl}. \tag{2.4}$$

The dyadic product $\{\otimes\}$ of two first or second order tensors are

$$(\boldsymbol{u} \otimes \boldsymbol{v})_{ij} = u_i v_j, \qquad (\boldsymbol{A} \otimes \boldsymbol{B})_{ijkl} = A_{ij} B_{kl} \tag{2.5}$$

and the non-standard dyadic products $\{\,\overline{\otimes}\,\}$ and $\{\,\underline{\otimes}\,\}$ of two second order tensors are

$$(\boldsymbol{A} \,\overline{\otimes}\, \boldsymbol{B})_{ijkl} = A_{ik} B_{jl}, \qquad (\boldsymbol{A} \,\underline{\otimes}\, \boldsymbol{B})_{ijkl} = A_{il} B_{jk}. \tag{2.6}$$

2.2 Kinematics

In this thesis the notation is mainly adopted from [6, 7, 8], with slight modifications. $\boldsymbol{X}$ is used to describe the reference material coordinates inside the domain $\mathcal{B}_0 \subset \mathbb{R}^3$. The domain $\mathcal{B}_0$ is a 3D smooth manifold with boundary. It is assumed here that boundary of $\mathcal{B}_0$, namely $\partial\mathcal{B}_0$, is a 2D piecewise smooth manifold without boundary which will be called a surface. The finitely many 1-dimensional parts of the surface which break the smoothness of the boundary $\partial\mathcal{B}_0$ are regarded as curves with the notation $\mathcal{C}_j$ whereas the smooth subsets of the surface are denoted

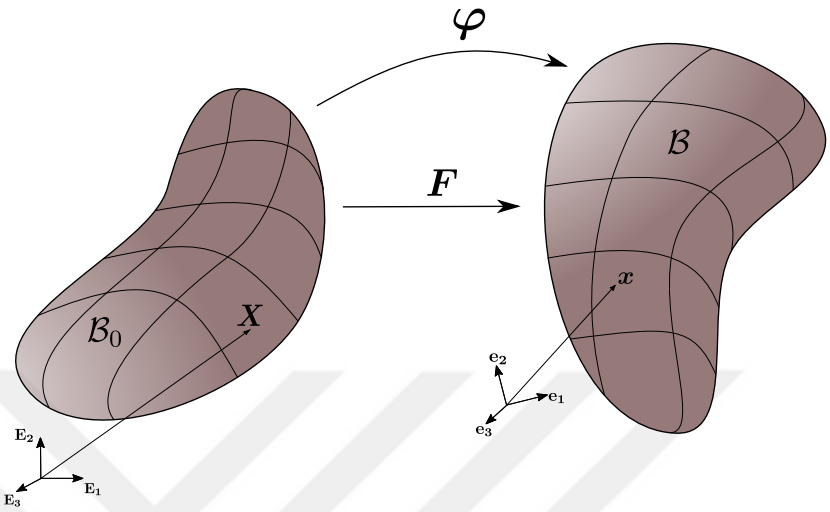

Figure 2.1: The map $\boldsymbol{\varphi}$ along with the deformation gradient $\boldsymbol{F}$

as $\mathcal{S}_i$. Different indices i and j are used for surfaces and curves in order to make the distinction that their numbers in general are different.

Here, we assume that the reference domain is mapped into the deformed state by a function $\boldsymbol{\varphi} : \mathcal{B}_0 \to \mathcal{B} \subset \mathbb{R}^3$, $\boldsymbol{X} \mapsto \boldsymbol{\varphi}(\boldsymbol{X}) = \boldsymbol{x}$ and that $\boldsymbol{\varphi}$ along with its inverse map $\boldsymbol{\varphi}^{-1}$ are continuously differentiable. The derivative of the map $\boldsymbol{\varphi}$ at a point $\boldsymbol{X} \in \mathcal{B}_0$ is denoted as $\boldsymbol{F}(\boldsymbol{X}) := \nabla\boldsymbol{\varphi}$. Then the deformation gradient tensor is $\boldsymbol{F} : \mathcal{B}_0 \to L(\mathbb{R}^3, \mathbb{R}^3)$.

All the dependent variables such as vector fields, tensor fields etc. that are defined on the domains $\mathcal{B}_0$ or $\mathcal{B}$ are referred as *bulk* quantities. In contrast, the quantities that admit $\mathcal{S}_i$ as their domains are associated with the term *surface* and the quantities that admit $\mathcal{C}_i$ as their domains are associated with the term *curve*. The domain of such objects might also be deduced from the independent variables: usage of $\boldsymbol{X}$ should emphasize that the domain of the associated mapping is the bulk, whereas $\widehat{\boldsymbol{X}}$ and $\widetilde{\boldsymbol{X}}$ indicate that the related domains are the surface and curve, respectively.

The restriction of the deformation mapping to the *surface* and the *curve* are defined as

$$\widehat{\boldsymbol{\varphi}} := \boldsymbol{\varphi}|_{\mathcal{S}_i}, \qquad \widetilde{\boldsymbol{\varphi}} := \boldsymbol{\varphi}|_{\mathcal{C}_j}. \tag{2.7}$$

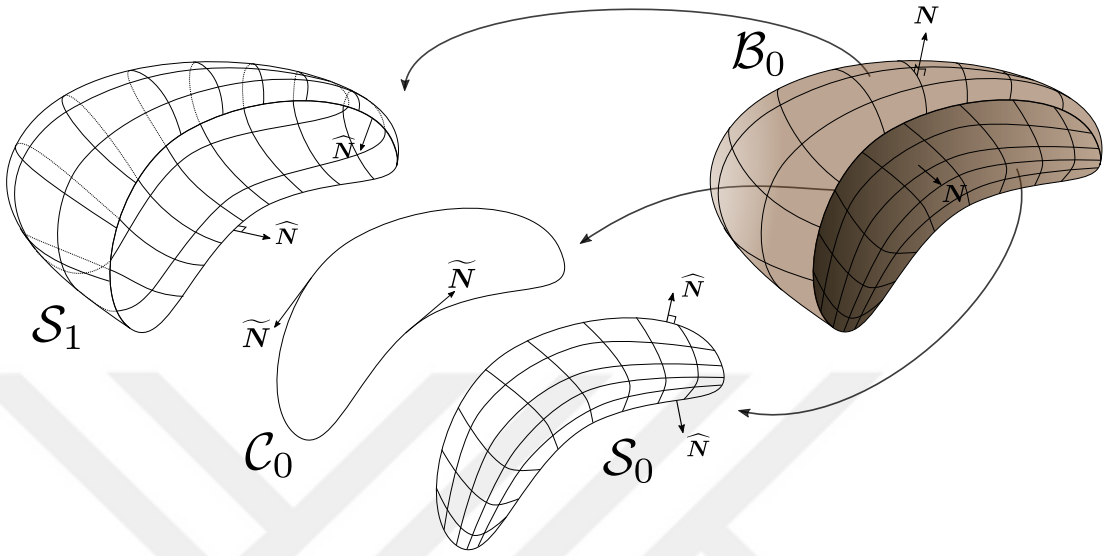

Figure 2.2: Illustration of normals and tangents

The bulk deformation gradient is defined simply as the derivative of the map $\boldsymbol{\varphi}$. Before introducing the surface and curve gradients $\widehat{\text{Grad}}\,\{\bullet\}$ and $\widetilde{\text{Grad}}\,\{\bullet\}$, we define the surface projection tensors $\widehat{\boldsymbol{I}}$, $\widehat{\boldsymbol{i}}$ and the curve projection tensors $\widetilde{\boldsymbol{I}}$, $\widetilde{\boldsymbol{i}}$. Projection tensors for the surfaces and curves are defined as

$$\begin{aligned} \widehat{\boldsymbol{I}} &:= \boldsymbol{I} - \boldsymbol{N} \otimes \boldsymbol{N}, \qquad & \widehat{\boldsymbol{i}} &:= \boldsymbol{i} - \boldsymbol{n} \otimes \boldsymbol{n}, \\ \widetilde{\boldsymbol{I}} &:= \widetilde{\boldsymbol{N}} \otimes \widetilde{\boldsymbol{N}}, & \widetilde{\boldsymbol{i}} &:= \widetilde{\boldsymbol{n}} \otimes \widetilde{\boldsymbol{n}}. \end{aligned} \tag{2.8}$$

In the equation, $\boldsymbol{N}$ and $\boldsymbol{n}$ are the unit normal vectors on the surfaces of the undeformed and deformed states while $\widetilde{\boldsymbol{N}}$ and $\widetilde{\boldsymbol{n}}$ are the unit tangent vectors to the curves of the undeformed and deformed states, respectively. Also $\boldsymbol{I}$ and $\boldsymbol{i}$ are identity transformations in the reference and deformed configurations. We also define $\widehat{\boldsymbol{N}}$ as the normal to a surface at its boundary, as seen in Fig. 2.2. The surface and curve deformation tensors are

$$\begin{aligned} \widehat{\boldsymbol{F}}\,(\widehat{\boldsymbol{X}},t) &:= \widehat{\text{Grad}}\,\widehat{\boldsymbol{\varphi}}\,(\widehat{\boldsymbol{X}},t) \;=\; \boldsymbol{F}\cdot\widehat{\boldsymbol{I}}, \\ \widetilde{\boldsymbol{F}}\,(\widetilde{\boldsymbol{X}},t) &:= \widetilde{\text{Grad}}\,\widetilde{\boldsymbol{\varphi}}\,(\widetilde{\boldsymbol{X}},t) \;=\; \boldsymbol{F}\;\cdot\widetilde{\boldsymbol{I}}. \end{aligned} \tag{2.9}$$

Since the projection tensors have non-empty null spaces, these tensors are rank deficient so they lack invertibility. However, one can define $\widehat{\boldsymbol{f}} := \boldsymbol{F}^{-1}\cdot\widehat{\boldsymbol{i}}$ and $\widetilde{\boldsymbol{f}} := \boldsymbol{F}^{-1}\cdot\widetilde{\boldsymbol{i}}$ which satisfy the conditions $\widehat{\boldsymbol{F}}\cdot\widehat{\boldsymbol{f}} = \widehat{\boldsymbol{i}}$, $\widehat{\boldsymbol{f}}\cdot\widehat{\boldsymbol{F}} = \widehat{\boldsymbol{I}}$ and $\widetilde{\boldsymbol{F}}\cdot\widetilde{\boldsymbol{f}} =$

$\widetilde{\boldsymbol{i}}$, $\widehat{\boldsymbol{f}} \cdot \widetilde{\boldsymbol{F}} = \widetilde{\boldsymbol{I}}$. As usual, $\boldsymbol{f}$ is defined as the inverse of $\boldsymbol{F}$. See [9] for further details.

The determinant -or the Jacobians- of a linear mapping whose domain is the tangent space at a point on the volume, surface or curve is defined as

$$\begin{aligned}
\operatorname{Det}\{\bullet\} &:= \frac{[\{\bullet\}\cdot\boldsymbol{V_1}]\cdot\left[[\{\bullet\}\cdot\boldsymbol{V_2}]\times[\{\bullet\}\cdot\boldsymbol{V_3}]\right]}{\boldsymbol{V_1}\cdot[\boldsymbol{V_2}\times\boldsymbol{V_3}]}, && \boldsymbol{V_1},\boldsymbol{V_2},\boldsymbol{V_3} \text{ linearly independent}\\
\widehat{\operatorname{Det}}\{\widehat{\bullet}\} &:= \frac{\|\,[\{\widehat{\bullet}\}\cdot\boldsymbol{V_1}]\times[\{\widehat{\bullet}\}\cdot\boldsymbol{V_2}]\,\|}{\|\boldsymbol{V_1}\times\boldsymbol{V_2}\|}, && \boldsymbol{V_1},\boldsymbol{V_2} \text{ linearly independent}\\
\widetilde{\operatorname{Det}}\{\widetilde{\bullet}\} &:= \frac{\|\{\bullet\}\cdot\boldsymbol{V_1}\|}{\|\boldsymbol{V_1}\|}.
\end{aligned} \tag{2.10}$$

Here, the linearly independent vectors are assumed to lie on the respective tangent spaces. As a particular case, J, $\widehat{J}$ and $\widetilde{J}$ are used to denote the Jacobians $\operatorname{Det}\boldsymbol{F}$, $\widehat{\operatorname{Det}}\,\widehat{\boldsymbol{F}}$ and $\widetilde{\operatorname{Det}}\,\widetilde{\boldsymbol{F}}$, respectively.

2.3 Minimum energy principle

In this section, the time independent governing equations of balance laws in localized form are retrieved from the minimum energy principle.

Consider a generalized form of internal energy ψ^{int} which depends not only on the bulk, but also on the boundary surface and some curves that lie on the boundary. Then, in general the total energy can be written in the form

$$\begin{aligned}
\psi^{tot} &= \psi^{ext} + \psi^{int}\\
&= \psi^{ext} + \int_{\mathcal{B}_0}\psi(\boldsymbol{F})\,\mathrm{d}V + \sum_i\int_{\mathcal{S}_i}\widehat{\psi}(\widehat{\boldsymbol{F}})\,\mathrm{d}A + \sum_j\int_{\mathcal{C}_j}\widetilde{\psi}(\widetilde{\boldsymbol{F}})\,\mathrm{d}L.
\end{aligned} \tag{2.11}$$

Here, the bulk form $\psi(\boldsymbol{F})$ and its surface and curve counterparts are assumed instead of the more general form $\psi(\boldsymbol{\varphi},\boldsymbol{F})$. This restricted assumption is considered in order to disregard the effects of external sources of energy such as gravity

or electric potential fields (for the bulk) that contribute to the energy density depending only on the displacement of the material point for the time being: such terms are assumed to be included in ψ^{ext}.

Seeking the solution of a mechanical problem where there exists a functional ψ^{tot} describing the total energy of the system in terms of the displacement field $\boldsymbol{\varphi}$ is equivalent to finding the global minimizer of such a functional. The total energy functional ψ^{tot} is assumed to depend only on $\boldsymbol{\varphi}$. Hence its first variation $\delta\psi^{tot}(\boldsymbol{\varphi}, \delta\boldsymbol{\varphi})$ is necessarily equal to 0 for any admissible increment $\delta\boldsymbol{\varphi}$ of $\boldsymbol{\varphi}$. Writing the total energy explicitly

$$\begin{aligned}\psi^{tot} &= \psi^{ext} + \psi^{int} \\ &= \psi^{ext} + \psi_b^{int} + \psi_s^{int} + \psi_c^{int} \\ &= \psi^{ext} + \int_{\mathcal{B}_0} \psi\left(\boldsymbol{F}\right) \mathrm{d}V + \sum_i \int_{\mathcal{S}_i} \widehat{\psi}\left(\widehat{\boldsymbol{F}}\right) \mathrm{d}A + \sum_j \int_{\mathcal{C}_j} \widetilde{\psi}\left(\widetilde{\boldsymbol{F}}\right) \mathrm{d}L\end{aligned} \tag{2.12}$$

implies that the necessary condition

$$\begin{aligned}\delta\psi^{tot}(\boldsymbol{\varphi}, \delta\boldsymbol{\varphi}) &= \delta\psi^{ext}(\boldsymbol{\varphi}, \delta\boldsymbol{\varphi}) + \delta\psi_b^{int}(\boldsymbol{\varphi}, \delta\boldsymbol{\varphi}) + \delta\psi_s^{int}(\boldsymbol{\varphi}, \delta\boldsymbol{\varphi}) + \delta\psi_c^{int}(\boldsymbol{\varphi}, \delta\boldsymbol{\varphi}) \\ &= \delta\psi^{ext}(\boldsymbol{\varphi}, \delta\boldsymbol{\varphi}) + \frac{\delta\psi_b^{int}}{\delta\boldsymbol{\varphi}} + \frac{\delta\psi_s^{int}}{\delta\widehat{\boldsymbol{\varphi}}} + \frac{\delta\psi_c^{int}}{\delta\widetilde{\boldsymbol{\varphi}}} \\ &= 0\end{aligned} \tag{2.13}$$

holds for every appropriate $\delta\boldsymbol{\varphi}$, since $\boldsymbol{\varphi}$ reduces to the appropriate terms according to (2.7).

$$\delta\psi^{int}(\boldsymbol{\varphi}, \delta\boldsymbol{\varphi}) = \underbrace{\frac{\delta}{\delta\boldsymbol{\varphi}} \int_{\mathcal{B}_0} \psi\left(\boldsymbol{F}\right) \mathrm{d}V}_{\text{bulk term}} + \sum_i \underbrace{\frac{\delta}{\delta\widehat{\boldsymbol{\varphi}}} \int_{\mathcal{S}_i} \widehat{\psi}\left(\widehat{\boldsymbol{F}}\right) \mathrm{d}A}_{\text{surface terms}} + \sum_j \underbrace{\frac{\delta}{\delta\widetilde{\boldsymbol{\varphi}}} \int_{\mathcal{C}_j} \widetilde{\psi}\left(\widetilde{\boldsymbol{F}}\right) \mathrm{d}L}_{\text{curve terms}} \tag{2.14}$$

Each one of the bulk, surface and curve terms are studied individually in the following sections.

2.3.1 Bulk energy variation

We now turn our attention to bulk energy variation. The variation is equal to

$$\frac{\delta}{\delta\boldsymbol{\varphi}}\int_{\mathcal{B}_0}\psi\left(\boldsymbol{F}\right)\mathrm{d}V \;=\; \int_{\mathcal{B}_0}\underbrace{\frac{\partial\psi}{\partial\boldsymbol{F}}}_{\boldsymbol{P}}:\delta\boldsymbol{F}\,\mathrm{d}V \;=\; \int_{\mathcal{B}_0}\boldsymbol{P}:\delta\boldsymbol{F}\,\mathrm{d}V. \tag{2.15}$$

In order to proceed further, one has to write the term $\delta\boldsymbol{F}$ in terms of $\delta\boldsymbol{\varphi}$. One might argue that since the gradient is a linear operator and that $\boldsymbol{F}=\mathrm{Grad}\,\boldsymbol{\varphi}$, it is possible to write $\boldsymbol{F}+\delta\boldsymbol{F}=\mathrm{Grad}\left(\boldsymbol{\varphi}+\delta\boldsymbol{\varphi}\right)$ which implies that $\delta\boldsymbol{F}=\mathrm{Grad}\,\delta\boldsymbol{\varphi}$. Then one can write

$$\int_{\mathcal{B}_0}\boldsymbol{P}:\delta\boldsymbol{F}\,\mathrm{d}V=\int_{\mathcal{B}_0}\boldsymbol{P}:\mathrm{Grad}\,\delta\boldsymbol{\varphi}\mathrm{d}V. \tag{2.16}$$

Integration by parts implies

$$\mathrm{Div}\{\delta\boldsymbol{\varphi}\cdot\boldsymbol{P}\}=\delta\boldsymbol{\varphi}\cdot\mathrm{Div}\boldsymbol{P}+\boldsymbol{P}:\mathrm{Grad}\boldsymbol{\varphi} \tag{2.17}$$

which then can be substituted into the equation (2.15), with the result being

$$\begin{aligned}\int_{\mathcal{B}_0}\boldsymbol{P}:\mathrm{Grad}\,\delta\boldsymbol{\varphi}\,\mathrm{d}V&=\int_{\mathcal{B}_0}\mathrm{Div}\{\delta\boldsymbol{\varphi}\cdot\boldsymbol{P}\}\,\mathrm{d}V \;-\int_{\mathcal{B}_0}\delta\boldsymbol{\varphi}\cdot\mathrm{Div}\boldsymbol{P}\,\mathrm{d}V\\&=\int_{\partial\mathcal{B}_0}\delta\boldsymbol{\varphi}\cdot\boldsymbol{P}\cdot\boldsymbol{N}\,\mathrm{d}A \;-\int_{\mathcal{B}_0}\delta\boldsymbol{\varphi}\cdot\mathrm{Div}\boldsymbol{P}\,\mathrm{d}V\\&=\sum_i\int_{\mathcal{S}_i}\delta\boldsymbol{\varphi}\cdot\boldsymbol{P}\cdot\boldsymbol{N}\,\mathrm{d}A \;-\int_{\mathcal{B}_0}\delta\boldsymbol{\varphi}\cdot\mathrm{Div}\boldsymbol{P}\,\mathrm{d}V\end{aligned} \tag{2.18}$$

due to Gauss' Theorem (where $\boldsymbol{N}$ is the outward unit vector from the surface at the reference configuration).

2.3.2 Surface energy variation

The variation of surface energy is

$$\delta\psi_s^{int}(\widehat{\boldsymbol{\varphi}},\delta\widehat{\boldsymbol{\varphi}})=\sum_i\frac{\delta}{\delta\widehat{\boldsymbol{\varphi}}}\int_{\mathcal{S}_i}\widehat{\psi}\left(\widehat{\boldsymbol{F}}\right)\mathrm{d}A \tag{2.19}$$

where $\widehat{\boldsymbol{F}}$ is the reduced rank form of the original gradient $\boldsymbol{F}$, with the notation $\widehat{\text{Grad}}\{\circ\} = \text{Grad}\{\circ\} \cdot \widehat{\boldsymbol{I}} = \text{Grad}\{\circ\} \cdot (\boldsymbol{I} - \boldsymbol{N} \otimes \boldsymbol{N})$. This quantity represents deformation gradient $\boldsymbol{F}$, while ignoring the components normal to the surface. $\widehat{\boldsymbol{F}}$ complies with the deformation gradient $\boldsymbol{F}$ along the surface, but satisfies the property $\widehat{\boldsymbol{F}} \cdot \boldsymbol{N} = 0$.

Then,

$$\begin{aligned}
\frac{\delta}{\delta \widehat{\boldsymbol{\varphi}}} \int_{\mathcal{S}_i} \widehat{\psi}\,(\widehat{\boldsymbol{F}})\,\mathrm{d}A &= \int_{\mathcal{S}_i} \frac{\partial \widehat{\psi}}{\partial \widehat{\boldsymbol{F}}} : \delta \widehat{\boldsymbol{F}}\,\mathrm{d}A \\
&= \int_{\mathcal{S}_i} \widehat{\boldsymbol{P}} : \delta \widehat{\boldsymbol{F}}\,\mathrm{d}A \\
&= -\int_{\mathcal{S}_i} \delta\,\widehat{\boldsymbol{\varphi}} \cdot \widehat{\text{Div}}\,\widehat{\boldsymbol{P}}\,\mathrm{d}A + \int_{\mathcal{S}_i} \widehat{\text{Div}}\{\delta\,\widehat{\boldsymbol{\varphi}} \cdot \widehat{\boldsymbol{P}}\}\,\mathrm{d}A \\
&= -\int_{\mathcal{S}_i} \delta\,\widehat{\boldsymbol{\varphi}} \cdot \widehat{\text{Div}}\,\widehat{\boldsymbol{P}}\,\mathrm{d}A + \underbrace{\int_{\mathcal{S}_i} \widehat{C}\,\delta\,\widehat{\boldsymbol{\varphi}} \cdot \widehat{\boldsymbol{P}} \cdot \boldsymbol{N}\,\mathrm{d}A}_{\text{curvature term}} + \int_{\partial \mathcal{S}_i} \delta\,\widetilde{\boldsymbol{\varphi}} \cdot \widehat{\boldsymbol{P}} \cdot \widehat{\boldsymbol{N}}\,\mathrm{d}L.
\end{aligned} \tag{2.20}$$

The curvature term needs attention. The term denoted as $\widehat{C}$ is the surface divergence of the surface normal $\boldsymbol{N}$ and is defined as $\widehat{C} = -\widehat{\text{Div}}\,\boldsymbol{N}$. This term in general exists because of the fact that (see [10])

$$\int_{\mathcal{S}_i} \widehat{\text{Div}}\{\circ\}\,\mathrm{d}A = \int_{\partial \mathcal{S}_i} \{\circ\} \cdot \widehat{\boldsymbol{N}}\,\mathrm{d}L - \int_{\mathcal{S}_i} \widehat{C}\,\{\circ\} \cdot \boldsymbol{N}\,\mathrm{d}A. \tag{2.21}$$

If one has the property that $\{\circ\} = \{\circ\} \cdot \widehat{\boldsymbol{I}}$, (in other words, if the vector's projection onto the tangent plane is equal to itself), then the curvature term vanishes. In the current case, however, this cannot be said. On the other hand, the equality $\widehat{\boldsymbol{P}} \cdot \boldsymbol{N} = \boldsymbol{0}$ holds, causing the curvature term to ultimately vanish, since

$$\int_{\mathcal{S}_0} \widehat{C}\,\delta\,\widehat{\boldsymbol{\varphi}} \cdot \widehat{\boldsymbol{P}} \cdot \boldsymbol{N}\,\mathrm{d}A = \int_{\mathcal{S}_0} \widehat{C}\,\delta\,\widehat{\boldsymbol{\varphi}} \cdot \boldsymbol{0}\,\mathrm{d}A = 0. \tag{2.22}$$

The end result is that the sum of the variations of surface energies become

$$\sum_i \left[\int_{\partial \mathcal{S}_i} \delta\,\widehat{\boldsymbol{\varphi}} \cdot \widehat{\boldsymbol{P}} \cdot \widehat{\boldsymbol{N}}\,\mathrm{d}L - \int_{\mathcal{S}_i} \delta\,\widehat{\boldsymbol{\varphi}} \cdot \widehat{\text{Div}}\,\widehat{\boldsymbol{P}}\,\mathrm{d}A \right]. \tag{2.23}$$

Now, assume that the number of smooth surfaces that together comprise the

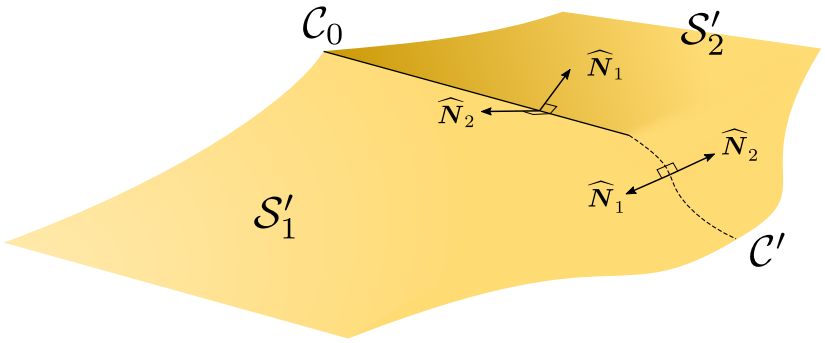

Figure 2.3: Decomposition of the surface. Note that $\widehat{\boldsymbol{N}}_1 = -\widehat{\boldsymbol{N}}_2$ on the curve $\mathcal{C}'$.

boundary $\partial\mathcal{B}_0$ is more than 1. Then it should be observed that every curve happens to be the intersection of two distinct surfaces, and the boundaries of the surfaces $\partial\mathcal{S}_i$ happen to be some union of these curves. This means that the first term in (2.23) can be replaced with a summation over the curves $\mathcal{C}_i$, though with a caveat: Since each curve belongs to the boundary of two surfaces, there will be a contribution from each neighbouring surface for a given curve. The result after this operation is that

$$\delta\psi_s^{int}(\widehat{\boldsymbol{\varphi}}, \delta\widehat{\boldsymbol{\varphi}}) = \sum_j \int_{\mathcal{C}_j} \delta\,\widehat{\boldsymbol{\varphi}} \cdot [\![\widehat{\boldsymbol{P}} \cdot \widehat{\boldsymbol{N}}]\!]\,\mathrm{d}L - \sum_i \int_{\mathcal{S}_i} \delta\,\widehat{\boldsymbol{\varphi}} \cdot \widehat{\mathrm{Div}}\,\widehat{\boldsymbol{P}}\,\mathrm{d}A \tag{2.24}$$

where $[\![\{\bullet\}]\!]$ denotes the sum of contributions from two neighbouring surfaces.

If the number of smooth surfaces is equal to one, the argument above may seem to not work, since there cannot be two terms in the integral. In that case, one can simply decompose the surface $\mathcal{S}_0$ into two surfaces $\mathcal{S}_1'$ and $\mathcal{S}_2'$ with the following property: $\mathcal{S}_1' \cap \mathcal{S}_2' = \mathcal{C}_0 \cup \mathcal{C}'$. Here, $\mathcal{C}_0$ is the already existing curve that happens to break the smoothness of the boundary whereas $\mathcal{C}'$ is a curve that does not break the smoothness between $\mathcal{S}_1'$ and $\mathcal{S}_2'$. This smoothness preserving property of $\mathcal{C}'$ implies that $\widehat{\boldsymbol{N}}_1 = -\widehat{\boldsymbol{N}}_2$ so that $\widehat{\boldsymbol{P}} \cdot [\widehat{\boldsymbol{N}}_1 + \widehat{\boldsymbol{N}}_2] = \boldsymbol{0}$, while the term for $\mathcal{C}_0$ is preserved. Eventually, this situation does not cause a loss of generality. The process is illustrated in Fig. 2.3.

2.3.3 Curve energy variation

The approach for curves on the boundary is similar to that of the surfaces',

$$\delta\psi_c^{int}(\widetilde{\boldsymbol{\varphi}}, \delta\widetilde{\boldsymbol{\varphi}}) = \sum_j \frac{\delta}{\delta\widetilde{\boldsymbol{\varphi}}} \int_{\mathcal{C}_j} \widetilde{\psi}\,(\widetilde{\boldsymbol{F}})\,\mathrm{d}L \tag{2.25}$$

where, $\widetilde{\boldsymbol{F}}$ is the reduced rank form of the original gradient $\boldsymbol{F}$, $\widetilde{\mathrm{Grad}}\{\circ\} = \mathrm{Grad}\{\circ\} \cdot \widetilde{\boldsymbol{I}} = \mathrm{Grad}\{\circ\} \cdot [\widetilde{\boldsymbol{N}} \otimes \widetilde{\boldsymbol{N}}]$. Here, $\widetilde{\boldsymbol{N}}$ denotes the tangent unit vector to the curve at any point. In this context, the following summation terms employ $\widetilde{\boldsymbol{m}}$ to denote the tangent *outward* unit vector on the curves' endpoints. So a clarification about this should be given outright. Also, $\dot{\boldsymbol{\varphi}}$ is used in this part to denote the restriction of $\boldsymbol{\varphi}$ to the boundaries of the curves.

Then we have that

$$\begin{aligned}
\frac{\delta}{\delta\widetilde{\boldsymbol{\varphi}}} \int_{\mathcal{C}_j} \widetilde{\psi}\,(\widetilde{\boldsymbol{F}})\,\mathrm{d}L &= \int_{\mathcal{C}_j} \frac{\partial\widetilde{\psi}}{\partial\widetilde{\boldsymbol{F}}} : \delta\widetilde{\boldsymbol{F}}\,\mathrm{d}L \\
&= \int_{\mathcal{C}_j} \widetilde{\boldsymbol{P}} : \delta\widetilde{\boldsymbol{F}}\,\mathrm{d}L \\
&= -\int_{\mathcal{C}_j} \delta\,\widetilde{\boldsymbol{\varphi}} \cdot \widetilde{\mathrm{Div}}\,\widetilde{\boldsymbol{P}}\,\mathrm{d}L + \int_{\mathcal{C}_j} \widetilde{\mathrm{Div}}\{\delta\,\widetilde{\boldsymbol{\varphi}} \cdot \widetilde{\boldsymbol{P}}\}\,\mathrm{d}L \\
&= -\int_{\mathcal{C}_j} \delta\,\widetilde{\boldsymbol{\varphi}} \cdot \widetilde{\mathrm{Div}}\,\widetilde{\boldsymbol{P}}\,\mathrm{d}L + \underbrace{\int_{\mathcal{C}_j} \widetilde{C}\,\delta\,\widetilde{\boldsymbol{\varphi}} \cdot \widetilde{\boldsymbol{P}} \cdot \widetilde{\boldsymbol{N}}\,\mathrm{d}L}_{\text{curvature term}} + \sum_{\partial\mathcal{C}_j} \delta\,\dot{\boldsymbol{\varphi}} \cdot \widetilde{\boldsymbol{P}} \cdot \widetilde{\boldsymbol{m}}.
\end{aligned} \tag{2.26}$$

The curvature term, similar to the surface energy integrals, again exists and is equal to zero since $\widetilde{\boldsymbol{P}} \cdot \widetilde{\boldsymbol{m}} = \boldsymbol{0}$. Then the result becomes

$$\delta\psi_c^{int}(\dot{\boldsymbol{\varphi}}, \delta\widetilde{\boldsymbol{\varphi}}) = \sum_j \sum_{\partial\mathcal{C}_j} \delta\,\widetilde{\boldsymbol{\varphi}} \cdot \widetilde{\boldsymbol{P}} \cdot \widetilde{\boldsymbol{m}} - \sum_j \int_{\mathcal{C}_j} \delta\,\widetilde{\boldsymbol{\varphi}} \cdot \widetilde{\mathrm{Div}}\,\widetilde{\boldsymbol{P}}\,\mathrm{d}L \tag{2.27}$$

Linear Momentum Balance Equations	
Bulk	$\mathrm{Div}\boldsymbol{P} + \boldsymbol{B}_0 = \boldsymbol{0}$
Surface	$\widehat{\mathrm{Div}}\,\widehat{\boldsymbol{P}} - \boldsymbol{P}\cdot\boldsymbol{N} + \widehat{\boldsymbol{B}}_0 = \boldsymbol{0}$
Curve	$\widetilde{\mathrm{Div}}\,\widetilde{\boldsymbol{P}} - [\![\widehat{\boldsymbol{P}}\cdot\widehat{\boldsymbol{N}}]\!] + \widetilde{\boldsymbol{B}}_0 = \boldsymbol{0}$
Point	$\widetilde{\boldsymbol{P}}\cdot\widetilde{\boldsymbol{m}} + \widetilde{\widetilde{\boldsymbol{B}}}_0 = \boldsymbol{0}$

Table 2.1: Balance equations for the regions in the domain

2.3.4 Resulting equation

The variations computed up to this point together read

$$\begin{aligned}\frac{\delta\psi^{tot}}{\delta\boldsymbol{\varphi}} = \frac{\delta\psi^{ext}}{\delta\boldsymbol{\varphi}} &- \int_{\mathcal{B}_0}\delta\boldsymbol{\varphi}\cdot\mathrm{Div}\boldsymbol{P}\,\mathrm{d}V\\ &+\sum_i\int_{\mathcal{S}_i}\delta\widehat{\boldsymbol{\varphi}}\cdot\left[\boldsymbol{P}\cdot\boldsymbol{N} - \widehat{\mathrm{Div}}\,\widehat{\boldsymbol{P}}\right]\mathrm{d}A\\ &+\sum_j\int_{\mathcal{C}_j}\delta\,\widetilde{\boldsymbol{\varphi}}\cdot\left[[\![\widehat{\boldsymbol{P}}\cdot\widehat{\boldsymbol{N}}]\!] - \widetilde{\mathrm{Div}}\,\widetilde{\boldsymbol{P}}\right]\mathrm{d}L\\ &+\sum_j\sum_{\partial\mathcal{C}_j}\delta\,\dot{\boldsymbol{\varphi}}\cdot\widetilde{\boldsymbol{P}}\cdot\widetilde{\boldsymbol{m}}\\ &= 0\end{aligned} \tag{2.28}$$

Since the equality has to be achieved in every admissible $\delta\boldsymbol{\varphi}$, each integral and summation have to be equal to zero. This means that the multiplying terms for $\delta\boldsymbol{\varphi}$, $\delta\widehat{\boldsymbol{\varphi}}$, $\delta\widetilde{\boldsymbol{\varphi}}$ and $\delta\dot{\boldsymbol{\varphi}}$ have to be equal to zero. Even though an explicit formula for external energy was not assumed up to this point, the constraint described implies that the form it assumes has to be such that it eventually appears as an additional vector in each of the relevant terms, denoted with various modifications of $\boldsymbol{B}_0$. Since these conditions are valid for each surface and curve individually, we can generalize the results under the categories of bulk, surface and curve. The general equations can be found in Table 2.1

2.4 Material model

In order to solve the equations in (2.1), one needs to have explicit formulae for $\boldsymbol{P}$, $\widetilde{\boldsymbol{P}}$ and $\widetilde{\boldsymbol{P}}$ which describe the material model. In this section, Neo-Hookean material model is described along with similar quantifiers that are used to describe deformations and stresses.

2.4.1 Strain and stress measures

Different strain and stress descriptors turn out to be equivalent in linear modeling, but this is not the case for non-linear models. This means that one can choose among many different strain and stress measures. Here, the scope is limited to the descriptors whose domain is the undeformed configuration. Hence we include the formulations of Piola stress $\boldsymbol{P}$ and Piola-Kirchhoff stress $\boldsymbol{S}$, along with their surface and curve counterparts. As for the strain measures, the deformation gradient $\boldsymbol{F}$ and right Cauchy-Green deformation tensor $\boldsymbol{C}$ are formulated.

The deformation gradient $\boldsymbol{F}$ has already been introduced. Right Cauchy-Green deformation tensor $\boldsymbol{C}$ is defined by

$$\boldsymbol{C} = \boldsymbol{F}^{\mathrm{t}} \cdot \boldsymbol{F} \tag{2.29}$$

where the definition is such that pure rotations are eliminated from the original deformation gradient $\boldsymbol{F}$, leaving only the stretches in the tensor. This can be also observed by the identity $\mathrm{d}\boldsymbol{x} \cdot \mathrm{d}\boldsymbol{x} = \mathrm{d}\boldsymbol{X} \cdot \boldsymbol{C} \cdot \boldsymbol{X}$. The surface and curve counterparts of right Cauchy-Green deformation tensor are also defined similarly:

$$\widehat{\boldsymbol{C}} = \widehat{\boldsymbol{F}}^{\mathrm{t}} \cdot \widehat{\boldsymbol{F}}, \qquad \widetilde{\boldsymbol{C}} = \widetilde{\boldsymbol{F}}^{\mathrm{t}} \cdot \widetilde{\boldsymbol{F}} \tag{2.30}$$

The Piola stress tensors were already introduced in the previous sections via

$$\boldsymbol{P} = \frac{\partial \psi}{\partial \boldsymbol{F}}, \qquad \widehat{\boldsymbol{P}} = \frac{\partial \widehat{\psi}}{\partial \widehat{\boldsymbol{F}}}, \qquad \widetilde{\boldsymbol{P}} = \frac{\partial \widetilde{\psi}}{\partial \widetilde{\boldsymbol{F}}}. \tag{2.31}$$

Piola-Kirchhoff stress tensor, on the other hand, is defined as twice the derivative of the energy measure with respect to right Cauchy-Green deformation tensor. This reads

$$\boldsymbol{S} := 2\frac{\partial \psi}{\partial \boldsymbol{C}}, \qquad \widehat{\boldsymbol{S}} := 2\frac{\partial \widehat{\psi}}{\partial \widehat{\boldsymbol{C}}}, \qquad \widetilde{\boldsymbol{S}} := 2\frac{\partial \widetilde{\psi}}{\partial \widetilde{\boldsymbol{C}}}. \tag{2.32}$$

Another important quantity for finite element computations is the fourth order elasticity tensors. Their definitions are

$$\begin{aligned} \mathbb{A} &:= \frac{\partial \boldsymbol{P}}{\partial \boldsymbol{F}}, \qquad \widehat{\mathbb{A}} := \frac{\partial \widehat{\boldsymbol{P}}}{\partial \widehat{\boldsymbol{F}}}, \qquad \widetilde{\mathbb{A}} := \frac{\partial \widetilde{\boldsymbol{P}}}{\partial \widetilde{\boldsymbol{F}}}, \\ \mathbb{C} &:= 2\frac{\partial \boldsymbol{S}}{\partial \boldsymbol{C}}, \qquad \widehat{\mathbb{C}} := 2\frac{\partial \widehat{\boldsymbol{S}}}{\partial \widehat{\boldsymbol{C}}}, \quad \widetilde{\mathbb{C}} := 2\frac{\partial \widetilde{\boldsymbol{S}}}{\partial \widetilde{\boldsymbol{C}}}. \end{aligned} \tag{2.33}$$

2.4.2 Neo-Hookean model

In the following sections, along with the finite element implementation, the response of the domain is modeled after hyperelastic materials. For the specific implementation, neo-Hookean type Helmholtz energy ψ was used. The exact form of this energy is given as

$$\psi(\boldsymbol{F}) = \frac{1}{2}\lambda \ln^2 J + \frac{1}{2}\mu \left[\boldsymbol{F} : \boldsymbol{F} - 3 - 2\ln J\right] \tag{2.34}$$

where $J > 0$ is assumed. ψ can also be written as a function of the right Cauchy-Green deformation tensor, in which case the form of it becomes

$$\psi(\boldsymbol{C}) = \frac{1}{2}\lambda \ln^2 J + \frac{1}{2}\mu \left[\mathrm{Tr}\,\boldsymbol{C} - 3 - 2\ln J\right]. \tag{2.35}$$

Here, $J = \mathrm{Det}\boldsymbol{F} = \sqrt{\mathrm{Det}\boldsymbol{C}}$ and $\mathrm{Tr}\{\bullet\}$ denotes the trace of the tensor. In equations (2.34) and (2.35), λ and μ happen to be the material parameters that

are called the Lamé constants. Similarly, we define the surface energies:

$$\begin{aligned}\widehat{\psi}(\widehat{\boldsymbol{F}}) &= \widehat{\gamma}\widehat{J} + \frac{1}{2}\widehat{\lambda}\ln^2\widehat{J} + \frac{1}{2}\widehat{\mu}\,[\widehat{\boldsymbol{F}} : \widehat{\boldsymbol{F}} - 2 - 2\ln\widehat{J}\,] \\ \widehat{\psi}(\widehat{\boldsymbol{C}}) &= \widehat{\gamma}\widehat{J} + \frac{1}{2}\widehat{\lambda}\ln^2\widehat{J} + \frac{1}{2}\widehat{\mu}\,[\widehat{\mathrm{Tr}}\,\widehat{\boldsymbol{C}} - 2 - 2\ln\widehat{J}\,].\end{aligned} \tag{2.36}$$

In equation (2.36), two Lamé constants for the surface are accompanied by a surface tension parameter $\widehat{\gamma}$, which is a term that is included to describe the area minimization effort of the material. When $\widehat{\gamma}$ is non-zero, the surface is not stress-free even in the undeformed configuration, which explains the lack of a similar term in the bulk. For visual examples one may refer to the appendices. The subtraction of 2 instead of 3 from $\widehat{\boldsymbol{F}} : \widehat{\boldsymbol{F}}$ is because of the fact that trace of the surface identity $\widehat{\boldsymbol{I}}$ operator is 2, instead of 3 which is the case for bulk. One could write an analogous expression for the curves but the fact that curves are one dimensional means that only one material constant for describing the extension suffices. In this case, after eliminating $\widetilde{\lambda}$, the curve energy becomes

$$\begin{aligned}\widetilde{\psi}(\widetilde{\boldsymbol{F}}) &= \widetilde{\gamma}\widetilde{J} + \frac{1}{2}\widetilde{\mu}\,[\widetilde{\boldsymbol{F}} : \widetilde{\boldsymbol{F}} - 1 - 2\ln\widetilde{J}\,] \\ \widetilde{\psi}(\widetilde{\boldsymbol{C}}) &= \widetilde{\gamma}\widetilde{J} + \frac{1}{2}\widetilde{\mu}\,[\widetilde{\mathrm{Tr}}\,\widetilde{\boldsymbol{C}} - 1 - 2\ln\widetilde{J}\,].\end{aligned} \tag{2.37}$$

2.4.2.1 Bulk model

Here, we present the form that stress tensors assume for the bulk.

$$\begin{aligned}\boldsymbol{P}(\boldsymbol{F}) &= \frac{\partial\psi(\boldsymbol{F})}{\partial\boldsymbol{F}} = \mu[\boldsymbol{F} - \boldsymbol{f}^{\mathrm{t}}], \\ \boldsymbol{S}(\boldsymbol{F}) &= 2\frac{\partial\psi(\boldsymbol{C})}{\partial\boldsymbol{C}} = \mu[\boldsymbol{I} - \boldsymbol{C}^{-1}].\end{aligned} \tag{2.38}$$

It is important to have an expression for the linearized version of Piola stress $\boldsymbol{P}$ for small deformation problems. In this case, first order Taylor expansion gives

the result:

$$\begin{aligned} \operatorname{Lin} \boldsymbol{P} &= \boldsymbol{P}|_{\boldsymbol{F}=\boldsymbol{I}} + \mathbb{A}|_{\boldsymbol{F}=\boldsymbol{I}} : [\boldsymbol{F}-\boldsymbol{I}] \quad &= 3\lambda\boldsymbol{\epsilon}^{\mathrm{vol}} + 2\mu\boldsymbol{\epsilon}, \\ \operatorname{Lin} \boldsymbol{C} &= \boldsymbol{S}|_{\boldsymbol{C}=\boldsymbol{I}} + \frac{1}{2}\mathbb{C}|_{\boldsymbol{C}=\boldsymbol{I}} : [\boldsymbol{C}-\boldsymbol{I}] \quad &= 3\lambda\boldsymbol{\epsilon}^{\mathrm{vol}} + 2\mu\boldsymbol{\epsilon}. \end{aligned} \tag{2.39}$$

Here, $\boldsymbol{\epsilon}$ is the infinitesimal strain tensor that is defined by $\boldsymbol{\epsilon} = \frac{1}{2}[\boldsymbol{I} \overline{\otimes} \boldsymbol{I} + \boldsymbol{I} \underline{\otimes} \boldsymbol{I}] : [\boldsymbol{F}-\boldsymbol{I}]$. Then $\boldsymbol{\epsilon}^{\mathrm{vol}} = \frac{1}{3}[\boldsymbol{I} \otimes \boldsymbol{I}] : \boldsymbol{\epsilon}$. In equation (2.39), $\mathbb{A}$ is the fourth order elasticity tensor and it is defined as

$$\begin{aligned} \mathbb{A} &= \frac{\partial \boldsymbol{P}}{\partial \boldsymbol{F}} = \lambda[\boldsymbol{f}^{\mathrm{t}} \otimes \boldsymbol{f}^{\mathrm{t}} + \ln J\, \mathbb{D}] + \mu[\mathbb{I} - \mathbb{D}], \qquad \text{with} \\ \mathbb{D} &= \frac{\partial \boldsymbol{f}^{\mathrm{t}}}{\partial \boldsymbol{F}} = -\boldsymbol{f}^{\mathrm{t}} \underline{\otimes} \boldsymbol{f}, \qquad \mathbb{I} = \frac{\partial \boldsymbol{F}}{\partial \boldsymbol{F}} = \boldsymbol{i} \overline{\otimes} \boldsymbol{I}. \end{aligned} \tag{2.40}$$

Similarly, $\mathbb{C}$ is defined as

$$\begin{aligned} \mathbb{C} &= 2\frac{\partial \boldsymbol{S}}{\partial \boldsymbol{C}} = \lambda[\tfrac{1}{2}\boldsymbol{C}^{-1} \otimes \boldsymbol{C}^{-1} + \ln J\, \mathbb{H}] - \mu\mathbb{H} \qquad \text{with} \\ \mathbb{H} &= \frac{\partial \boldsymbol{C}^{-1}}{\partial \boldsymbol{C}} = -\tfrac{1}{2}[\boldsymbol{C}^{-1} \overline{\otimes} \boldsymbol{C}^{-1} + \boldsymbol{C}^{-1} \underline{\otimes} \boldsymbol{C}^{-1}]. \end{aligned} \tag{2.41}$$

2.4.2.2 Surface model

$$\begin{aligned} \widehat{\boldsymbol{P}}(\widehat{\boldsymbol{F}}) &= \frac{\partial \psi(\widehat{\boldsymbol{F}})}{\partial \widehat{\boldsymbol{F}}} = \hat{\gamma}\hat{J}\,\hat{\boldsymbol{f}}^{\mathrm{t}} + \hat{\lambda}\ln\hat{J}\,\hat{\boldsymbol{f}}^{\mathrm{t}} + \hat{\mu}[\widehat{\boldsymbol{F}} - \hat{\boldsymbol{f}}^{\mathrm{t}}], \\ \widehat{\boldsymbol{S}}(\widehat{\boldsymbol{C}}) &= 2\frac{\partial \psi(\widehat{\boldsymbol{F}})}{\partial \widehat{\boldsymbol{F}}} = \hat{\gamma}\hat{J}\,\widehat{\boldsymbol{C}}^{-1} + \hat{\lambda}\ln\hat{J}\,\widehat{\boldsymbol{C}}^{-1} + \hat{\mu}[\hat{\boldsymbol{I}} - \widehat{\boldsymbol{C}}^{-1}]. \end{aligned} \tag{2.42}$$

The expressions for linearized surface stresses are derived similar to the case

of bulk's. It reads

$$\begin{aligned}\operatorname{Lin}\widehat{\boldsymbol{P}} &= \widehat{\boldsymbol{P}}|_{\widehat{\boldsymbol{F}}=\widehat{\boldsymbol{I}}} + \widehat{\mathbb{A}}|_{\widehat{\boldsymbol{F}}=\widehat{\boldsymbol{I}}} : [\widehat{\boldsymbol{F}} - \widehat{\boldsymbol{I}}] \\ &= \widehat{\gamma}\,\widehat{\boldsymbol{I}} + 2[\widehat{\lambda} + \widehat{\gamma}]\widehat{\boldsymbol{\epsilon}}^{\mathrm{vol}} + 2[\widehat{\mu} - \widehat{\gamma}]\widehat{\boldsymbol{\epsilon}} + \widehat{\gamma}\,[\widehat{\boldsymbol{F}} - \widehat{\boldsymbol{I}}], \\ \operatorname{Lin}\widehat{\boldsymbol{S}} &= \widehat{\boldsymbol{S}}|_{\widehat{\boldsymbol{C}}=\widehat{\boldsymbol{I}}} + \frac{1}{2}\widehat{\mathbb{C}}|_{\widehat{\boldsymbol{C}}=\widehat{\boldsymbol{I}}} : [\widehat{\boldsymbol{C}} - \widehat{\boldsymbol{I}}] \\ &= \widehat{\gamma}\,\widehat{\boldsymbol{I}} + 2[\widehat{\lambda} + \widehat{\gamma}]\widehat{\boldsymbol{\epsilon}}^{\mathrm{vol}} + 2[\widehat{\mu} - \widehat{\gamma}]\widehat{\boldsymbol{\epsilon}}.\end{aligned} \tag{2.43}$$

Similar to the case for bulk, $\boldsymbol{\epsilon}$ is the infinitesimal strain tensor and is equal to $\widehat{\boldsymbol{\epsilon}} = \frac{1}{2}[\widehat{\boldsymbol{I}} \overline{\otimes} \widehat{\boldsymbol{I}} + \widehat{\boldsymbol{I}} \underline{\otimes} \widehat{\boldsymbol{I}}] : [\widehat{\boldsymbol{F}} - \widehat{\boldsymbol{I}}]$. On the contrary $\widehat{\boldsymbol{\epsilon}}^{\mathrm{vol}} = \frac{1}{2}[\widehat{\boldsymbol{I}} \otimes \widehat{\boldsymbol{I}}] : \widehat{\boldsymbol{\epsilon}}$ is the volumetric strain. Note that the factor is $\frac{1}{2}$ instead of $\frac{1}{3}$, which is the situation for the bulk. Even though it is called volumetric, the term actually refers to the relevant measure at the considered space, which is area for surfaces. $\widehat{\mathbb{A}}$ is the fourth order elasticity tensor and it is defined as

$$\begin{aligned}&\widehat{\mathbb{A}} = \frac{\partial \widehat{\boldsymbol{P}}}{\partial \widehat{\boldsymbol{F}}} = \widehat{\gamma}\widehat{J}[\widehat{\boldsymbol{f}}^{\mathrm{t}} \otimes \widehat{\boldsymbol{f}}^{\mathrm{t}} + \widehat{\mathbb{D}}] + \lambda[\widehat{\boldsymbol{f}}^{\mathrm{t}} \otimes \widehat{\boldsymbol{f}}^{\mathrm{t}} + \ln \widehat{J}\,\widehat{\mathbb{D}}] + \widehat{\mu}[\widehat{\mathbb{I}} - \widehat{\mathbb{D}}] \qquad \text{with} \\ &\widehat{\mathbb{D}} = \frac{\partial \widehat{\boldsymbol{f}}^{\mathrm{t}}}{\partial \widehat{\boldsymbol{F}}} = -\widehat{\boldsymbol{f}}^{\mathrm{t}} \underline{\otimes} \widehat{\boldsymbol{f}} + [\boldsymbol{i} - \widehat{\boldsymbol{i}}] \overline{\otimes} [\widehat{\boldsymbol{f}} \cdot \widehat{\boldsymbol{f}}^{\mathrm{t}}], \qquad \widehat{\mathbb{I}} = \frac{\partial \widehat{\boldsymbol{F}}}{\partial \widehat{\boldsymbol{F}}} = \boldsymbol{i} \overline{\otimes} \widehat{\boldsymbol{I}}.\end{aligned} \tag{2.44}$$

Similarly, $\widehat{\mathbb{C}}$ is

$$\begin{aligned}&\widehat{\mathbb{C}} = 2\frac{\partial \widehat{\boldsymbol{S}}}{\partial \widehat{\boldsymbol{C}}} = \widehat{\gamma}\widehat{J}[\tfrac{1}{2}\widehat{\boldsymbol{C}}^{-1} \otimes \widehat{\boldsymbol{C}}^{-1} + \widehat{\mathbb{H}}] + \widehat{\lambda}[\tfrac{1}{2}\widehat{\boldsymbol{C}}^{-1} \otimes \widehat{\boldsymbol{C}}^{-1} + \ln \widehat{J}\,\widehat{\mathbb{H}}] - \mu\widehat{\mathbb{H}} \qquad \text{with} \\ &\widehat{\mathbb{H}} = \frac{\partial \widehat{\boldsymbol{C}}^{-1}}{\partial \widehat{\boldsymbol{C}}} = -\frac{1}{2}[\widehat{\boldsymbol{C}}^{-1} \overline{\otimes} \widehat{\boldsymbol{C}}^{-1} + \widehat{\boldsymbol{C}}^{-1} \underline{\otimes} \widehat{\boldsymbol{C}}^{-1}].\end{aligned} \tag{2.45}$$

2.4.2.3 Curve model

$$\begin{aligned}\widetilde{\boldsymbol{P}}(\widetilde{\boldsymbol{F}}) &= \frac{\partial \psi(\widetilde{\boldsymbol{F}})}{\partial \widetilde{\boldsymbol{F}}} = \widetilde{\gamma}\widetilde{J}\,\widetilde{\boldsymbol{f}}^{\mathrm{t}} + \widetilde{\mu}[\widetilde{\boldsymbol{F}} - \widetilde{\boldsymbol{f}}^{\mathrm{t}}], \\ \widetilde{\boldsymbol{S}}(\widetilde{\boldsymbol{C}}) &= 2\frac{\partial \psi(\widetilde{\boldsymbol{F}})}{\partial \widetilde{\boldsymbol{F}}} = \widetilde{\gamma}\widetilde{J}\,\widetilde{\boldsymbol{C}}^{-1} + \widetilde{\mu}[\widetilde{\boldsymbol{I}} - \widetilde{\boldsymbol{C}}^{-1}].\end{aligned} \tag{2.46}$$

It is important to have an expression for the linearized version of Piola stress $\boldsymbol{P}$ for small deformation problems. In this case, first order Taylor expansion gives the result:

$$\begin{aligned}\operatorname{Lin}\widetilde{\boldsymbol{P}} &= \widetilde{\boldsymbol{P}}|_{\widetilde{\boldsymbol{F}}=\widetilde{\boldsymbol{I}}} + \widetilde{\mathbb{A}}|_{\widetilde{\boldsymbol{F}}=\widetilde{\boldsymbol{I}}} : [\widetilde{\boldsymbol{F}} - \widetilde{\boldsymbol{I}}] \\ &= \widetilde{\gamma}\,[\widetilde{\boldsymbol{I}} + \widetilde{\boldsymbol{\epsilon}}^{\mathrm{vol}}] + 2[\widetilde{\mu} - \widetilde{\gamma}]\widetilde{\boldsymbol{\epsilon}} + \widetilde{\gamma}\,[\widetilde{\boldsymbol{F}} - \widetilde{\boldsymbol{I}}], \\ \operatorname{Lin}\widetilde{\boldsymbol{S}} &= \widetilde{\boldsymbol{S}}|_{\widetilde{\boldsymbol{C}}=\widetilde{\boldsymbol{I}}} + \frac{1}{2}\widetilde{\mathbb{C}}|_{\widetilde{\boldsymbol{C}}=\widetilde{\boldsymbol{I}}} : [\widetilde{\boldsymbol{C}} - \widetilde{\boldsymbol{I}}] \\ &= \widetilde{\gamma}\,[\widetilde{\boldsymbol{I}} + \widetilde{\boldsymbol{\epsilon}}^{\mathrm{vol}}] + 2[\widetilde{\mu} - \widetilde{\gamma}]\widetilde{\boldsymbol{\epsilon}}.\end{aligned} \tag{2.47}$$

In equation (2.47), $\widetilde{\mathbb{A}}$ is the fourth order elasticity tensor and it is defined as

$$\begin{aligned}&\widetilde{\mathbb{A}} = \frac{\partial\widetilde{\boldsymbol{P}}}{\partial\widetilde{\boldsymbol{F}}} = \widetilde{\gamma}\widetilde{J}[\widetilde{\boldsymbol{f}}^{\mathrm{t}} \otimes \widetilde{\boldsymbol{f}}^{\mathrm{t}} + \widetilde{\mathbb{D}}] + \widetilde{\mu}[\widetilde{\mathbb{I}} - \widetilde{\mathbb{D}}] \qquad \text{with} \\ &\widetilde{\mathbb{D}} = \frac{\partial\widetilde{\boldsymbol{f}}^{\mathrm{t}}}{\partial\widetilde{\boldsymbol{F}}} = -\widetilde{\boldsymbol{f}}^{\mathrm{t}} \underline{\otimes}\, \widetilde{\boldsymbol{f}} + [\boldsymbol{i} - \widetilde{\boldsymbol{i}}] \overline{\otimes} [\widetilde{\boldsymbol{f}} \cdot \widetilde{\boldsymbol{f}}^{\mathrm{t}}], \qquad \widetilde{\mathbb{I}} = \frac{\partial\widetilde{\boldsymbol{F}}}{\partial\widetilde{\boldsymbol{F}}} = \boldsymbol{i} \overline{\otimes} \widetilde{\boldsymbol{I}}.\end{aligned} \tag{2.48}$$

Similarly, $\widetilde{\mathbb{C}}$ is defined as

$$\begin{aligned}&\widetilde{\mathbb{C}} = 2\frac{\partial\widetilde{\boldsymbol{S}}}{\partial\widetilde{\boldsymbol{C}}} = \widetilde{\gamma}\widetilde{J}[\tfrac{1}{2}\widetilde{\boldsymbol{C}}^{-1} \otimes \widetilde{\boldsymbol{C}}^{-1} + \widetilde{\mathbb{H}}] - \mu\widetilde{\mathbb{H}} \qquad \text{with} \\ &\widetilde{\mathbb{H}} = \frac{\partial\widetilde{\boldsymbol{C}}^{-1}}{\partial\widetilde{\boldsymbol{C}}} = -\frac{1}{2}[\widetilde{\boldsymbol{C}}^{-1} \overline{\otimes} \widetilde{\boldsymbol{C}}^{-1} + \widetilde{\boldsymbol{C}}^{-1} \underline{\otimes} \widetilde{\boldsymbol{C}}^{-1}].\end{aligned} \tag{2.49}$$

2.5 Finite element implementation

2.5.1 Discretization

The numerical implementation of the model is done via finite elements method. The domain is decomposed into subdomains, which are called elements, and to each element is attached a local set of functions that approximate the displacement field. These functions are called the shape functions. To ensure continuity of the material, continuity of the total function is necessary. In this case, the shape functions are chosen as Lagrange polynomials of order 1 and 2, which

are C^0 continuous globally. The shape of elements used are hexahedra. These polynomials are assigned to nodes that reside on each element, and the value of displacements on a point inside the element are computed by adding individual contributions of each shape function. The result reads

$$\boldsymbol{\varphi} = \sum_{i=1}^{N_e} N^i(\boldsymbol{\xi})\boldsymbol{\varphi}^i, \qquad \widehat{\boldsymbol{\varphi}} = \sum_{i=1}^{N_e} \widehat{N}^i(\widehat{\boldsymbol{\xi}})\widehat{\boldsymbol{\varphi}}^i, \qquad \widetilde{\boldsymbol{\varphi}} = \sum_{i=1}^{N_e} \widetilde{N}^i(\widetilde{\xi})\widetilde{\boldsymbol{\varphi}}^i. \tag{2.50}$$

Here, $\boldsymbol{\xi} = (\xi_1, \xi_2, \xi_3)$ denotes the coordinates in the reference unit element, while N_e is the number of nodes per element. Similarly, $\widehat{\boldsymbol{\xi}} = (\widehat{\xi}_1, \widehat{\xi}_2)$ denote the local coordinates in the shape function for surfaces and $\widetilde{\xi}$ denotes the coordinate in the local curve coordinates. With this definition the deformation gradients become

$$\begin{aligned} \boldsymbol{F} &= \mathrm{Grad}\boldsymbol{\varphi} \approx \sum_{i=1}^{N_e} \boldsymbol{\varphi}^i \otimes \mathrm{Grad}N^i \\ \widehat{\boldsymbol{F}} &= \widehat{\mathrm{Grad}}\widehat{\boldsymbol{\varphi}} \approx \sum_{i=1}^{N_e} \widehat{\boldsymbol{\varphi}}^i \otimes \widehat{\mathrm{Grad}}\widehat{N}^i \\ \widetilde{\boldsymbol{F}} &= \widetilde{\mathrm{Grad}}\widetilde{\boldsymbol{\varphi}} \approx \sum_{i=1}^{N_e} \widetilde{\boldsymbol{\varphi}}^i \otimes \widetilde{\mathrm{Grad}}\widehat{N}^i \end{aligned} \tag{2.51}$$

where

$$\mathrm{Grad}N^i = \frac{\partial N^i}{\partial \boldsymbol{\xi}}\frac{\partial \boldsymbol{\xi}}{\partial \boldsymbol{X}}, \qquad \widehat{\mathrm{Grad}}\widehat{N}^i = \frac{\partial \widehat{N}^i}{\partial \widehat{\boldsymbol{\xi}}}\frac{\partial \widehat{\boldsymbol{\xi}}}{\partial \widehat{\boldsymbol{X}}}, \qquad \widetilde{\mathrm{Grad}}\widetilde{N}^i = \frac{\partial \widetilde{N}^i}{\partial \widetilde{\boldsymbol{\xi}}}\frac{\partial \widetilde{\boldsymbol{\xi}}}{\partial \widetilde{\boldsymbol{X}}}. \tag{2.52}$$

Alhough it is possible to implement these quantities using local surface and curve coordinates, it requires a change of basis for every face and edge where the surface and curve energies are defined. This was not done in the actual finite element implementation. Rather, for all energetic faces and edges of an element, the actual value of $\boldsymbol{F}$ is computed on the relevant face or edge just like it is done for the bulk. Then, simply resorting to the equality in (2.9), the deformation gradients on the faces and edges are retrieved by multiplying $\boldsymbol{F}$ with the relevant projection operators. A similar procedure is repeated whenever $\boldsymbol{f}$ is required, too. The rationale behind this procedure is that the implementation of this method can be seamlessly made, since $\boldsymbol{F}$ is being computed for the bulk either way. This way, the same code that computes $\boldsymbol{F}$ on arbitrary points can be reused without

any extra work. The difficulty this method brings along is the need to compute $\widehat{\boldsymbol{I}}$, $\widetilde{\boldsymbol{I}}$, $\widehat{\boldsymbol{i}}$ and $\widetilde{\boldsymbol{i}}$. For this task, Nanson's formula is used extensively. It reads

$$\mathrm{d}a\,\boldsymbol{n} = J\,\mathrm{d}A\,\boldsymbol{F}^{-\mathrm{t}} \cdot \boldsymbol{N} \tag{2.53}$$

in which the scalar coefficients need not be calculated: one can simply normalize the vector after computing $\boldsymbol{F}^{-\mathrm{t}} \cdot \boldsymbol{N}$. Note that, in equation (2.53), $\boldsymbol{N}$ is substituted with the **known** unit normal vectors on the faces of the reference coordinates, i.e. $\boldsymbol{\xi}$, whereas the result $\boldsymbol{n}$ is the unit normal vectors in either deformed or undeformed configurations.

Keeping in mind the shape functions described previously and the intent to use them as an approximation for the actual displacement field, finite element method aims to approximate the total energy of the system described in (2.11) as a function of finitely many variables, namely $\boldsymbol{d}$, and then minimize it. Here, $\boldsymbol{d}$ is esentially a vector of global degrees of freedom of the system. So writing explicitly, a nonlinear function is being minimized

$$\psi^{tot}(\boldsymbol{\varphi}) \approx \psi(\boldsymbol{d}). \tag{2.54}$$

This minimization effort is then equivalent to finding the zeros of the derivative - called the global residual

$$\boldsymbol{R}(\boldsymbol{d}) := \frac{\partial \psi}{\partial \boldsymbol{d}}. \tag{2.55}$$

The nonlinear formulation of the material means that the residual is not linear in $\boldsymbol{d}$. Hence, finding the zeros of the residual requires an iterative approach. In the context of this thesis, Newton-Raphson scheme is applied to find the roots of the residual vector. This scheme linearizes the current state with

$$\boldsymbol{R}(\boldsymbol{d}) + \left.\frac{\partial \boldsymbol{R}}{\partial \boldsymbol{d}}\right|_{\boldsymbol{d}_n} \Delta\boldsymbol{d} = 0, \qquad \Delta\boldsymbol{d} = \boldsymbol{d}_{n+1} - \boldsymbol{d}_n \tag{2.56}$$

The term $\boldsymbol{K} = \partial \boldsymbol{R}/\partial \boldsymbol{d}$ is the stiffness matrix. To compute a specific entry $\boldsymbol{R}^I$, one has to add individual contributions from each element that the relevant node belongs to. Same is true for the stiffness matrix, too. In that case, it makes sense to traverse each element one by one, and **assemble** the residual vector and the

stiffness matrix as one goes along. This operation is denoted by the operator $\mathbf{A}$. Since each computation in an element is done with local node numbering, one has to find the corresponding global label of the relevant degrees of freedom of a node and add the contributions according to that global labels. The operator signifies this procedure. In this case we write

$$\boldsymbol{R}^I = \mathop{\mathbf{A}}_{e=1}^{N_{el}} \boldsymbol{R}_e^i, \qquad \boldsymbol{K}^{IJ} = \mathop{\mathbf{A}}_{e=1}^{N_{el}} \boldsymbol{K}_e^{ij}. \tag{2.57}$$

Here, $\boldsymbol{R}_e^i$ is the local residual vector and $\boldsymbol{K}_e^{ij}$ is the local stiffness matrix with the local node labels i and j.

The explicit form of the local residual vector is

$$\begin{aligned} \boldsymbol{R}_e^i = & \int_{\mathcal{B}_0^\beta} \boldsymbol{P} \cdot \mathrm{Grad} N^i \, \mathrm{d}V - \int_{\mathcal{B}_0^\beta} \boldsymbol{b}_0^p \, N^i \, \mathrm{d}V \\ & + \int_{\mathcal{S}_0^\beta} \widehat{\boldsymbol{P}} \cdot \widehat{\mathrm{Grad}} \widehat{N}^i \, \mathrm{d}A - \int_{\mathcal{S}_0^\beta} \widehat{\boldsymbol{b}}_0^p \, \widehat{N}^i \, \mathrm{d}A \\ & + \int_{\mathcal{C}_0^\beta} \widetilde{\boldsymbol{P}} \cdot \widetilde{\mathrm{Grad}} \widetilde{N}^i \, \mathrm{d}L - \int_{\mathcal{C}_0^\beta} \widetilde{\boldsymbol{b}}_0^p \, \widetilde{N}^i \, \mathrm{d}L \end{aligned} \tag{2.58}$$

and the form of local stiffness matrix is

$$\begin{aligned} \boldsymbol{K}_e^{ij} = & \int_{\mathcal{B}_0^\beta} \mathbb{A} \,\overline{:}\, \left[\mathrm{Grad} N^i \otimes \mathrm{Grad} N^j \right] \mathrm{d}V \\ & + \int_{\mathcal{S}_0^\beta} \widehat{\mathbb{A}} \,\overline{:}\, \left[\widehat{\mathrm{Grad}} \widehat{N}^i \otimes \widehat{\mathrm{Grad}} \widehat{N}^j \right] \mathrm{d}A \\ & + \int_{\mathcal{C}_0^\beta} \widetilde{\mathbb{A}} \,\overline{:}\, \left[\widetilde{\mathrm{Grad}} \widetilde{N}^i \otimes \widetilde{\mathrm{Grad}} \widetilde{N}^j \right] \mathrm{d}L \end{aligned} \tag{2.59}$$

where $[\mathbb{T} \,\overline{:}\, \boldsymbol{S}]_{ab} = \mathbb{T}_{acbd} S_{cd}$.

There is a critical observation about equations (2.58) and (2.59) that has to be discussed. The hexahedral Langrange polynomials are obtained as a product of one dimensional shape functions. This is formulated as

$$N^i(\xi_1, \xi_2, \xi_3) = N^p(\xi_1) N^r(\xi_2) N^s(\xi_3) \tag{2.60}$$

where $p, r, s \in \{0, \ldots, M\}$ are the indices that map the node to its one dimensional counterparts, and M is the polynomial order. There is a one to one correspondence between the node index i in the element and (p, r, s) index numbering. The importance of this property is that, the value of the shape function of a node, say i, is equal to zero at every plane and line that it does not reside on.

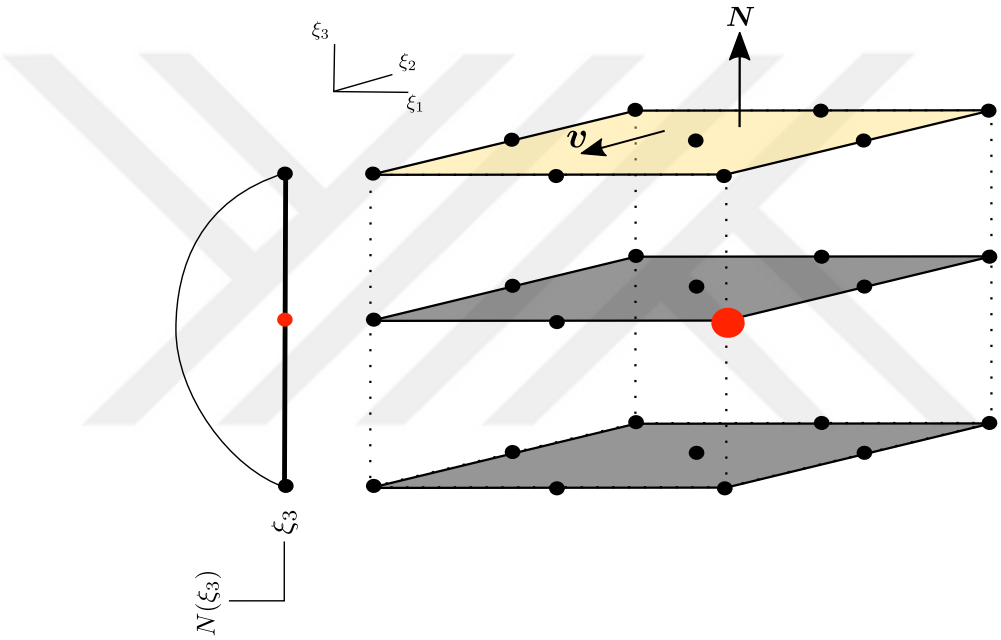

Figure 2.4: The tangential component of a shape function's gradient is zero when the node is outside the plane. 27 node Lagrange element is used as example

Consider the node labeled with red colour in Fig. 2.4 and the associated shape function's value at a point that is on the top face. For this node, value of $N^i(\boldsymbol{\xi})$ is equal to zero on the top face, because $N(\xi_3)$ is identically zero at every point on that plane. This means that the directional derivatives on the top plane, namely $\boldsymbol{v} \cdot \mathrm{Grad} N^i$ are equal to zero for every tangent vector $\boldsymbol{v}$ so that only the normal component is non zero. But then since $\mathrm{Grad} N \cdot \widehat{\boldsymbol{I}}$ computes the projection onto the plane, the result obtained after computing $\widehat{\mathrm{Grad}\widehat{N^i}}$ is identically zero whenever node i does not reside on the plane of interest. This means that we can assemble the residual vectors' and stiffness matrices' surface contributions without discriminating the nodes that do not reside on the surface. This again allows code reusability while bringing an insignificant inefficiency. The same

argument also holds for curves.

2.5.2 Implementation

The code used in this thesis is written in C++ from scratch. GiD is used as the meshing tool and the program begins by reading the mesh file, though it is adaptable to other mesh file types. Then it creates the element-face-edge topology. Currently it is able to do computations with linear 8 noded and quadratic 27 noded three dimensional Lagrange elements, but the restriction in this regard comes from the types of elements supported in GiD, rather than the code itself.

The integrals in equations (2.58) and (2.59) are computed using Legendre-Gauss quadrature method, which is a numerical approximation for integrals. User provides the number of quadrature points per dimension as an input and values up to 20 are supported.

Templates are heavily used for the functions that are called during the assembly phase. This allows the compiler to do some important optimizations such as loop unrolling and produce binaries that access elements of multi-dimensional arrays with constant, rather than needing to be provided the inner sizes of such arrays. These together allow generation of faster binaries, with the downside being requiring recompilation for each mesh file.

Since assembly is a procedure that is repeated for each element, it is a good candidate for parallelization. For this purpose, OpenMP, which is an application programming interface that is supported by major compiler vendors is used. Simple #pragma directives are included into the code to achieve parallelism. The global stiffness matrix and global residual vectors are the main shared variables that are being written, so an atomic lock is placed wherever required to prevent different threads from trying to access the same element simultaneously. This in general may happen when two elements that share common nodes are being assembled at the same time.

The main solver of preference is PARDISO [11, 12, 13]. PARDISO is a direct sparse system solver that fits the task perfectly, but it is not open source. As an alternative to PARDISO, MUMPS [14, 15], which is also a direct sparse solver, is implemented. MUMPS is an open source project contrary to PARDISO, which provides binaries and a license to acamedicians that lasts for only a short amount of time. The downside of MUMPS is that its speed depends on the graph partitioning libraries that are provided by the user during its build and the building phase is not so straightforward. Also, MUMPS' speed was found out to be typically 25-30% slower than that of PARDISO's in GNU/Linux environment and much slower in MAC OS X. Direct solvers' memory usage grow rapidly with problem size, so for large problems the iterative solvers of ViennaCL [16] are implemented. The advantage of ViennaCL is that with simple preprocessor directives the computation can be offloaded from CPU environment to GPU devices, which in this case is done with OpenCL environment. Another advantage is that ViennaCL is a header only library, though this results in longer compilation times.

Although the code was first written for GCC (GNU Compiler Collection), in its current form it also supports Intel Compiler through conditional compilation and is known to work with versions 17, 18 and 19. The advantage of Intel's compiler is that it produces very fast binaries by producing better vectorized codes and Intel's proprietary math library MKL includes a version of PARDISO that is observed to be faster than the regular one. The vectorization subject requires a comment: even though the current version of GCC 8 has improved vectorization support over its predecessors, it somehow still lacks this ability in nested loops compared to Intel Compiler, though the latter also has some room for improvement.

The performance of the code was analyzed with Intel Advisor profile program and it was observed that the most critical time consuming loop is the one where computation of the local stiffness matrix happens. The disassembly files of both compilers suggest that vectorization is poorly performed, if any. Hence, implementation of some intrinsic functions that map to hardware vector instructions such as AVX and FMA were found to improve assembly speed by up to 60% and

80%, respectively. Also, the symmetric structure of stiffness matrices were taken advantage of, whenever possible.

Chapter 3

Surface and Curve Effects on Beam Bending

3.1 Introduction

With the advent of nano manufacturing, some physical effects that are too weak to be observed in the macro scale have started to become prominent. There have been many publications on the effects of surface coating over bending stiffness of nanowires in the previous years, such as [3, 17]. A common observation made in these articles is that, for a silver or lead nanowire, the predicted -or equivalent- Young's modulus increases after some point when the wires' radius is decreased while keeping the length constant. This behavior in general is attributed to the existence of a fixed thickness surface coating that is formed around these nanowires. Naturally, the general tendency is to model this extra set of parameters on the surface of the structure, at which point the constant thickness of the boundary layer plays an important role.

In this chapter, surface effects on beams are studied, along with curves. We first begin by formulation of Euler and Timoshenko beam theories.

3.2 Euler and Timoshenko beam theories

In this part, we present the Euler and Timoshenko beam theory formulations. The main kinematic descriptors of these two formulations can be seen in figure 3.1. Although both theories assume that plane cross section of the beams remain as planes in the deformed configurations, Timoshenko beams include the assuptmion that these cross sections need not be orthogonal to the neutral axis. This necessitates inclusion of another kinematic variable, namely ϕ, that is required to describe this relaxed assumption, whereas for Euler beams just one dependent variable i.e. u, the vertical displacement of a point, suffices. For further reference, one can consult [18].

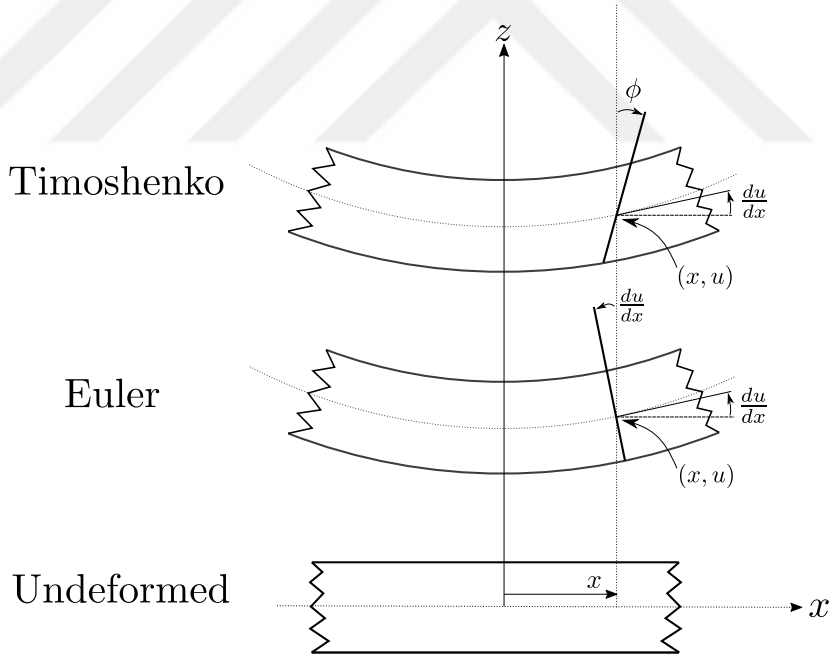

Figure 3.1: Kinematic variables in Euler and Timoshenko beams.

3.2.1 Euler beam theory

Since the cross section planes remain orthogonal to the neutral axis in Euler beams, there is no shear energy associated with the energy densities. Hence, the internal energy comprises only the bending energy. The total energy of the

system -including the energy associated with the external force field f- is

$$\mathcal{L} = \underbrace{\int_0^L fu \, \mathrm{d}x}_{\text{external energy}} + \underbrace{\int_0^L \frac{1}{2} EI \left[u''\right]^2 \mathrm{d}x}_{\text{internal energy}}. \tag{3.1}$$

Here, E, G, I, A are Young's modulus, shear modulus, moment of area and cross section of the beam, respectively.

Finding the minimizer of the total energy functional is equivalent to setting its variation equal to zero. The variation of the total energy $\mathcal{L}$ is

$$\begin{aligned} \delta\mathcal{L}\left(\delta u\right) &= \int_0^L f\delta u \, \mathrm{d}x + \int_0^L EIu''\delta u'' \, \mathrm{d}x + \\ &= \int_0^L f\delta u \, \mathrm{d}x - \int_0^L \frac{d}{dx}(EIu'')\delta u' \, \mathrm{d}x \\ &= \int_0^L \left[\frac{d^2}{dx^2}(EIu'') + f\right] \delta u \, \mathrm{d}x = 0 \end{aligned} \tag{3.2}$$

which yields the Euler beam equation

$$\frac{d^2}{dx^2}\left(EI\frac{d^2u}{dx^2}\right) + f = 0 \tag{3.3}$$

where the boundary conditions are imposed during the solution.

3.2.2 Timoshenko beam theory

Timoshenko beams have an additional shear term due to the relaxed assumptions about the cross sections. The total energy for a Timoshenko beam reads

$$\mathcal{L} = \int_0^L fu \, \mathrm{d}x + \underbrace{\int_0^L \frac{1}{2} EI \left[\phi'\right]^2 \mathrm{d}x}_{\text{bending energy}} + \underbrace{\int_0^L \frac{1}{2} CAG \left[\phi + u'\right]^2 \mathrm{d}x}_{\text{shear energy}}. \tag{3.4}$$

Then the variation is

$$\begin{aligned}
&\delta\mathcal{L}\left(\delta u, \delta\phi\right) = \\
&= \int_0^L f\,\delta u\,\mathrm{d}x + \int_0^L EI\phi'\,\delta\phi'\,\mathrm{d}x + \int_0^L CAG\left[\phi + u'\right]\delta u'\mathrm{d}x + \int_0^L CAG\left[\phi + u'\right]\delta\phi\,\mathrm{d}x \\
&= \int_0^L \left[f - \frac{d}{dx}\Big(CAG\left[\phi + u'\right]\Big)\right]\delta u\,\mathrm{d}x + \int_0^L \left[CAG\left[\phi + u'\right] - \frac{d}{dx}\left(EI\phi'\right)\right]\delta\phi\,\mathrm{d}x.
\end{aligned} \tag{3.5}$$

The resulting set of differential equations can be written down as

$$\begin{aligned}
\frac{d}{dx}\Big(CAG\left[\phi + u'\right]\Big) - f = 0 \\
CAG\left[\phi + u'\right] - \frac{d}{dx}\left(EI\phi'\right) = 0.
\end{aligned} \tag{3.6}$$

In equation (3.6), C is the shear correction factor. It is necessarily included because the shear stress profile on the cross section of the beam is assumed to be uniform although in reality it cannot be so because the shear stresses have to be zero at the top and bottom surfaces of the beam. Some values derived analytically can be found in [19].

The coefficients related to bending and shear in equations (3.3) and (3.6) can be replaced with their equivalent counterparts. This lets one use a clearer notation and simultaneously include surface and curve contributions into a single term. Henceforth, we will use the term K_κ for bending stiffness and K_γ for shear stiffness. Of course, in the sole presence of bulk parameters, we have that $K_\kappa = EI$ and $K_\gamma = CAG$.

Now, we present solutions of two specific boundary value problems for Euler beams and Timoshenko beams. First one of these problems concerns displacement of a double clamped beam under shear. Second one models the hinged beam subjected to pure moments. In both models, it is assumed that the cross section profile is uniform, so that they can be treated as constants. Also, it is assumed that no vertical force profile is present on the beams, i.e. $f = 0$.

3.2.3 Shear problem

Consider a double clamped beam with length L subjected to a displacement of d on the right end. The precise description of this problem for an Euler beam is formulated as such:

$$\begin{aligned} K_\kappa\, u^{(4)} &= 0 && \text{subject to} \\ u(0) = 0, \quad u(L) = d, \quad u'(0) &= 0, \quad u'(L) = 0. \end{aligned} \tag{3.7}$$

The solution to this problem fairly straightforward, so the derivation is ommitted. The solution reads

$$u(x) = -\frac{2d}{L^3}x^3 + \frac{3d}{L^2}x^2. \tag{3.8}$$

The shear force v can be found by using the identity $v(x) = M'(x)$, where M is the internal moment distribution of the beam. In this case, the shear force simply becomes

$$v = -\frac{12K_\kappa d}{L^3}. \tag{3.9}$$

The internal shear force is constant and is equal in magnitude to the reaction forces at both ends. This fact is used in later sections.

The formulation of the Timoshenko beam is similar:

$$\begin{aligned} K_\gamma[\phi + u'] - K_\kappa\phi'' = 0, \qquad K_\gamma[\phi' + u''] &= 0 \qquad \text{along with} \\ u(0) = 0, \qquad u(L) = d, \qquad \phi(0) = 0, \qquad \phi(L) &= 0. \end{aligned} \tag{3.10}$$

First two boundary conditions are common with Euler beams, whereas the last two simply mean that for a double clamped beam, the cross sections at both ends have to stay parallel to the wall that the beam is attached to. The equation can be reduced by observing that $\phi + u'$ has to be constant along the beam, since the second differential equation states that this term's derivative is identically zero. Skipping the intermediate steps, we end up with

$$\begin{aligned} u(x) &= -\frac{2Rd}{RL^3 + 12L}x^3 + \frac{3Rd}{RL^2 + 12}x^2 + \frac{12d}{RL^3 + 12L}x, \\ \phi(x) &= \frac{6Rd}{RL^3 + 12L}x^2 - \frac{6Rd}{RL^2 + 12} \end{aligned} \tag{3.11}$$

where, $R = K_\gamma / K_\kappa$ is the term describing the ratio between stiffnesses against shear to bending. It should be noted that RL^2 is a fundamental constant of this problem and also as RL^2 diverges to infinity, Timoshenko solution converges to that of Euler's, confirming the assumption on Euler beams having a much greater stiffness against shearing, which is then ommitted. For the Timoshenko beam, internal shear distribution is

$$v = K_\gamma[\phi + u'] = \frac{12K_\gamma d}{RL^3 + 12L}. \tag{3.12}$$

Again, in the limit case $RL^2 \to \infty$, internal shear of the Timoshenko beam is identical to that of Euler beam's, albeit with a sign difference that is due to the internal representation contrast between the formulations.

3.2.4 Pure moment problem

Next, the solution of pure moment problem is presented. Since the internal moment is constant in such a beam, the shear force is equal to zero in both models. This means that no terms related to shear appears in the Timoshenko beam, causing the solutions to be identical. Here, we present the relevant boundary conditions for both cases along with the solution. The derivations are fairly straightforward and not included because of this reason.

The relevant boundary conditions for Euler beams are

$$u(0) = 0, \quad u(L) \ = 0, \quad K_\kappa u''(0) = M_0, \quad K_\kappa u''(L) = M_0. \tag{3.13}$$

The first two boundary conditions in (3.13) are common with the Timoshenko beams. Because moments in Timoshenko beams are described as $M = -K_\kappa \phi'$ (negative sign is required since $\phi' > 0$ implies negative curvature), the latter two boundary conditions' equivalents for Timoshenko beams are

$$-K_\kappa \phi'(0) = M_0, \quad -K_\kappa \phi'(L) = M_0. \tag{3.14}$$

The solution to both problems then reads

$$u(x) = \frac{M_0}{2K_\kappa}x^2 - \frac{M_0 L}{2K_\kappa}x. \tag{3.15}$$

3.3 Numerical Examples

Experiments done with silver and lead nanowires suggest that these structures present a higher stiffness against bending in certain cases. This is reported as higher than normal Young's modulus measurements in the literature, see for instance [3, 17]. Although this work focuses on silver, the effects can be observed in other materials, one such example is the work in [20]. Stiffness in general increases when the thickness of a nanowire is decreased while keeping the total length fixed. The most frequent explanation of the phenomenon is based on the existence of surface effects which happen to become more prominent as the sizes decrease.

In [2], the surface effects are incorporated via an elastic model. The reason of surface effects becoming more prominent with shrinking cross section is attributed in many cases to the existence of a surface coating material that is formed either during the manufacturing process or due to oxidation. Since such layers have constant thicknesses, the equivalent surface material parameters are constant even when the diameter changes. This causes surface effects to have more influence on the overall behavior of the material as the diameter decreases. In [2, 21], surface parameters are incorporated into the models like a bulk material that is confined to a thickness t_s. We follow a similar pattern here and convert such oxidation layers' properties into fixed surface parameters by multiplying their respective bulk parameters by the coating thickness. Before proceeding further, the general formula for equivalent bending stiffness K_κ is presented.

Consider a small cross sectional element of a beam like the one shown in Fig. 3.2. In order to find K_κ, one has to add all the contributions from the bulk,

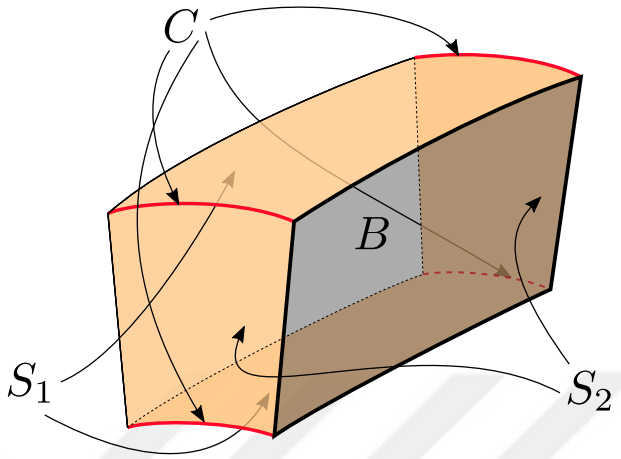

Figure 3.2: Rectangular cross section of a beam.

surfaces and curves. The general form of the bending stiffness becomes

$$\begin{gathered} K_\kappa = EI + \widehat{E}\widehat{I} + \widetilde{E}\widetilde{I}, \\ I = \int_{\mathcal{A}} y^2 \,\mathrm{d}A, \quad \widehat{I} = \oint_{\mathcal{L}} \widehat{y}^2 \,\mathrm{d}L, \quad \widetilde{I} = \sum_i \widetilde{y_i}^2. \end{gathered} \tag{3.16}$$

In equation (3.16), $\mathcal{A}$ is the cross sectional region while $\mathcal{L}$ comprises the lines that surround the cross sectional area and the summation index runs over all the points on the cross section that belong to an energetic curve. As usual, for a rectangular cross section with a width of b and height h,

$$\int_{\mathcal{A}} y^2 \,\mathrm{d}A = \int_0^b \int_{-h/2}^{h/2} y^2 \,\mathrm{d}y \,\mathrm{d}x = \frac{1}{12} b h^3 \tag{3.17}$$

is the second moment of area that is assigned to the bulk. One has to consider the surfaces in two groups, as demonstrated in figure 3.2. In that case we have

$$\oint_{\mathcal{L}} \widehat{y}^2 \,\mathrm{d}L = 2 \int_0^b \frac{h^2}{4} \mathrm{d}x + 2 \int_{-h/2}^{h/2} y^2 \,\mathrm{d}y = \frac{1}{2} b h^2 + \frac{1}{6} h^3 \tag{3.18}$$

and for the curves the result becomes

$$\sum_i \widetilde{y_i}^2 = \sum_{i=1}^4 \frac{h^2}{4} = h^2. \tag{3.19}$$

As a result, for a square cross sectional beam ($h = b$) the equivalent bending stiffness is

$$K_\kappa = \frac{1}{12}Eh^4 + \frac{2}{3}\widehat{E}h^3 + \widetilde{E}h^2. \tag{3.20}$$

Equation (3.20) has a similar form with different coefficients for other cross sections: the exponents on h remain the same for all cases. The form of the bending stiffness is useful in explaining the increasing Young's modulus for small diameters. Asymptotically, the ratio between bulk and surface contributions are determined by the exponents of h. It is clear that as $h \to \infty$, the equivalent stiffness is dominated by that of bulk's while as $h \to 0$, surface effect is the prominent factor. Of course, theoretically curve effects would dominate the behavior for small scales but there are yet no scientific findings that would necessitate their inclusion.

In order to demonstrate such effects, we set up a hypothetical beam problem where the scale of the entire beam is an adjustable parameter and the length to thickness and thickness to width ratios of the beam are preserved. For the following studies, the material parameters are fixed as: $\lambda = 4000$, $\mu = 1000$, $\widehat{\lambda} = 4$, $\widehat{\mu} = 1$, $\widetilde{\mu} = 0.1$. The linearized material model of the theory described in the previous chapter is implemented in the numerical simulations.

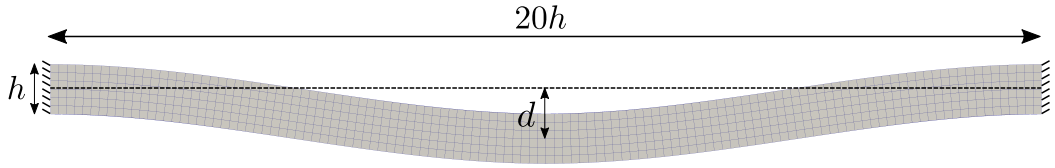

Figure 3.3: Illustration of the problem on the mesh used.

The beam of interest is chosen to be defined in terms of the parameter h, which is equal to its thickness. As can be seen in figure 3.3, the length of the beam is $20h$ whereas the width of the beam is taken to be equal to its thickness, h. The beam is subjected to a vertical displacement of d at its middle plane, and after the solution of each separate problem the vertical residuals of the nodes lying on the middle plane are added to compute the reaction force. The analytical Euler and Timoshenko solutions to this problem are identical to the ones found in 3.2.3. The only difference is that the problem described there represents half of

the problem considered here, due to mirror symmetry of the system with respect to the middle of the beam.

The finite element mesh consists of $6 \times 6 \times 120$ quadratic elements. A table that shows the computed equivalent stiffness values for different element types and numbers is also included in 3.1. Note that values in table 3.1 are results obtained from the solution of the pure bending problem, not the problem that is being considered right now. Results confirm that $6 \times 6 \times 120$ quadratic elements are adequate for obtaining accurate results thus in the following studies this mesh is utilized.

	Linear Elements			Quadratic Elements			Analytical
h	6 (4320)	8 (10240)	16 (81920)	6 (4320)	8 (10240)	12 (34560)	
Bulk							
10^{-1}	2.3821e-2	2.3609e-2	2.3404e-2	2.3336e-2	2.3335e-2	2.3335e-2	2.3333e-2
10^{-2}	2.3821e-6	2.3609e-6	2.3404e-6	2.3336e-6	2.3335e-6	2.3335e-6	2.3333e-6
10^{-3}	2.3821e-10	2.3609e-10	2.3404e-10	2.3336e-10	2.3335e-10	2.3335e-10	2.3333e-10
Bulk & Surface							
10^{-1}	2.6299e-2	2.6083e-2	2.5872e-2	2.5803e-2	2.5801e-2	2.5799e-2	2.5555e-2
10^{-2}	4.7474e-6	4.7156e-6	4.6820e-6	4.6727e-6	4.6710e-6	4.6696e-6	4.5555e-6
10^{-3}	2.5022e-9	2.4915e-9	2.4809e-9	2.4776e-9	2.4774e-9	2.4773e-9	2.4555e-9

Table 3.1: Bending stiffness K_κ values for different beam sizes characterized by h and various number of elements across the domain. Problem is described in 3.2.4. Total number of elements written in the paranthesis.

3.3.1 Solutions to shear problem

We now turn our attention to the shear problem. For a rectangular beam with dimensions of $h \times h \times 20h$ that is subjected to a vertical displacement of d at the middle, Euler beam theory states that bending stiffness can be computed using the formula

$$K_\kappa = -\frac{L^3 v}{12d}. \tag{3.21}$$

The error between the theoretical and simulation values for bulk only material can be considered in the acceptable range: when the beam has the dimensions of $1\text{m} \times 1\text{m} \times 20\text{m}$, the calculated bending stiffness is $230.1\,\text{Nm}^2$ compared to the

theoretical value of $233.3\,\mathrm{Nm}^2$. Consider the analytical expression for K_κ derived in (3.20). In order to compute the asymptotical behavior of the expression in terms of exponents, one may compute the logarithm of K_κ. In table 3.2, the limit behaviors of bending stiffness are summarized. The conclusion to be drawn is that while all materials are expected to have a slope of 4 for large h values, bulk and surface combination yields a slope of 3 as h goes to 0 and in this case it further decreases to 2 when curve is also included.

	Bulk	Bulk & Surface	Bulk, Surface & Curve
General Form	$\log(\frac{1}{12}Eh^4)$	$\log(\frac{1}{12}Eh^4+\frac{2}{3}\widehat{E}h^3)$	$\log(\frac{1}{12}Eh^4+\frac{2}{3}\widehat{E}h^3+\widetilde{E}h^2)$
$h\to\infty$	$4\log h+\log(\frac{1}{12}E)$	$4\log h+\log(\frac{1}{12}E)$	$4\log h+\log(\frac{1}{12}E)$
$h\to 0$	$4\log h+\log(\frac{1}{12}E)$	$3\log h+\log(\frac{2}{3}\widehat{E})$	$2\log h+\log\widetilde{E}$

Table 3.2: Asymptotical behavior of $\log K_\kappa$ vs. $\log h$.

Keeping table 3.2 in mind, we now turn our attention to the $\log-\log$ graph of the computed stiffness values, which is generated by utilizing Euler beam theory. Figure 3.4 shows that while the limiting behavior for bulk and surface meets the expectation, results obtained turn out to be wrong when curves are included. The reason for this is that, the existence of curves determine the bending stiffness for small sizes, but they show no effect whatsoever on the shear modulus of the beam. This causes the beam to have a greatly increased bending stiffness, while having shear stiffness values that simply cannot keep up with bending. Ultimately, Euler beam assumption about plane sections remaining orthogonal to the neutral axis fails, since the beam has greatly reduced shear resistance compared to bending. Note that, this happens although the ratios between the dimensions of the beam are preserved.

The explanation can be verified by looking at a resulting mesh. In figure 3.5 an exaggerated solution for the curve energy problem can be seen. It is clear that the resulting beam is under shear deformation, hence cannot be regarded as an Euler beam. It should be noted that the predicted K_κ values for bulk & surfaces also have high amount of disagreements with the analytical values. For instance, when $h = 10^{-7}\,\mathrm{m}$, the analytical bending stiffness is $K_\kappa = 2.22\times10^{-21}\,\mathrm{Nm}^2$ compared to the computed value of $K_\kappa = 1.96\times10^{-21}\,\mathrm{Nm}^2$. The reason for

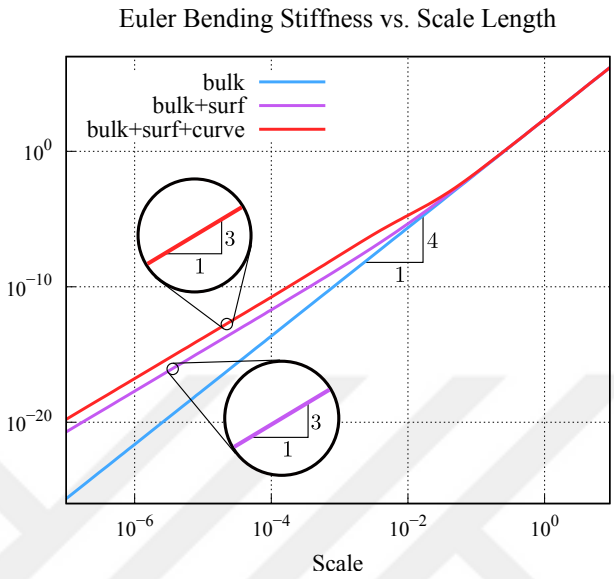

Figure 3.4: Size dependent stiffness of the Euler beam.

surfaces is more subtle than that of curves': although top and bottom surfaces comprise the majority of the bending stiffness (i.e. compared to the sides with the ratio being 3:1), they do not form any resistance against the beam's shear because these surfaces are subjected to out-of-plane motions.

There are two ways to overcome the problem of finding the bending stiffness: one might simply use a specific problem that eliminates the shear, or use the Timoshenko beam formulation to find the values. Applying pure moments on both ends eliminates internal shear, so that is the method we will use next. Before proceeding however, we shall provide the higher order beam formulation and derive an expression for bending stiffness in Timoshenko beams.

In Timoshenko beams, the term $R = K_\gamma/K_\kappa$ includes two unknowns and this means that there is no way to determine both stiffnesses at the same time with just one measurement. Hence, let us assume that we measure the displacement of one other point without influencing the setup. Assuming that the total length of the beam is $2L$, and the problem described in Sec. 3.2.3 is defined on the interval $[0, L]$, one needs to determine another point $x \in [0, L]$. This point cannot be $L/2$ because the problem has odd symmetry with respect to $x = L/2$, that is the displacement at $x = L/2$ is equal to $d/2$, independent of the material parameters.

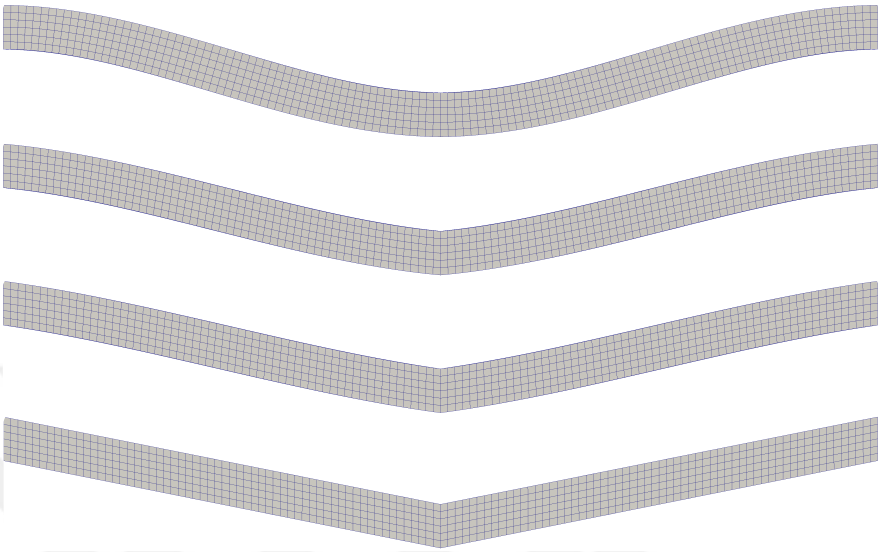

Figure 3.5: Progress from Euler beam to Timoshenko beam with decreasing h. The displacements are scaled for clarity.

So let us fix $x = L/4$ and denote the measured displacement at $x = L/4$, i.e. $u(L/4)$ with $\overline{u}$. In this case we have

$$u(L/4) = \overline{u} = -\frac{2Rd}{RL^3 + 12L}\frac{L^3}{64} + \frac{3Rd}{RL^2 + 12}\frac{L^2}{16} + \frac{12d}{RL^3 + 12L}\frac{L}{4} \tag{3.22}$$

in which it is possible to isolate RL^2 as

$$RL^2 = 12\left[\frac{d/4 + \overline{u}}{\overline{u} - 5/32\,d}\right], \qquad \text{and also} \qquad R^{-1} = \frac{L^2}{12}\left[\frac{\overline{u} - 5/32\,d}{d/4 - \overline{u}}\right]. \tag{3.23}$$

Now, substituting R in equation (3.12) lets one obtain the expression for K_γ,

$$K_\gamma = \frac{vL\,[RL^2 + 12]}{12d} = \frac{3vL}{32}\left[\frac{1}{\overline{u} - 5/32\,d}\right]. \tag{3.24}$$

Since $R = K_\gamma/K_\kappa$, one can retrieve K_κ via

$$K_\kappa = R^{-1}K_\gamma = \frac{L^2}{12}\left[\frac{\overline{u} - 5/32\,d}{d/4 - \overline{u}}\right]\frac{3vL}{32}\left[\frac{1}{\overline{u} - 5/32\,d}\right] = \frac{vL^3}{32\,[d - 4\overline{u}]}. \tag{3.25}$$

The computed stiffness values by the utilization of equation (3.25) are presented in Fig. 3.6. This time, the asymptotic behavior that curves are expected to display

can be observed clearly, with numerical values also matching the analytical results fairly close. Again considering the case of $h = 10^{-7}\,\mathrm{m}$, numerically computed bending stiffness is $2.046 \times 10^{-15}\,\mathrm{Nm}^2$ whereas the analytically derived value is equal to $2.000 \times 10^{-15}\,\mathrm{Nm}^2$.

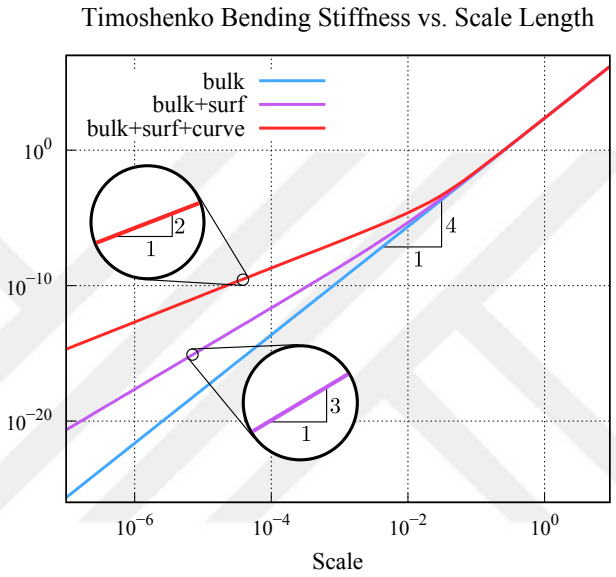

Figure 3.6: Size dependent stiffness of the Timoshenko beam.

	h			
	10^{-1}	10^{-3}	10^{-5}	10^{-7}
Computational				
Bulk	2.3737e-2	2.3737e-10	2.3737e-18	2.3737e-26
Bulk & Surface	2.6288e-2	2.5734e-9	2.3209e-15	2.3184e-21
Bulk, Surface & Curve	2.8298e-2	1.9298e-7	2.0425e-11	2.0466e-15
Analytical				
Bulk	2.3333e-2	2.3333e-10	2.3333e-18	2.3333e-26
Bulk & Surface	2.5555e-2	2.4555e-9	2.2245e-15	2.2222e-21
Bulk, Surface & Curve	2.7555e-2	2.0245e-7	2.0000e-11	2.0000e-15

Table 3.3: Bending stiffness calculations for the shear problem using Timoshenko beam.

As stated before, the value $RL^2/12$ esentially quantizes how well Euler's model predicts the reality: as the value approaches 1, shear effects set in and the beam can no longer be viewed through it. Thus, visualizing the evolution of $RL^2/12$ gives valuable insight about the problem. In figure 3.7, a comparison of numerical

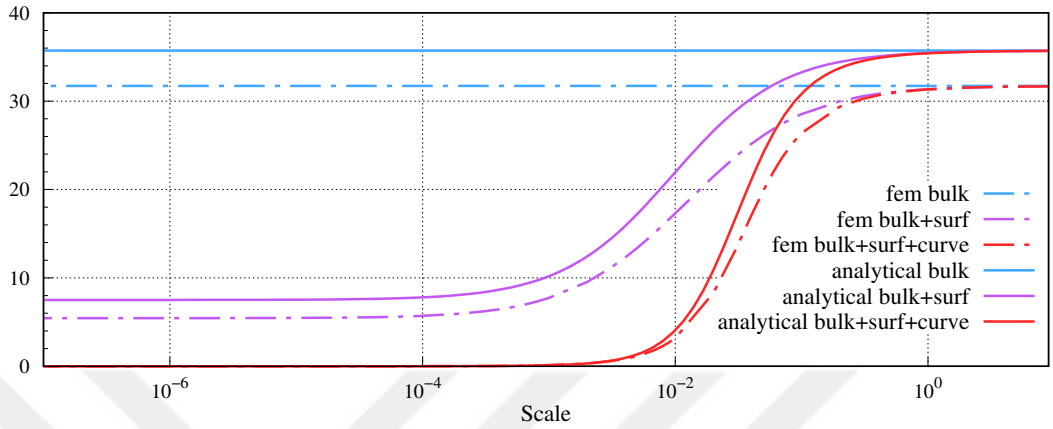

Figure 3.7: $\frac{L^2 K_\gamma}{12 K_\kappa}$ vs. thickness h for different material combinations.

and analytical values can be found. In order to compute the analytical value, one has to find K_γ through

$$K_\gamma = CAG + \widehat{C}\widehat{A}\widehat{G} = C' \left[AG + \widehat{A}\widehat{G} \right] \tag{3.26}$$

where the term $\widehat{A}$ is used to denote the total length of projection of the boundary on the vertical axis. One has to compute the projection instead of the total length because the orthogonal components have no shear resistance. The notation $\widehat{A}$ is kept for the sake of consistency, and it should not be confused with area. C' is the equivalent correction factor that in a sense averages the contributing correction factors. For square cross sections

$$K_\gamma = C' \left[Gh^2 + 2\widehat{G}h \right] \tag{3.27}$$

holds.

With the formulation above kept in mind, the comparison of numerical and analytical $RL^2/12$ values can be found in figure 3.7. Note that for the analytical model, correction factors are not included and the disparity between the lines stem from this. One may even retrieve correction factors from the graph.

It is clear that $RL^2/12$ converges to 0 when curve effects are present, and the problem becomes shear dominant. This causes Euler's model to completely

mispredict the behavior of the beam, whereas for surfaces $RL^2/12$ converges to a value greater than 1, but still on the same order of magnitude, causing an observable amount of disparity between stiffness values.

3.3.2 Solutions to pure moment problem

The solutions to pure moment bending is much easier to analyze due to lack of internal shear. All that one has to do is measure the displacement of the beam at the middle, i.e. $d = u(L/2)$. Here, L represents the whole length of the beam, instead of half of it like in the previous section. In this case for both Euler and Timoshenko beams one may recover the bending stiffness by utilizing the equality

$$u(L/2) = d = \frac{M_0}{2K_\kappa}\frac{L^2}{4} - \frac{M_0 L}{2K_\kappa}\frac{L}{2}, \qquad K_\kappa = -\frac{M_0 L^2}{8d}. \tag{3.28}$$

The moments at the endpoints are implemented with fource couples F_0, where $F_0 h = M_0$. The total force F_0 is distributed equally among the nodes which lie along the width of the beam. Figure (3.8) summarizes the setup.

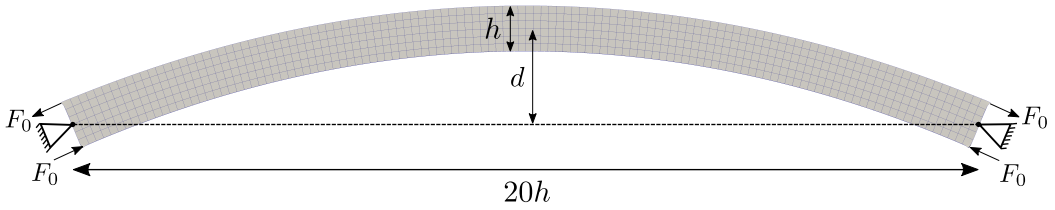

Figure 3.8: Pure moment problem illustration.

For this problem, the value of $\widetilde{\mu}$ is taken as $\widetilde{\mu} = 0.0001$, contrary to the previous examples. This is due to numerical stability problems associated with application of boundary conditions on a very few number of nodes. The comparison of analytical and numerical stiffness values can be found in 3.4.

The results indicate that pure moment application yields more accurate results while avoiding the extra formulation burden that is required for shearing beams.

We now proceed to comparison of experimental results in the literature with

	h			
	1	10^{-2}	10^{-4}	10^{-6}
Computational				
Bulk	233.360	2.3336e-6	2.3336e-14	2.3336e-22
Bulk & Surface	235.861	4.6727e-6	2.2528e-12	2.2281e-18
Bulk, Surface & Curve	235.862	4.6927e-5	4.2634e-9	2.0725e-15
Analytical				
Bulk	233.333	2.3333e-6	2.3333e-14	2.3333e-22
Bulk & Surface	235.555	4.5555e-6	2.2455e-12	2.2224e-18
Bulk, Surface & Curve	235.755	4.5755e-5	4.2455e-9	2.0222e-13

Table 3.4: Bending stiffness calculations for the pure moment problem using Euler/Timoshenko beam.

numerical solutions.

3.3.3 Comparison with experimental results

In this section we model a real silver nanowire with realistic parameters and compare the effective Young's modulus predictions of the model (effective means finding the value E_e such that $E_e I = K_\kappa$) with published experimental data. The experimental results are gathered from the work in [17], but one can find fairly similar results in [3], too.

In [17], authors manufacture several silver nanowires with same length but various diameters. The length of the suspended part of the nanowire is reported as 1µm. The largest diameter tested is around 140nm while the smallest diameter is about 15nm. The beams are subjected to a vertical force at the middle by AFM (Atomic Force Microscope), a problem which was described in the section 3.2.3. For numerical simulations, we again adopt a rectangular mesh with $6 \times 6 \times 240$ elements. Although nanowires have circular cross sections, using a square cross section only marginally alters the value of $RL^2/12$, so that we end up with fairly close results to what we would otherwise obtain. The length of the beam is set to 1µm and the thickness of the beam is varied through 15nm to 150nm. The

studies presented in [2, 17] compute an effective Young's modulus E_e by dividing the computed stiffness of the beam to moment of area. In those studies, stiffness is computed according to Euler's beam model. Here, we compare those experimental data with the analytical values and also numerical values that result from the simulations. For numerical values, we include both Euler and Timoshenko beam models' predictions. To model the surface, typical values for silver-oxide are used. In [17], the oxide layer's thickness is reported to be around 4nm, so that is the value used here.

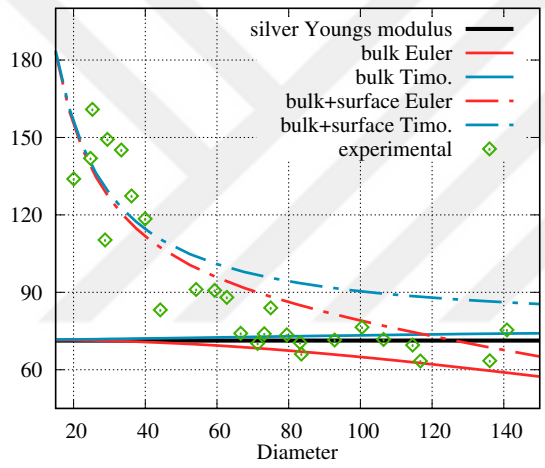

(a) Experimental and numerical effective Young's modulus measurements. Data from [17].

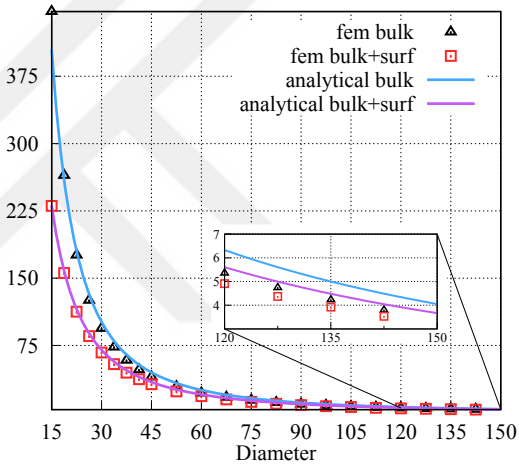

(b) Analytical and numerical $RL^2/12$ values. Shear correction factors not included in analytical values.

Figure 3.9: Experimental, analytical and numerical results compared. $E = 71.5\text{GPa}, \nu = 0.37$ for silver and $E = 51.5\text{GPa}, \nu = 0.25$ for silver oxide.

In figure 3.9a, one can track the effective Young's modulus values. The experimental results are obtained from Euler beam model, so they are in fact closest to our numerical values obtained through Euler's formula. We also include the numerical results for beams that have no surface components under the name bulk, which would correspond to a beam that lacks an oxidation layer. The reason they are included is that those values are expected to be fairly close to the Young's modulus of silver, and any variation signals some incompatibility with the underlying assumptions. One can see that experimentally obtained values drop below the Young's modulus of silver, which is normally an unexpected behavior. On the other hand, bulk only Euler beam's measurements (obtained from the finite

element model) also drop below that value. The reason for this is that the for large diameter values Euler beam model begins to fail. This can also be confirmed by the $RL^2/12$ graph seen in figure 3.9b. Both analytical and numerical results drop to around 3 for large diameters. This shows that one has to resort to Timoshenko beam theory for such large values. The underlying cause is purely geometrical unlike the case discussed in the previous chapters.

For small diameters, $RL^2/12$ is sufficiently large so that Timoshenko and Euler models agree. In that case, it is possible to observe the increase in effective Young's modulus and the experimental data match numerical values. This confirms that surface layers with constant thicknesses can indeed be modeled with the 2D surface theory described in the previous chapter.

Chapter 4

Bistable Beam Formulation

4.1 Introduction

The behavior that a buckled beam exhibits while transforming from one of the bistable states to the other is called snap-through. The reason is that a transverse force that forces beam to move between its two states is only required until a certain point after which the beam quickly snaps to its other stable state. This chapter is devoted to the formulation of an analytical model for beam buckling and is accompanied with numerical implementations. Comparisons with nonlinear finite element model are presented to justify the accuracy of the model. The surface effects are also incorporated in order to cover nano sized beams.

4.2 Kinematic variables

First, the kinematic model is introduced. The kinematic model is perhaps the single most important aspect of this study. The reason is that, a poorly chosen kinematic model has the potential to make the theory outright impractical for numerical simulations. For instance in [22], one of the kinematic descriptors is

chosen as the longitudinal displacement while the other variable is the tangent angle of the deformed beam. Although the latter is also used here, the former descriptor results in a more complicated formulation compared to what is obtained here. There are some other formulations that has been proposed in the literature, such as [23]. In [24], the equation is explicitly derived with taking the oddity of the buckling modes into account, again resulting in complicated equations. There are also some other works such as [25] that deal with the buckling behavior of other slender structures under distributed loads.

The formulation presented here is closest to the one derived in [26]. The main difference is that here we include one additional term which does not show up there. Also, the examples given in [26] belong to beams fixed with hinge supports, whereas we show results for double clamped beams, too.

The undeformed beam which is doubly clamped on its ends are assumed to be of length L. The reference configuration's coordinates are denoted by S. This beam is assumed to be deformed and that a function $\phi : [0, L] \to \mathbb{R}^2$ maps the points on the undeformed line onto the current configuration by $S \mapsto (\phi_1(S), \phi_2(S))$. Although one can work with coordinate functions, we switch to a more convenient representation of the deformation, namely: $\varphi : S \mapsto \boldsymbol{\varphi}(S) = (\Lambda(S)\,,\, \theta(S))$. Here, Λ denotes the stretch of the original map ϕ at the point S, i.e. $\Lambda = \sqrt{(\phi_1')^2 + (\phi_2')^2}$ whereas θ denotes the angle that the tangent line at the current configuration does with the abscissa, i.e. $\tan\theta = \phi_2'/\phi_1'$, provided that the right hand side exists.

Along with stretch, curvature is an essential quantifier in bending, so it has to be introduced in terms of the functions that we desire to use. Here, curvature is denoted by κ and satisfies the property that $|\kappa| = |d\boldsymbol{T}/dS|$ where $\boldsymbol{T}$ is the unit tangent vector and s is the arc length parametrization in the final configuration. In terms of Λ and θ, this equality becomes

$$\kappa = \frac{1}{\Lambda}\frac{d\theta}{dS}, \quad \text{where} \qquad \Lambda = \frac{ds}{dS} \tag{4.1}$$

Stretch and curvature are the main two quantities that are used here to describe

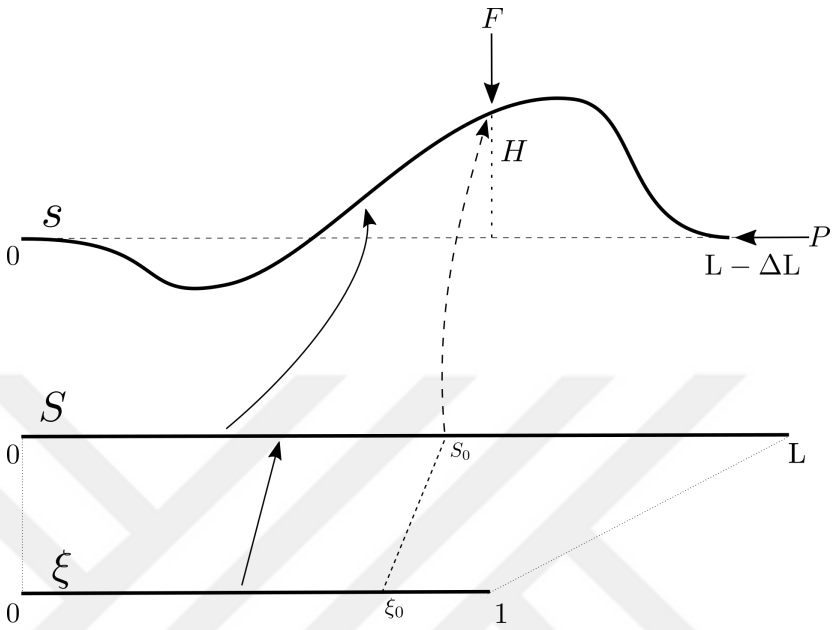

Figure 4.1: Composite mapping from the unit reference configuration to the current configuration. The map from unit ref. configuration to the reference configuration is linear.

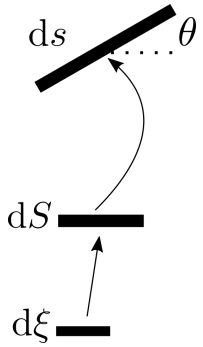

Figure 4.2: Small line element from the unit reference domain mapped to the current configuration.

the internal energy of the beam. In the next section, the energy function for the specific problem is constructed.

With this kinematic model, we can relate a point's (say, p) position in the undeformed configuration S_p to its position (x, y) in the deformed configuration via

$$\begin{aligned} x(S_p) &= \int_0^{S_p} \Lambda \cos\theta \, \mathrm{d}S, \\ y(S_p) &= \int_0^{S_p} \Lambda \sin\theta \, \mathrm{d}S. \end{aligned} \tag{4.2}$$

We also introduce a unit reference $\xi \in [0, 1]$ to normalize the arguments. This

is not necessary but it becomes useful when both doing a scale analysis of the problem and picking initial values for the numerical implementation, as explained in the later sections. No special letter is reserved for this map because it is simple in its explicit form: $\xi \mapsto L\xi = S$.

4.3 Energy functional

The problem that is of interest is the buckling behavior of a double clamped or double hinged beam under compression while a downward transverse force is applied at a specified position on the beam. These problems may be presented in two ways: One may either prescribe the relevant forces and try to find the solution to that problem or alternatively fix the displacements that are assumed to be the results of those unknown forces and then try to recover the values. As it is the case, prescribing forces is practically less useful but side-by-side comparison of the terms gives valuable information about recovering the forces after solving the latter problem. The relevant details are presented in Sec. 4.3.2.1. In each of the following sections, the following procedure is followed: First, the relevant quantities are expressed in terms of the reference coordinate S. Then, the equivalent form based on the unit reference coordinate ξ is presented. Lastly, the functional that is to be minimized is written after all the energy terms are introduced.

4.3.1 Internal energy

The material model is assumed to be linear elastic throughout the whole domain. The non-linearity of the theory originates from the geometry, as opposed to the material model itself. Hence, the contributions of stretch and bending may be separated and considered individually. The stretch Λ has to be sufficiently close to 1 in order to let one incorporate linear elasticity. The bending term warrants a remark: the curvature term is used without the stretch factor Λ^{-1}. This simplification is done because although large curvature values may ultimately appear,

the difference caused by the stretch will be negligible in comparison. Then the internal energy becomes

$$\begin{aligned}\mathcal{U} &= \int_0^L \frac{1}{2} K_\Lambda \left[\Lambda - 1\right]^2 \mathrm{d}S + \int_0^L \frac{1}{2} K_\theta \left[\frac{d\theta}{dX}\right]^2 \mathrm{d}S \\ &= \int_0^1 \frac{1}{2} K_\Lambda L \left[\Lambda - 1\right]^2 \mathrm{d}\xi + \int_0^1 \frac{1}{2} \frac{K_\theta}{L} \left[\frac{d\theta}{d\xi}\right]^2 \mathrm{d}\xi.\end{aligned} \tag{4.3}$$

The terms K_Λ and K_θ denote the stiffness of the beam exhibits against stretch and bending, respectively. They are general in that, the energy functionals are still valid for the cases which include surface effects. In such cases, all that has to be done is to substitute the equivalent values, which are the sum of bulk and surface effects. Explicitly,

$$\begin{aligned}K_\Lambda &= EA + \widehat{E}\widehat{A}, \\ K_\theta &= EI\ + \widehat{E}\widehat{I}.\end{aligned} \tag{4.4}$$

Here, K_θ is identical with K_κ which was introduced in chapter 3, and one may refer to (3.16) for its formulation. The name change is for the sake of consistency of subscripts being related to kinematic variables. The term $\widehat{A}$ denotes the perimeter of the cross section, as the surface stretch energies reside there. Again, the naming is chosen to preserve consistency across notations. Though, a warning is necessary: $\widehat{A}$ denotes the *total* curve length around the cross section in this study, whereas it was used to refer to the length of the curves that resist shearing in (3.26) in chapter 3, so that they are not necessarily equal.

4.3.2 External energy and geometric constraints

As explained in the Sec. 4.3, two different approaches to the same problems are presented. Namely: a force based and a displacement based formulation is presented in the sections 4.3.2.2 and 4.3.2.3. The force based approach is not useful in practice, though its usefulness will be apparent shortly.

4.3.2.1 Boundary conditions

For double clamped beams, the requirement is that the angle θ be zero at both ends:

$$\theta(0) = \theta(1) = 0 \tag{4.5}$$

Double hinged beams, on the other hand, do not support any moments on the boundaries so that

$$\theta'(0) = \theta'(1) = 0 \tag{4.6}$$

holds.

4.3.2.2 External energy

In the case that two external forces F (transverse) and P (compressive) are applied to the beam, corresponding potential energies can be written as

$$\begin{aligned} \mathcal{F} &= F \int_0^{s_0} \Lambda \sin\theta \, \mathrm{d}S = FL \int_0^{\xi_0} \Lambda \sin\theta \, \mathrm{d}\xi = FL \int_0^1 \mathbb{1}_{\xi_0} \Lambda \sin\theta \, \mathrm{d}\xi \\ \mathcal{P} &= P \int_0^{L} \Lambda \cos\theta \, \mathrm{d}S = PL \int_0^1 \Lambda \cos\theta \, \mathrm{d}\xi \end{aligned} \tag{4.7}$$

Here, $\mathbb{1}_{\xi_0}$ is the characteristic function of the interval $[0, \xi_0]$. Again, note that this part is not included in the formulation: the geometric constraints are used instead.

4.3.2.3 Geometric constraints

A short notice is required in this section. Since the quantities here are not free functionals to be minimized (or some combination thereof), the variations of these functionals have to be incorporated into the main equation along with their respective Lagrange multipliers. The symbols η_1, η_2 and η_3 are reserved as the three relevant Lagrange multipliers in this section and henceforth.

The main geometric constraint originates from the requirement that both ends of the beam be at the same height. This requirement reads

$$\mathcal{C}_1 = \frac{1}{L}\int_0^L \Lambda \sin\theta \,\mathrm{d}S = \int_0^1 \Lambda \sin\theta \,\mathrm{d}\xi = 0 \tag{4.8}$$

The second and third constraints are the displacement type counterparts of the terms derived in the previous section. If one assumes that the beam is compressed by an amount of ΔL and a specific point on the beam is forced to be at a height H then,

$$\mathcal{C}_2 = \frac{1}{L}\int_0^L \Lambda \cos\theta \,\mathrm{d}S = \int_0^1 \Lambda \cos\theta \,\mathrm{d}\xi = 1 - \frac{\Delta L}{L} \tag{4.9}$$

and

$$\mathcal{C}_3 = \frac{1}{L}\int_0^{s_0} \Lambda \sin\theta \,\mathrm{d}S = \int_0^1 \mathbb{1}_{\xi_0} \Lambda \sin\theta \,\mathrm{d}\xi = \frac{H}{L} \tag{4.10}$$

4.4 Resulting differential equation

To obtain the resulting differential equation, one has to compute the variation of the total energy along with the constraints, which are multiplied by their respective coefficients i.e. Lagrange multipliers. This requirement can be written as

$$\begin{aligned} &\delta\mathcal{L}\left(\delta\Lambda,\, \delta\theta\right) = \delta\left[\mathcal{U} + \eta_1 \mathcal{C}_1 + \eta_2 \mathcal{C}_2 + \eta_3 \mathcal{C}_3\right]\left(\delta\Lambda,\, \delta\theta\right) = 0 \qquad \text{along with} \\ &\qquad\qquad \mathcal{C}_1 = 0, \qquad \mathcal{C}_2 = 1 - \frac{\Delta L}{L}, \qquad \mathcal{C}_3 = \frac{H}{L}. \end{aligned} \tag{4.11}$$

The variations of each term are as follows:

$$\begin{aligned}\delta\mathcal{U}\left(\delta\Lambda,\,\delta\theta\right) &= \int_0^1 K_\Lambda L\left[\Lambda-1\right]\delta\Lambda\,\mathrm{d}\xi + \int_0^1 \frac{K_\theta}{L}\,\theta'\,\delta\theta'\,\mathrm{d}\xi \\ &= \int_0^1 K_\Lambda L\left[\Lambda-1\right]\delta\Lambda\,\mathrm{d}\xi - \int_0^1 \frac{K_\theta}{L}\,\theta''\,\delta\theta\,\mathrm{d}\xi\end{aligned} \tag{4.12}$$

where θ' and θ'' denote $d\theta/d\xi$ and $d^2\theta/d\xi^2$, respectively.

$$\begin{aligned}\eta_1\,\delta\mathcal{C}_1\left(\delta\Lambda,\,\delta\theta\right) &= \eta_1 \int_0^1 \left[\sin\theta\,\delta\Lambda + \Lambda\cos\theta\,\delta\theta\right]\,\mathrm{d}\xi \\ \eta_2\,\delta\mathcal{C}_2\left(\delta\Lambda,\,\delta\theta\right) &= \eta_2 \int_0^1 \left[\cos\theta\,\delta\Lambda - \Lambda\sin\theta\,\delta\theta\right]\,\mathrm{d}\xi \\ \eta_3\,\delta\mathcal{C}_3\left(\delta\Lambda,\,\delta\theta\right) &= \eta_3 \int_0^1 \mathbb{1}_{\xi_0}\left[\sin\theta\,\delta\Lambda + \Lambda\cos\theta\,\delta\theta\right]\,\mathrm{d}\xi\end{aligned} \tag{4.13}$$

Additionally, the variations of the terms found in (4.7) are presented. Note the similarity between the form of functionals found in (4.13) and in (4.14).

$$\begin{aligned}\delta\mathcal{F}\left(\delta\Lambda,\,\delta\theta\right) &= FL\int_0^1 \mathbb{1}_{\xi_0}\left[\sin\theta\,\delta\Lambda + \Lambda\cos\theta\,\delta\theta\right]\,\mathrm{d}\xi \\ \delta\mathcal{P}\left(\delta\Lambda,\,\delta\theta\right) &= PL\int_0^1 \left[\cos\theta\,\delta\Lambda - \Lambda\sin\theta\,\delta\theta\right]\,\mathrm{d}\xi\end{aligned} \tag{4.14}$$

One could have formulated the Lagrangian by replacing the constraints $\mathcal{C}_2$ and $\mathcal{C}_3$ with the potential functionals defined in Eq. (4.7). Although this does not help the actual computations, it is possible to see that the terms $\delta\mathcal{P}$ and $\eta_2\delta\mathcal{C}_2$ differ only by the leading coefficients PL and η_2. The same holds for $\delta\mathcal{F}$ and $\eta_3\delta\mathcal{C}_3$, with the coefficients being FL and η_3. This means that once the relevant Lagrange multipliers are found, it is possible to directly recover the required transverse and

longitudinal forces to keep the beam at the configuration of interest.

The practical value that this approach brings to the problem is that with a force value guess, the beam might attain stability at two or more completely different configurations, making it hard to predict the height ratio for that specific quantity. This is because as the later sections show, the graph of H/L vs. F is not one to one even in very small compression values. On the other hand, when the constraints along with their Lagrange multipliers are implemented, the uncertainty about the length or height disappears, helping reach the desired solution faster. This is the main advantage of the formulation proposed here compared to the formulation used in [27], where the forces are unknown. Though it should be clarified that in [27], the abscissa of the force application point is assumed to be given in the deformed configuration whereas here it is modeled as a fixed point in the initial configuration. The difference is quite trivial, since the library used to implement this model is flexible enough to adapt to that scenario without much hassle.

Next, the equations are written down explicitly. Standard procedure is followed: the terms inside the integral with $\delta\Lambda$ and $\delta\theta$ coefficients are gathered together. That is,

$$\begin{aligned} &\Big[K_\Lambda L\left[\Lambda - 1\right] + \left[\eta_1 + \mathbb{1}_{\xi_0}\eta_3\right]\sin\theta + \eta_2\cos\theta\Big]\,\delta\Lambda = 0 \\ &\Big[-\frac{K_\Lambda}{L}\theta'' + \left[\eta_1 + \mathbb{1}_{\xi_0}\eta_3\right]\Lambda\cos\theta - \eta_2\Lambda\cos\theta\Big]\,\delta\theta = 0. \end{aligned} \tag{4.15}$$

The equations in (4.15) hold for all admissible $\delta\Lambda$ and $\delta\theta$, thus the terms in parantheses have to be equal to zero. Although originally there are two unknowns, namely Λ and θ, it is possible to express Λ in terms of θ and write θ in a separate second order non-linear differential equation. Isolating Λ in the first equation of (4.15) by simply subtracting the other terms from both sides yields

$$\Lambda = \frac{1}{K_\Lambda L}\Big[K_\Lambda L - \left[\eta_1 + \mathbb{1}_{\xi_0}\eta_3\right]\sin\theta - \eta_2\cos\theta\Big]. \tag{4.16}$$

Then, substituting the value of Λ from (4.16) into the second equation in (4.15)

results with

$$\theta'' = \frac{1}{K_\Lambda K_\theta}\left[K_\Lambda L - [\eta_1 + \mathbb{1}_{\xi_0}\eta_3]\sin\theta - \eta_2\cos\theta\right]\left[[\eta_1 + \mathbb{1}_{\xi_0}\eta_3]\cos\theta - \eta_2\sin\theta\right] \tag{4.17}$$

along with the relevant boundary conditions for θ and the additional constraints described in (4.11). Note that now the formulation of zero transverse force problem can be reduced to a special case of (4.17). Setting $\eta_3 = 0$ and getting rid of constraint $\mathcal{C}_3$ gives the result.

4.5 Numerical implementation

Numerical implementation of Eq. (4.17) is done with the open source ODE solver CVODES [28]. CVODES is a non-linear initial value ODE system solver with additional sensitivity analysis capabilities. In order to use any initial value problem library to solve the boundary value problem of interest, an iterative method has to be performed. In this case, non-linear shooting method is used not only to find the unknown initial value of $\theta(0)$ and $\theta'(0)$ (for double hinged and double clamped problems, respectively), but also to find the values of the Lagrange multipliers η_1, η_2 and η_3 simultaneously.

There are two different sensitivity capabilities that CVODES provides, which are used extensively to solve the equations (4.11) and (4.17). First of these functionalities is the forward sensitivity analysis (FSA). FSA is used to find the sensitivities of θ and θ' at some fixed points (in this case points ξ_0 and 1) with respect to problem parameters η_1, η_2, η_3 and the initial value $\theta(0)$ or $\theta'(0)$. The other functionality is the adjoint sensitivity analysis (ASA). ASA is used to compute the values $\partial\mathcal{C}_i/\partial\eta_j, i, j \in \{1, 2, 3\}$ and also the sensitivites of $\mathcal{C}_i, i \in \{1, 2, 3\}$ with respect to the unknown initial value. CVODES also has the functionality to compute any additional quadratures, so at each step the values of $\mathcal{C}_i$ are known.

In both problem types, the initial step is to compute the modified buckling problem in which the $\mathcal{C}_3$ constraint is relieved. The solution to this particular

problem is the one where no transverse force F is present. An initial set of values is guessed and the problem is solved for a small compression value $\frac{\Delta L}{L}$. Then the parameter set found after the solution of this first problem is used as the guess for the second, higher compression value. The pseudocode is as follows:

Algorithm 1 Relaxed buckling solution - $H = H_0$

```
θ(0) ← initial guess                    ▷ Green coloured lines for double hinged
θ'(0) ← initial guess                   ▷ Blue coloured lines for double clamped
η1 ← 0
η2 ← π²EI/(K²L)                         ▷ Use crit. value from linear theory
for ΔL ← ΔL1 to ΔLf do
    while err > ε do
        A ← ∂(C1, C2, θ'(1))/∂(η1, η2, θ(0))
        b ← (C1, C2, θ'(1))
        A ← ∂(C1, C2, θ(1))/∂(η1, η2, θ'(0))
        b ← (C1, C2, θ(1))
        err ← ||b||
        solve Ax = b
        update values
    end while
    write values to a file
end for
```

The potential problem with this implementation is the possibility to converge to higher order modes of buckling. However, a couple of observations help to overcome this. First, the η_1 value associated to the first mode is always equal to 0. So a non zero value immediately tells the user that a higher order mode is found. Hence, it makes sense to set η_1 to 0 in the first iteration. The second observation is that for small compression values, the critical force that the linear theory suggests for the particular problem is a good enough initial guess. However, no general initial guess methodology was found for $\theta(0)$ or $\theta'(0)$ values and providing a well enough guess for those values remains the only challenging part in this approach.

The next step is to sweep through the height ratio values $0 \leq H/L \leq H_0/L$ while fixing the compression ratio $\Delta L/L$. A problem arises for both type of supports in this situation. At first sight, gradually decreasing H/L would seem to be the natural thing to do but this method incorrectly follows a higher energy

path than the actual progress does. To circumvent this problem, the parameter set that was found in the previous part is modified to directly solve the state with $H/L = 0$. After this case is solved, H/L is gradually increased back to H_0/L and the correct result is obtained.

Algorithm 2 Transverse force implementation - Clamped

$\Delta L \leftarrow$ `fix value`
$\theta'(0), \eta_1, \eta_2 \leftarrow$ `read saved values`
$\eta_3 \leftarrow 0$
$(\theta'(0), \eta_2) \leftarrow 1.5 \times (\theta'(0), \eta_2)$
$H \leftarrow 0$
while $err > \epsilon$ **do**
    $A \leftarrow \partial(\mathcal{C}_1, \mathcal{C}_2, \mathcal{C}_3, \theta(1))/\partial(\eta_1, \eta_2, \eta_3, \theta'(0))$
    $b \leftarrow (\mathcal{C}_1, \mathcal{C}_2, \mathcal{C}_3, \theta(1))$
    $err \leftarrow \|b\|$
    `solve` $Ax = b$
    `update values`
end while
for $H \leftarrow 0$ to H_f **do**
    while $err > \epsilon$ **do**
        $A \leftarrow \partial(\mathcal{C}_1, \mathcal{C}_2, \mathcal{C}_3, \theta(1))/\partial(\eta_1, \eta_2, \eta_3, \theta'(0))$
        $b \leftarrow (\mathcal{C}_1, \mathcal{C}_2, \mathcal{C}_3, \theta(1))$
        $err \leftarrow \|b\|$
        `solve` $Ax = b$
        `update values`
    end while
    `save values`
end for

The problem with the both configurations is summarized in Fig. 4.3. After the problem with zero transverse force is solved, while the height is decreased step by step there comes a bifurcation point at which a second solution set that has a lower energy emerges and diverges from the original one. The higher energy solution has mirror symmetry with respect to the center, while the lower energy solution breaks this symmetry. It was found out that the implementation had a tendency to follow the higher energy solution when H/L was reduced to 0 from H_0/L, thus giving incorrect results in terms of what is matching the reality. To circumvent this, using the zero transverse force H_0 solution, the problem with $H = 0$ is solved directly. The parameter set is adjusted accordingly so that the

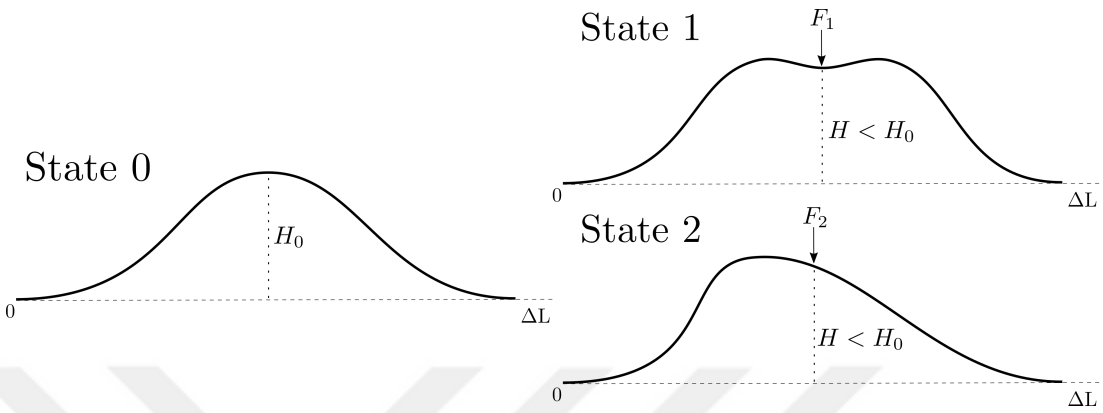

Figure 4.3: The two possible local minima for the double clamped beam when the height is reduced. State 2 corresponds to the lower energy solution while State 1 represents the higher energy solution, which is unrealistic. Comparatively, $F_1 > F_2$ and the boundary forces are much higher.

Support Type	Physical	$\Delta L/L$	Non-physical
Hinged	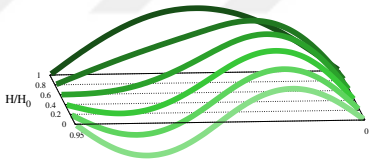	0.05	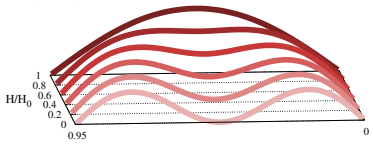
Clamped	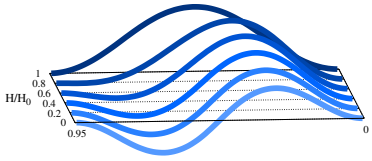		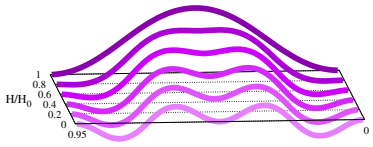
Hinged	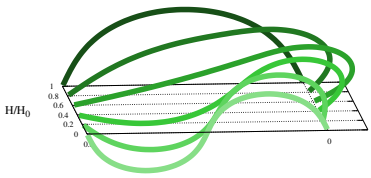	0.40	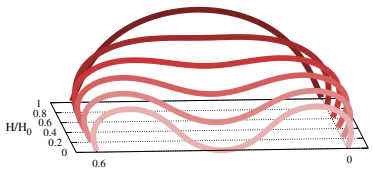
Clamped	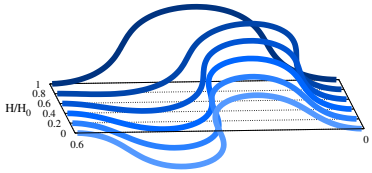		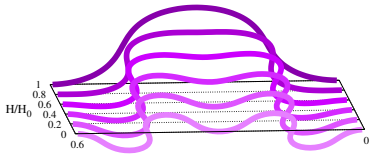

Table 4.1: Physical and non-physical buckled beam deformations of hinged and clamped beams.

result found in this step is the actual solution on the lower energy branch. Then, the height H is increased *back to* the original height H_0. The low energy transition passes through the second mode of the buckled beam. This is expected since it is actually the second lowest energy state for the buckled beam when there is no transverse force.

A sample group of transition graphs between bistable states for both types of beams can be seen in Fig. 4.1. It can be seen that the lower energy beams lose the symmetry with respect to the middle plane early on, while the higher energy solutions preserve it as the transition proceeds.

Fig. 4.4 shows the bifurcation diagrams of end-shortening vs. compressive load. The loads are normalized to the respective critical loads of the support types. In the graphs first mode branches are generated by lifting the restriction $\mathcal{C}_3$ from the the equations which enforce a particular H/L ratio. Without this ratio present the first mode of buckling is easily generated. On the contrary, second mode diagrams are generated by enforcing $H/L = 0$ at each step while varying the compression ratios. It can be observed that reaching the buckling point for the second mode requires proportionally more force for hinged beams compared to clamped ones, i.e. 4 times the load of first mode buckling critical force is required for hinged beams to buckle into the second mode whereas this ratio is 2 for double clamped beams. It can also be seen that double clamped beams begin to exhibit negative stiffness against P around $\Delta L/L = 0.5$ and that the force associated to the first mode actually exceeds that of second mode around $\Delta L/L = 0.7$.

In this section, some comparisons between the results obtained from the formulation discussed in the previous sections and finite element model are presented. The model of interest is chosen to be a silicon nanobeam with a length of 40µm and a cross section of 200nm × 200nm. In addition to the analysis focusing only on the existence of bulk parameters, a study that takes surface parameters into account is also presented. The bulk parameter is modeled after silicon, whose Young's Modulus has an approximate value of 165GPa and has a typical Poisson's ratio of 0.25. The surface is modeled after SiO_2 which has a Young's Modulus

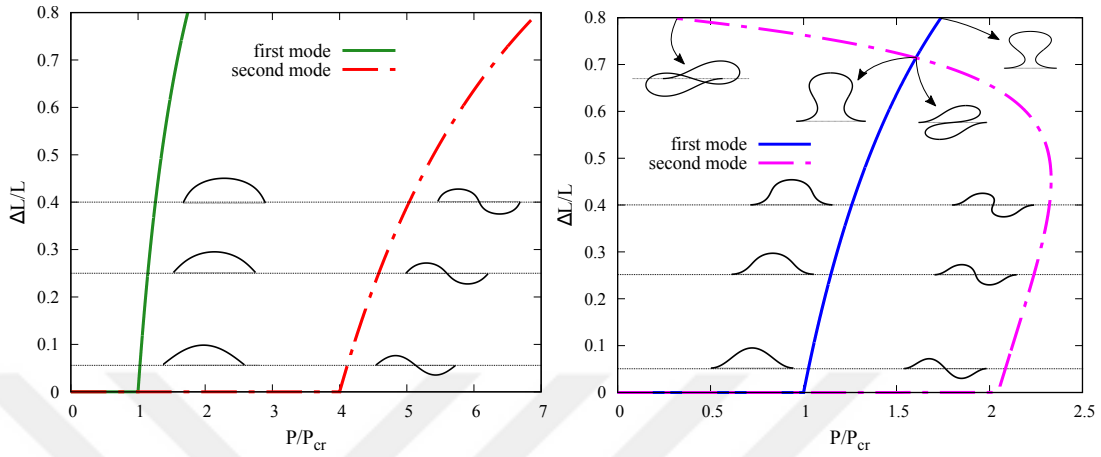

(a) Bifurcation diagram for hinged beams. $P_{cr} = \pi K_\theta / L^2$.

(b) Bifurcation diagram for clamped beams. $P_{cr} = \pi K_\theta / 4L^2$.

Figure 4.4: End-shortening vs. compressive load. Compressive load is normalized to critical load that is determined from linear theory. Beam properties same with those in 4.5. Mode shapes drawn for $\Delta L/L = 0.05$, 0.25, and 0.40 for both support types in addition to $\Delta L/L = 0.714$ and 0.8 for double clamped beams.

around 103GPa. With a surface coating thickness of 1.5nm, this corresponds to the surface parameters $\widehat{\lambda} = 43$Pa and $\widehat{\mu} = 38$Pa, since $\widehat{E} = E_s \times \Delta t$. Bending stiffness of the surface is modeled like it is done in [2].

In table 4.2, a convergence study for the finite element model, along with the results obtained from the numerical implementation of the model developed in the previous sections can be found. The values in the table are the computed forces corresponding the various height values H at the fixed compression ratio of $\Delta L/L = 0.15$. For the specific compression ratio, maximum value of H is found to be $H_0 = 0.23466$.

It can be seen that the linear elements yield high error compared to the quadratic elements, even though the aspect ratio of some quadratic elements are worse than that of linear elements'. Each element in the 640 element model has an aspect ratio of 1:2.5 compared to 1:1.25 that the 1280 element model has. However the results in the table show that the former is sufficiently accurate.

Due to time constraints 640 element quadratic model was used in the consequent studies instead of the better 1280 element model. For instance, sweeping

		Linear Elements			Quadratic Elements			Analytical
	H/L	320	640	1280	320	640	1280	
Bulk								
	0.05	5.52982	2.58335	1.84802	1.56706	1.56422	1.56361	1.56339
	0.10	11.1245	5.19678	3.71752	3.15254	3.14663	3.14539	3.14500
	0.20	23.2732	10.8671	7.77292	6.59528	6.57919	6.57630	6.57584
Bulk & Surface								
	0.05	5.59261	2.62912	1.84802	1.60686	1.60397	1.60336	1.60260
	0.10	11.2508	5.28885	3.71752	3.23261	3.22660	3.22536	3.22389
	0.20	23.5374	11.0596	7.77292	6.76273	6.74642	6.74349	6.74080

Table 4.2: Transverse reaction force $F/10^{-7}$ in N for various H/L and fixed $\Delta L/L = 0.15$. Beam size of 200nm $\times$ 200nm $\times$ 40µm. $\lambda = 6.6$ GPa, $\mu = 6.6$ GPa, $\widehat{\lambda} = 43$ Pa, $\widehat{\mu} = 38$ Pa. 4 elements on the cross section, varying among the length of the beam.

through the range $H = 0 \rightarrow H_0$ with $\Delta L/L = 0.25$ requires applying the displacement increments approximately 1200 times. Solving each of these nonlinear problems takes around 1.2 and 3 seconds for 640 element model and 1280 element model, respectively. Also, since the nodes are more frequent along the length of the beam in the latter model, the number of displacement increments have to be approximately twice as much during the initial compression stage. This means that using 640 element model is much more feasible while not sacrificing much of the accuracy, as the study shows.

Next, actual graphs comparing the results obtained from FEM and numerical implementation are presented. In each graph, both the bulk energy and bulk & surface energy comparisons are presented.

Fig. 4.5 shows that the numerical model adopted matches the nonlinear finite element model to a high level of accuracy even when high compression ratios are applied. The finite element model considered here is both geometrically and materially nonlinear. The thickness of the surface layer, along with the material parameters for silicon dioxide result in only a slight variation of computed transverse force though for other materials the results may vary.

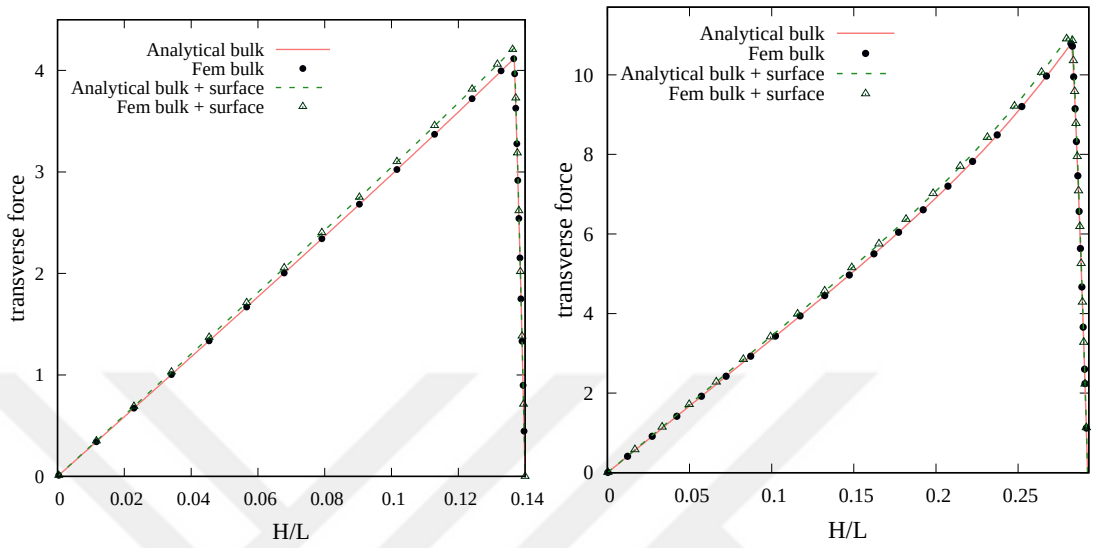

(a) $\Delta L/L = 0.05$ (b) $\Delta L/L = 0.25$

Figure 4.5: Finite element and numerical implementation comparisons of double clamped beam. Y axis represents transverse reaction force $F/10^{-7}$ in N. X axis represents height ratio H/L.

One has to verify that the strain levels developed in the analytical model reside in the proportionality limits as to ensure that linear material response assumption is valid. To demonstrate that this is the case for both $\Delta L/L$ values considered, we show that the maximum of E_{zz}, E_{zy} and E_{yy} values are in the acceptable range. Here, $\boldsymbol{E}$ is the Green-Lagrange strain tensor, i.e. $\boldsymbol{E} = \boldsymbol{F}^{\mathrm{t}} \cdot \boldsymbol{F} - \boldsymbol{I}$ and z and y are the longitudinal and transverse direction of the beam, respectively.

Fig. 4.6 shows the maximum strain levels developed inside the beam. It is expected that higher $\Delta L/L$ values result in increased levels of strains, and the graphs confirm this. The maximum amount of normal strains developed in the beams are below 3% even for $\Delta L/L = 0.25$. According to the work presented in [29], normal strain levels below 3% are well inside the proportionality limit for silicon nanobeams, which confirms that the analytical model is successfull in predicting the behavior of silicon nanobeams. The transverse shear is in general an order of magnitude smaller, which confirms the validity of the linearity assumption.

Next, we present force and energy plots that are obtained by sweeping the full

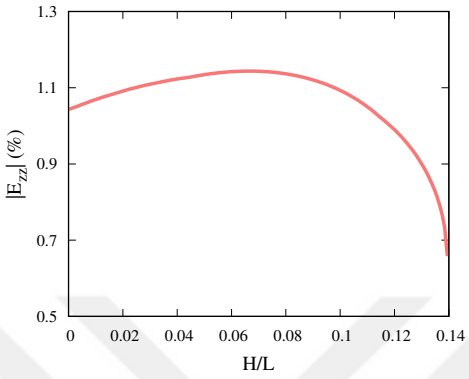

(a) E_{zz} for $\Delta L/L = 0.05$

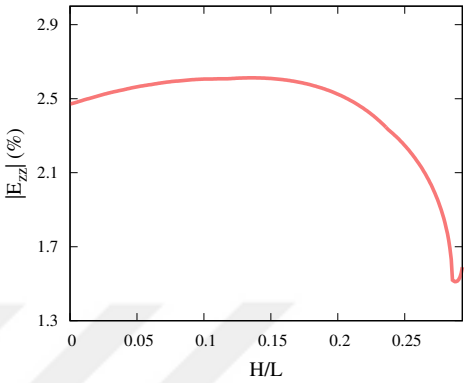

(b) E_{zz} for $\Delta L/L = 0.25$

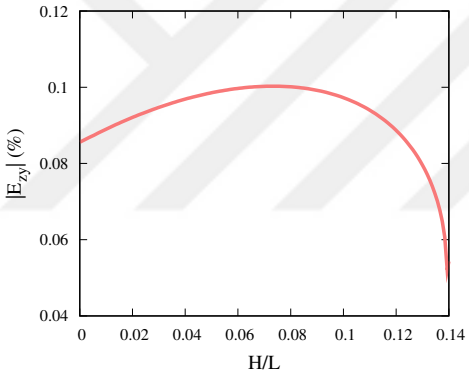

(c) E_{zy} for $\Delta L/L = 0.05$

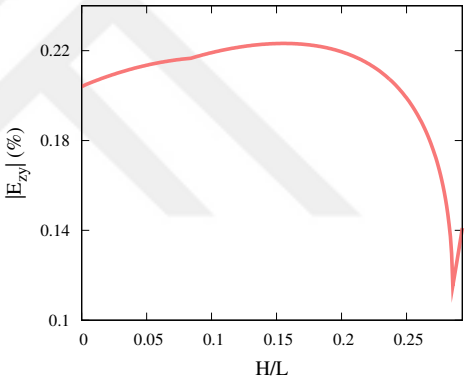

(d) E_{zy} for $\Delta L/L = 0.25$

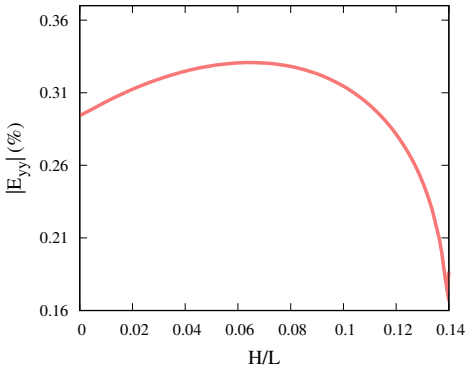

(e) E_{yy} for $\Delta L/L = 0.05$

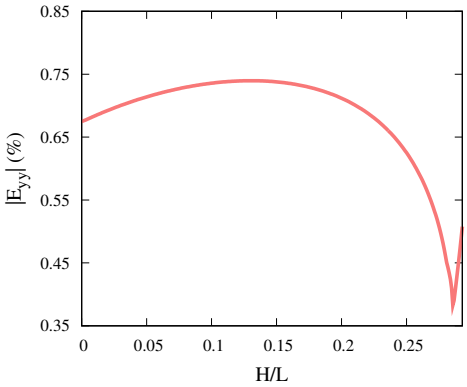

(f) E_{yy} for $\Delta L/L = 0.25$

Figure 4.6: Absolute value of maximum strains developed inside the beams at various H/L values according to the nonlinear finite element model. Strains denoted in percents. Axes z and y denote the longitudinal and transverse directions of the beam, respectively.

range of $0 \leq H_0/H \leq 1$ for 20 different $\Delta L/L$ values between 0.05 and 0.40.

Before proceeding further, some performance results may give a better idea about the advantage that the analytical model has over the finite element code. Sweeping for 20 different values for $0.005 \leq \Delta L/L \leq 0.400$ with 50 equally spaced $0 \leq H/H_0 \leq 1$ takes around 4 seconds for the numerical implementation to complete. On the other hand FEM model takes around 20 minutes to complete for a fixed $\Delta L/L$ value, on average. This means that replicating the graphs in the next section would take at least 5 hours for the FEM, excluding the user interrupts.

The finite element meshes for two compression ratio values are depicted in figure 4.7. Note that the length of the buckled beams are not equal in reality.

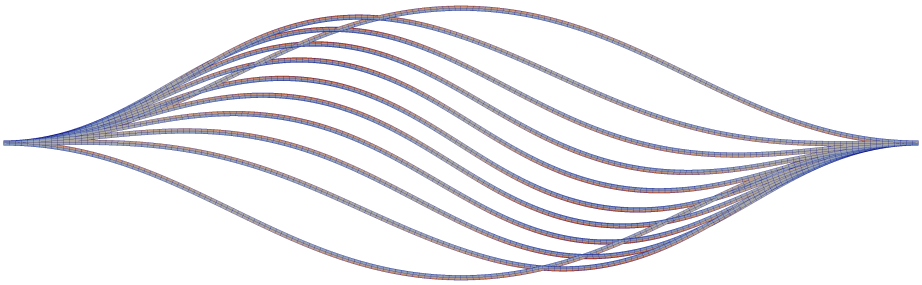

(a) FEM model. $\Delta L/L = 0.05$

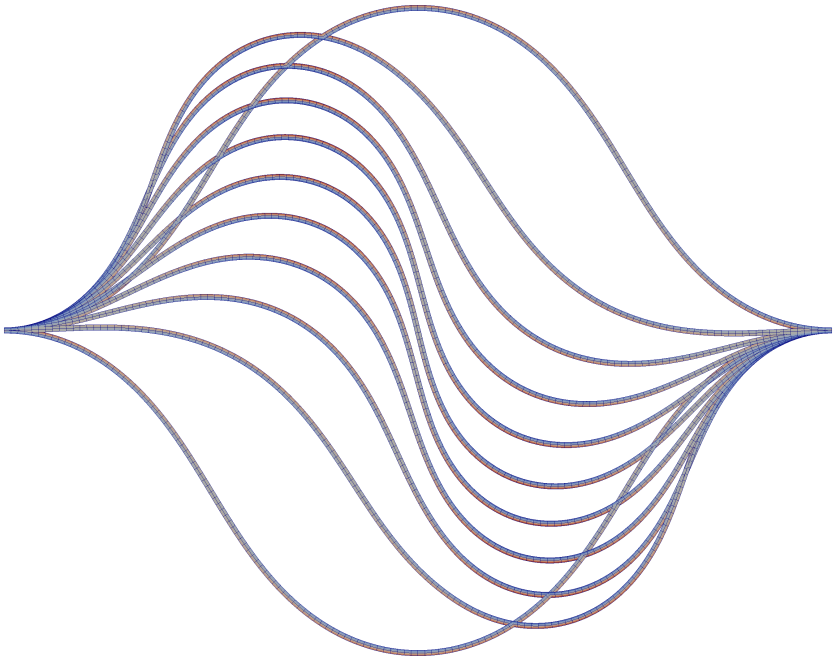

(b) FEM model. $\Delta L/L = 0.25$

Figure 4.7: Snap-through behavior observed in FEM model.

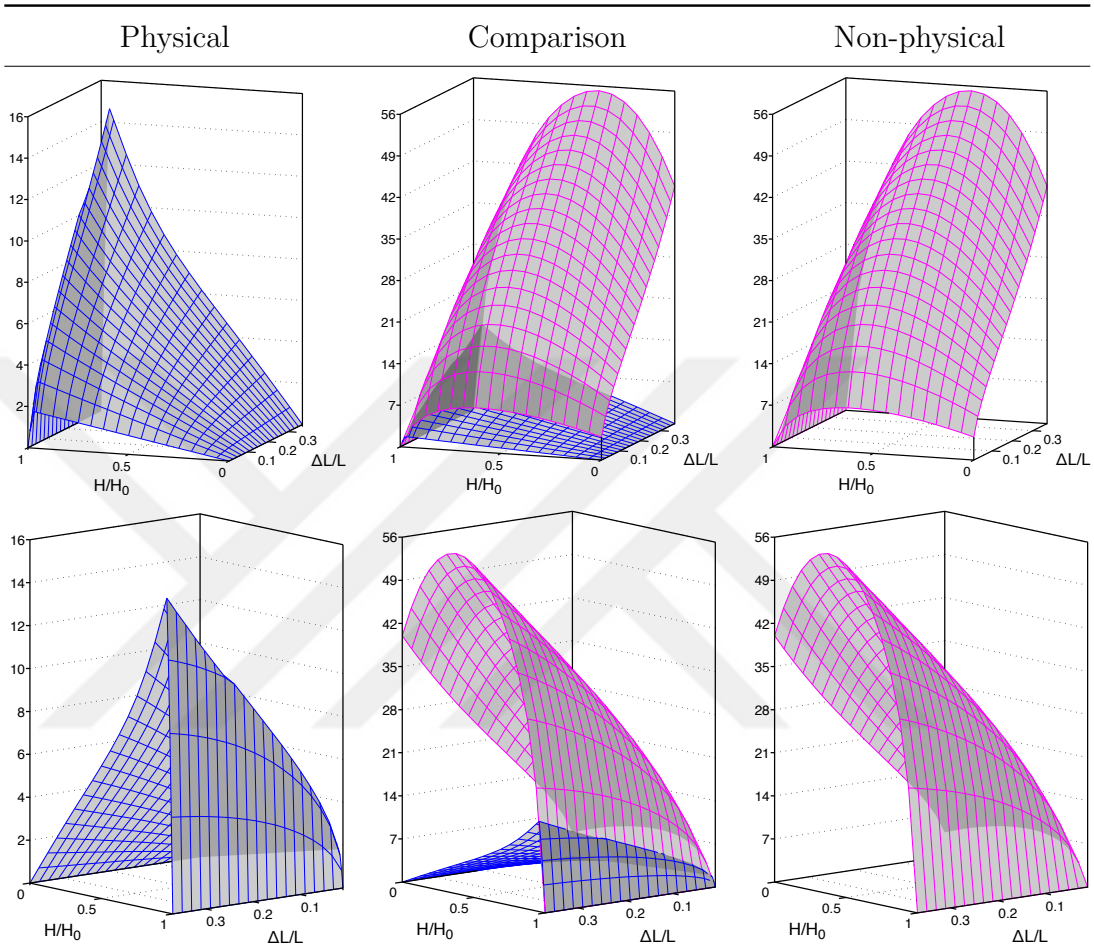

Table 4.3: Transverse reaction force $F/10^{-7}$ in N for clamped beams. Blue colours depict the high energy non-physical solutions while purples depict the lower energy physical ones.

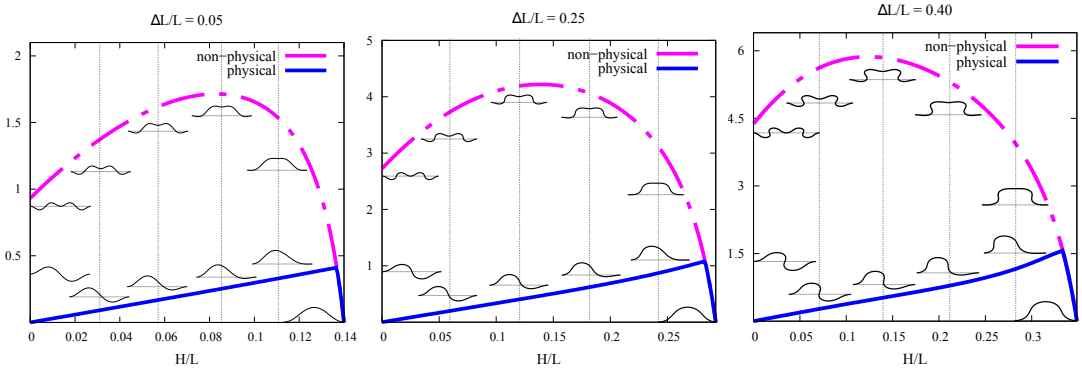

(a) $\Delta L/L = 0.05$ (b) $\Delta L/L = 0.25$ (c) $\Delta L/L = 0.40$

Figure 4.8: F vs. H/L graphs for clamped beams for various $\Delta L/L$ values.

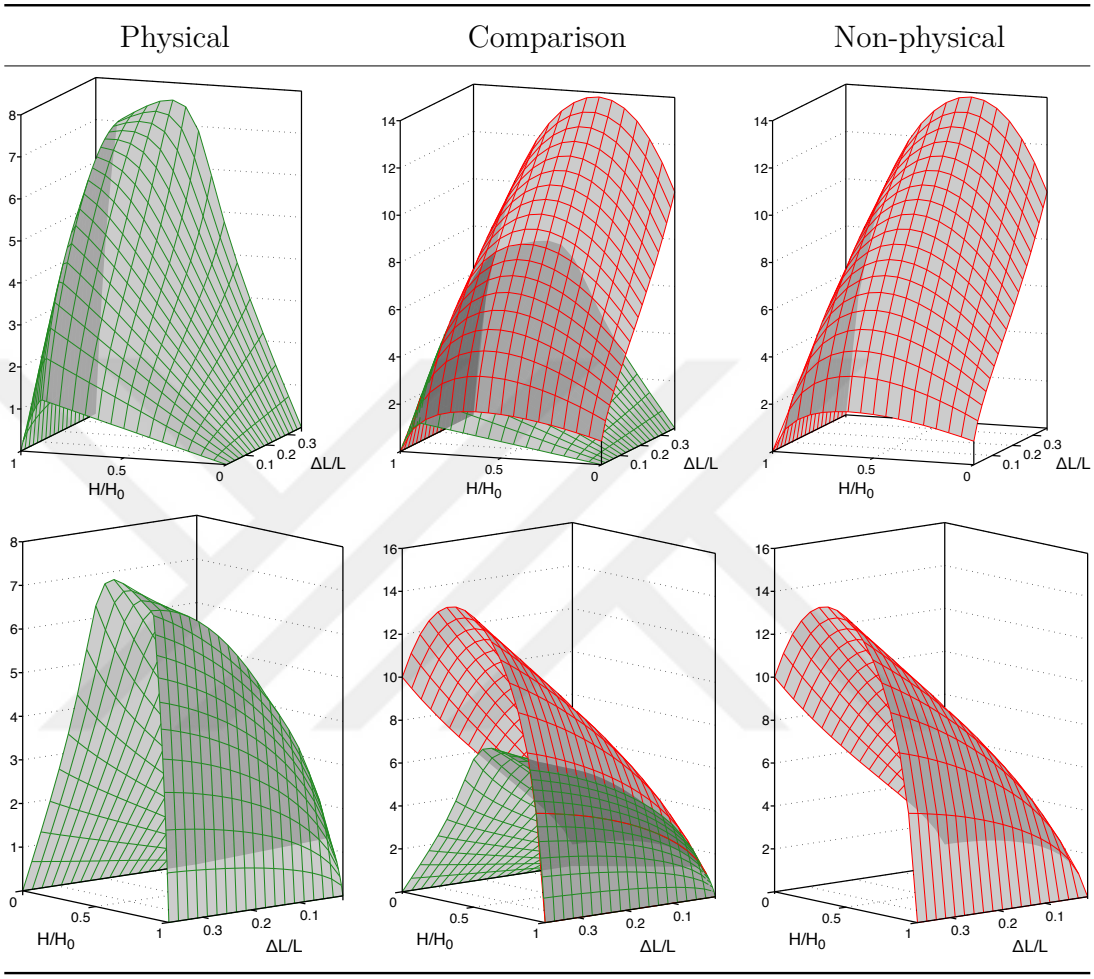

Table 4.4: Transverse reaction force $F/10^{-7}$ in N for hinged beams. Red colours depict the high energy non-physical solutions while greens depict the lower energy physical ones.

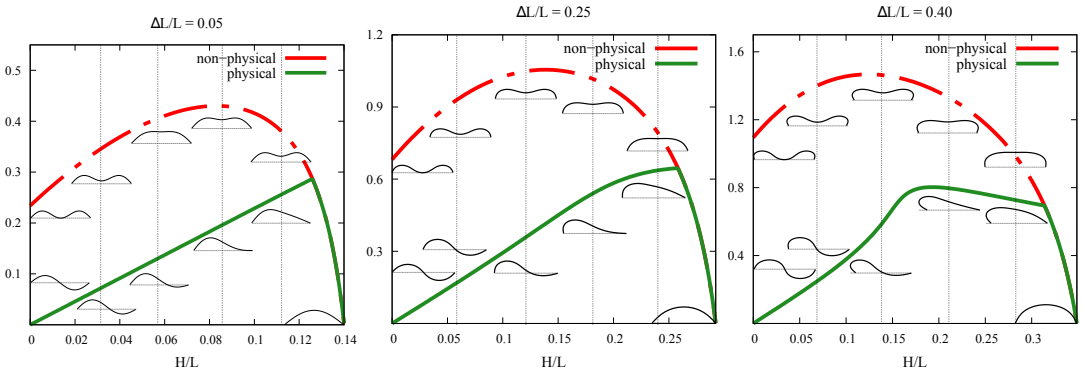

(a) $\Delta L/L = 0.05$ (b) $\Delta L/L = 0.25$ (c) $\Delta L/L = 0.40$

Figure 4.9: F vs. H/L graphs for hinged beams for various $\Delta L/L$ values.

Tables 4.3 and 4.4 show the surface plots which map a given $\Delta L/L$ and H/H_0 value (where $0 \leq H \leq H_0$) to their corresponding transverse force F. To increase clarity, each surface is shown from two different angles in separate rows of the table. Fig. 4.8 and 4.9 are two dimensional plots that show the progression of H/L vs F for three fixed compression ratio values of $\Delta L/L = 0.0.5$, 0.25, 0.40. These figures also include the profiles of the beams along differing H/L values.

An initial observation that is valid for all $\Delta L/L$ values is that the onset of bifurcation is much earlier (considered when H/H_0 is decreased) for double clamped beams compared to double hinged beams. Because of this fact, externally influencing a clamped beam to follow the higher energy path is more difficult than doing the same for a hinged beam. This can also be seen in the later figurs that compare the internal stretch and bending energies of the beams.

The decreasing transverse force (reported as negative stiffness) after bifurcation point is one of the typical properties of snap-through behavior. This trend is also observed to both types of beams but it can be seen that for sufficiently high compression values, the double hinged beam actually starts to have a positive stiffness just after the bifurcation point, up to some value. Figure 4.9c illustrates this. This behavior is not observed on the clamped beams, however.

Similar transverse force graphs for hinged beams can be found in [27, 26], which also include high energy transitions in the graphs along with physical solutions. For double clamped beams, one may refer to [30, 31].

Physical	Comparison	Non-physical

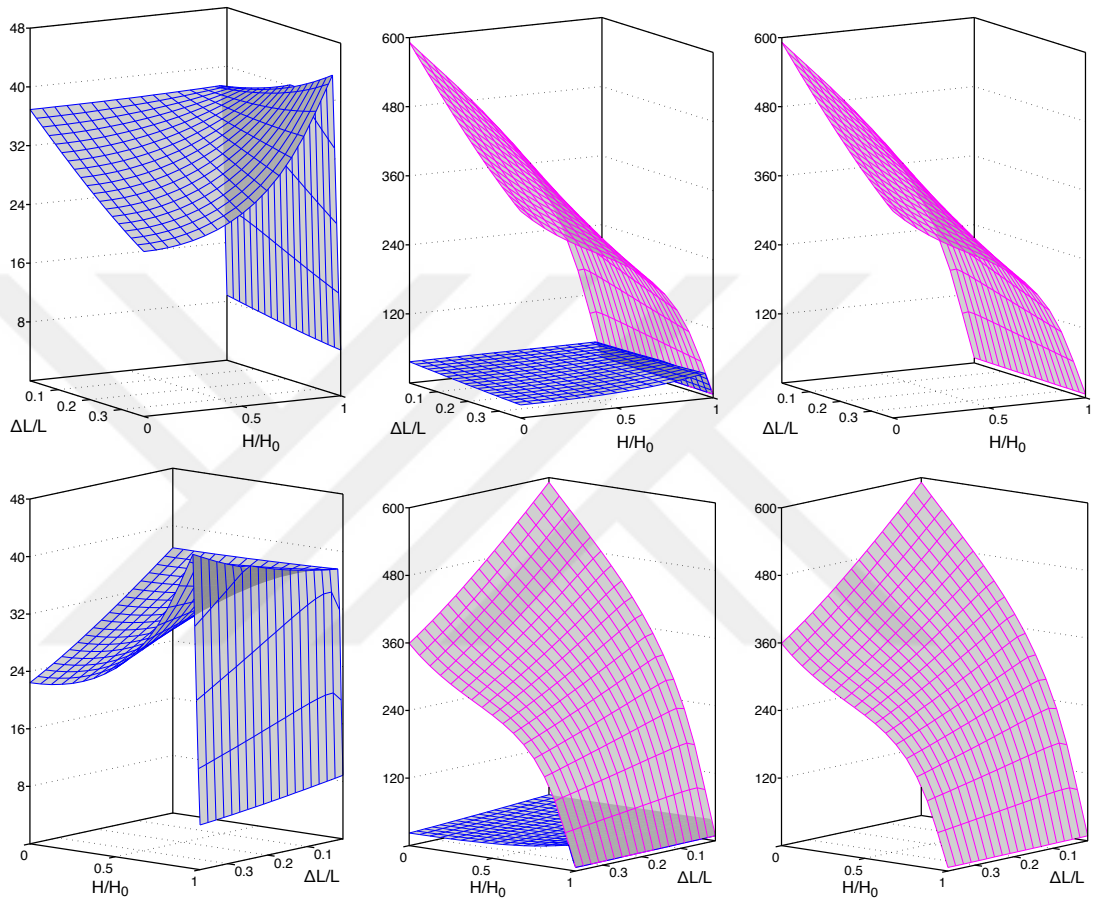

Table 4.5: Stretch energy $E_\Lambda/10^{-16}$ in J for clamped beams.

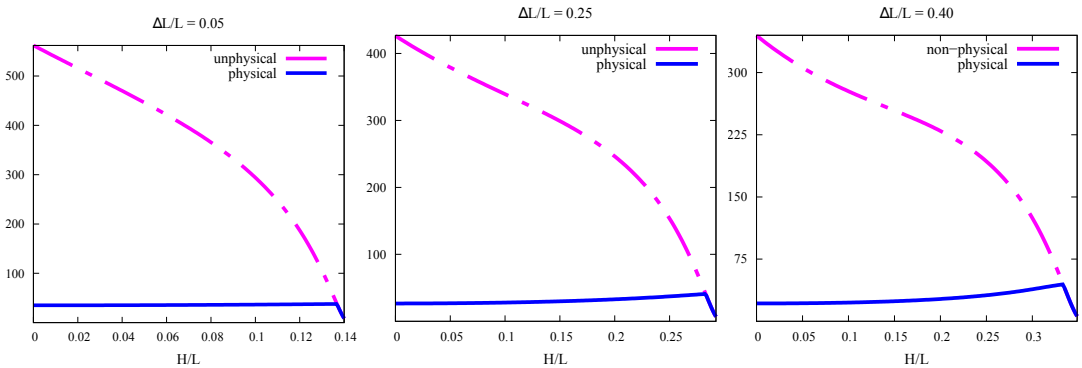

(a) $\Delta L/L = 0.05$ (b) $\Delta L/L = 0.25$ (c) $\Delta L/L = 0.40$

Figure 4.10: H/L vs. E_Λ graphs for clamped beams for various $\Delta L/L$ values.

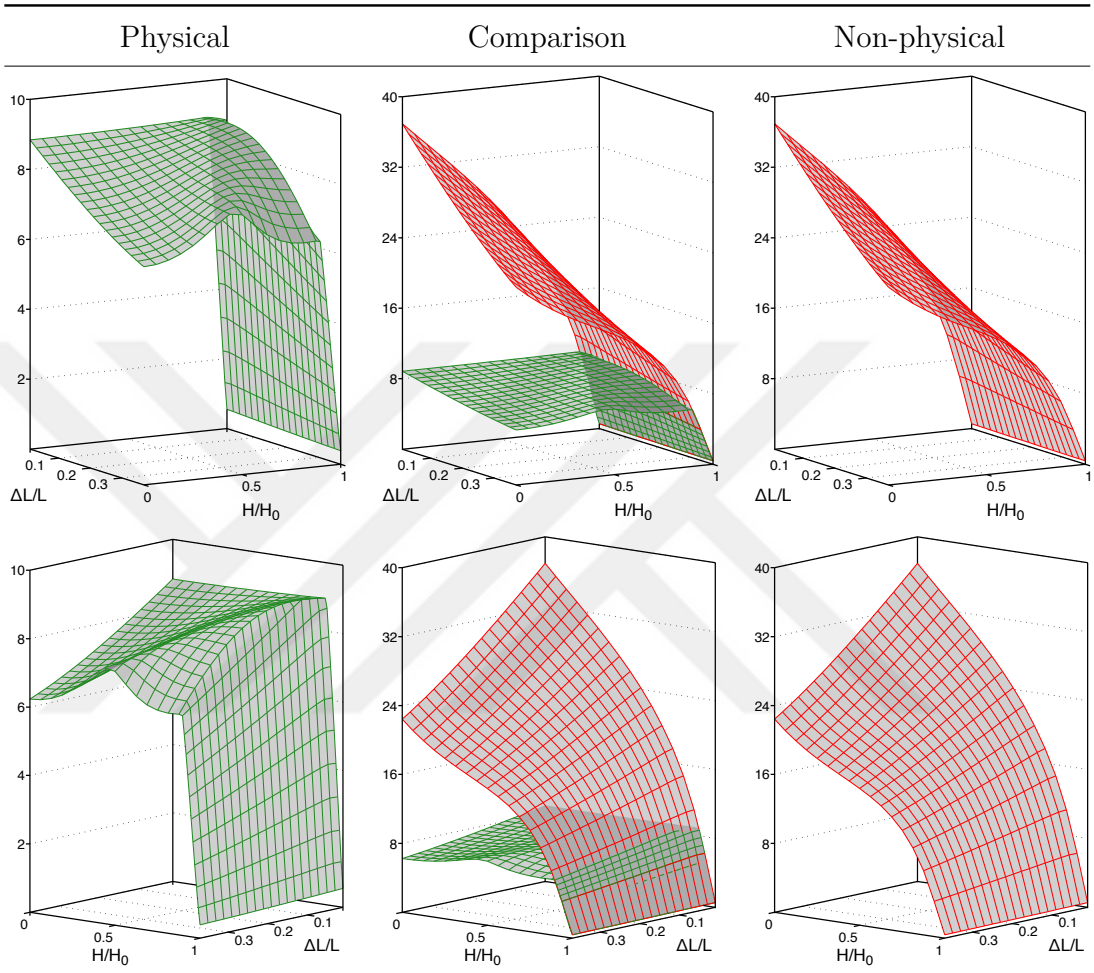

Table 4.6: Stretch energy $E_\Lambda/10^{-16}$ in J for hinged beams.

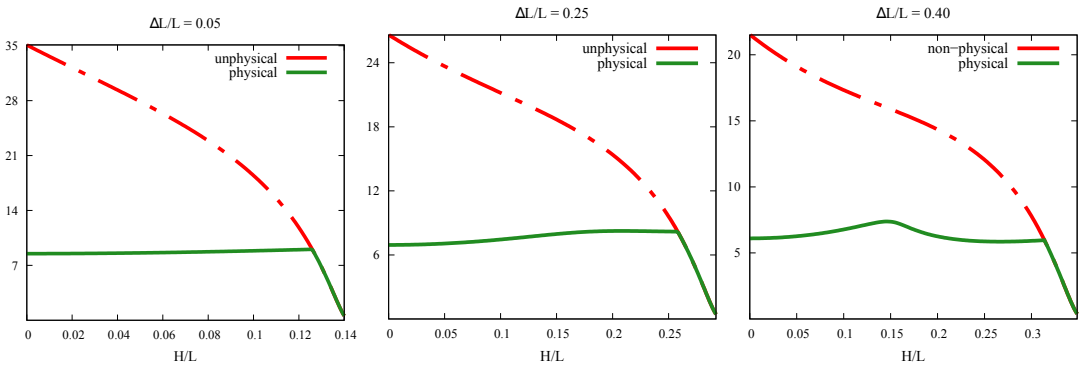

(a) $\Delta L/L = 0.05$ (b) $\Delta L/L = 0.25$ (c) $\Delta L/L = 0.40$

Figure 4.11: H/L vs. E_Λ graphs for hinged beams for various $\Delta L/L$ values.

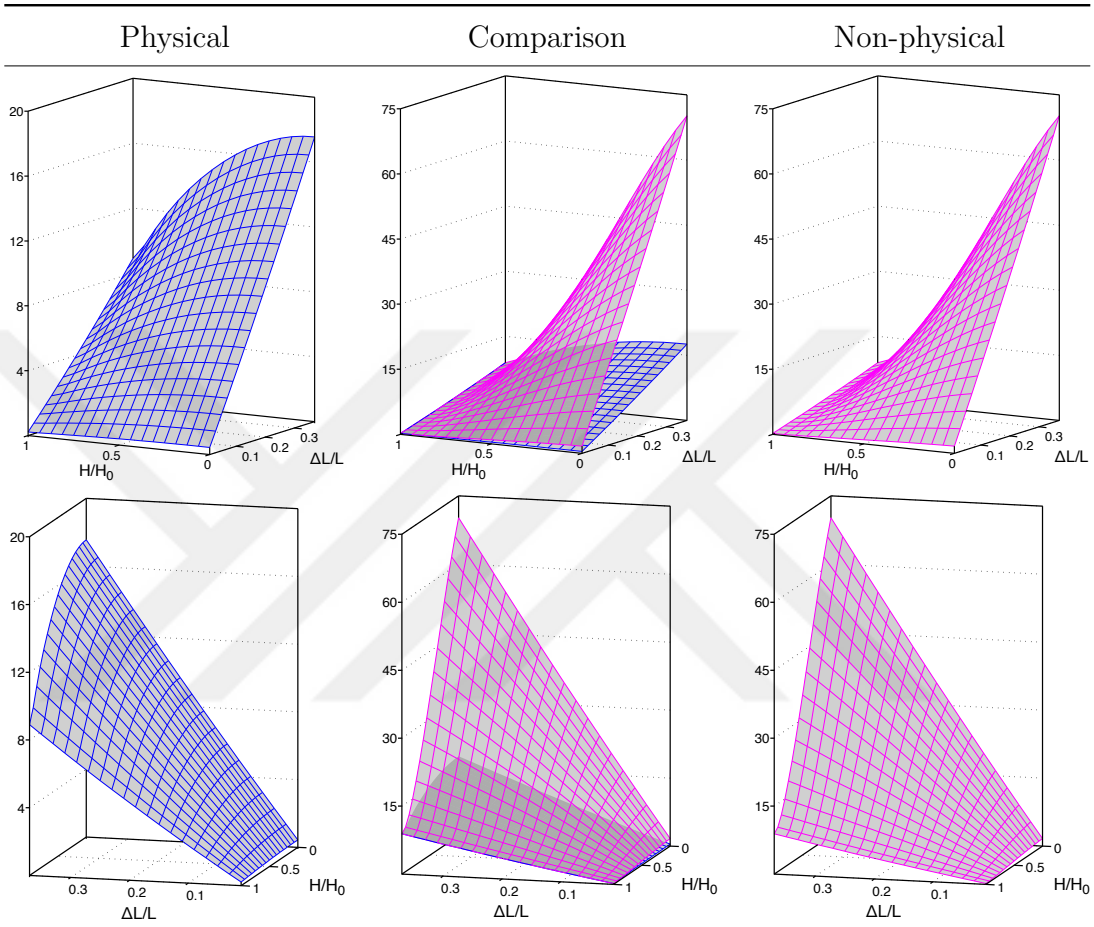

Table 4.7: Bending energy $E_\theta/10^{-12}$ in J for clamped beams.

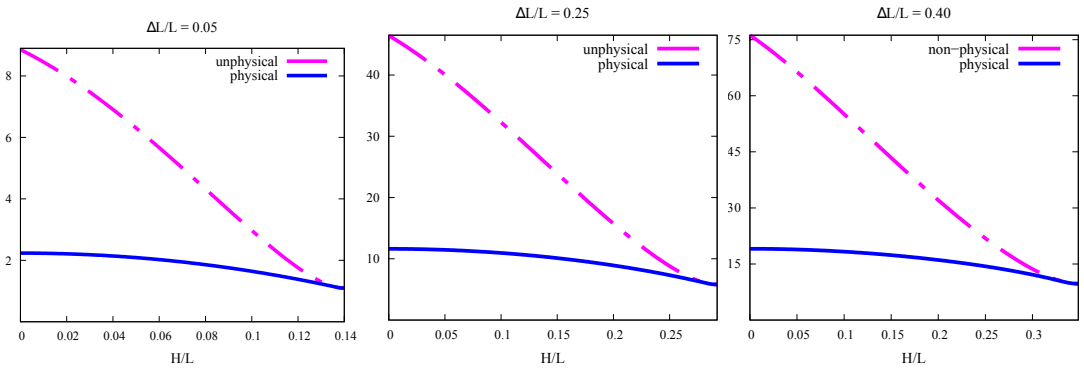

(a) $\Delta L/L = 0.05$ (b) $\Delta L/L = 0.25$ (c) $\Delta L/L = 0.40$

Figure 4.12: H/L vs. E_θ graphs for clamped beams for various $\Delta L/L$ values.

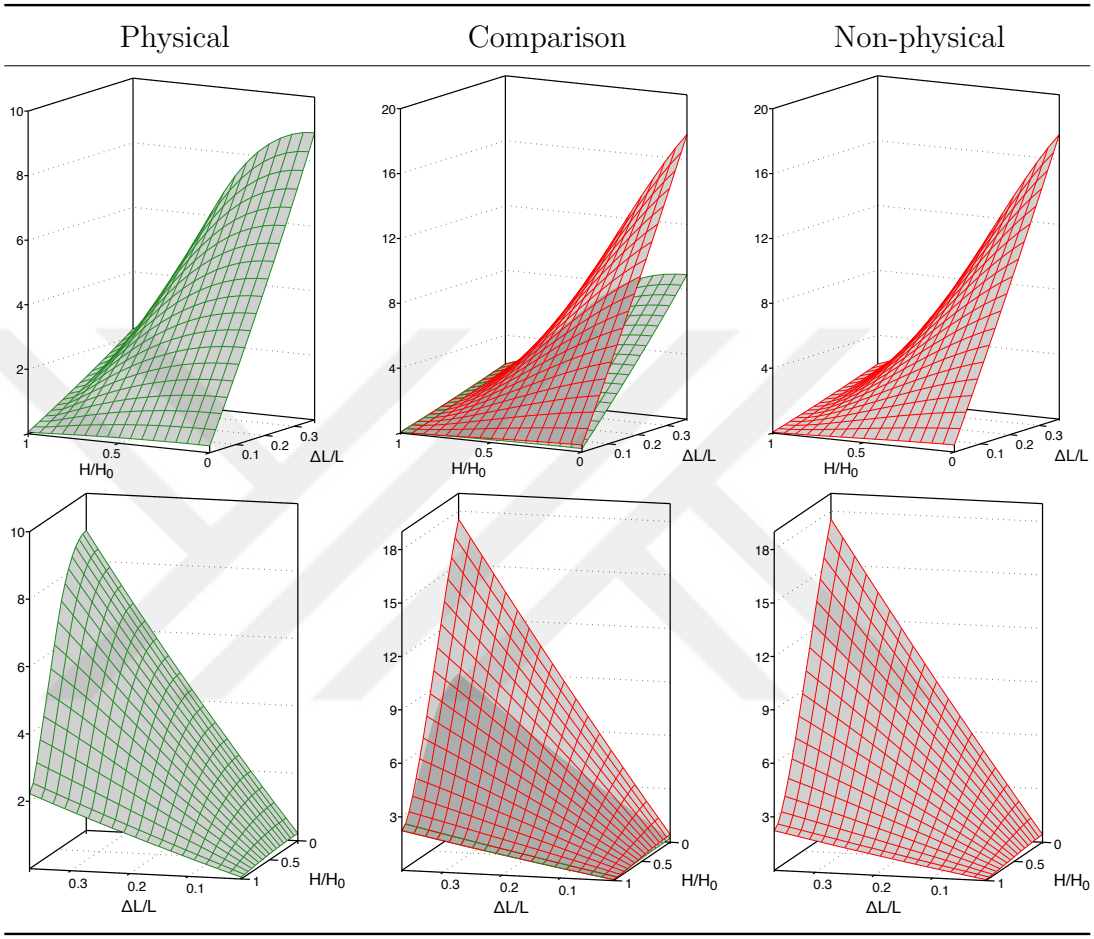

Table 4.8: Bending energy $E_\theta/10^{-12}$ in J for hinged beams.

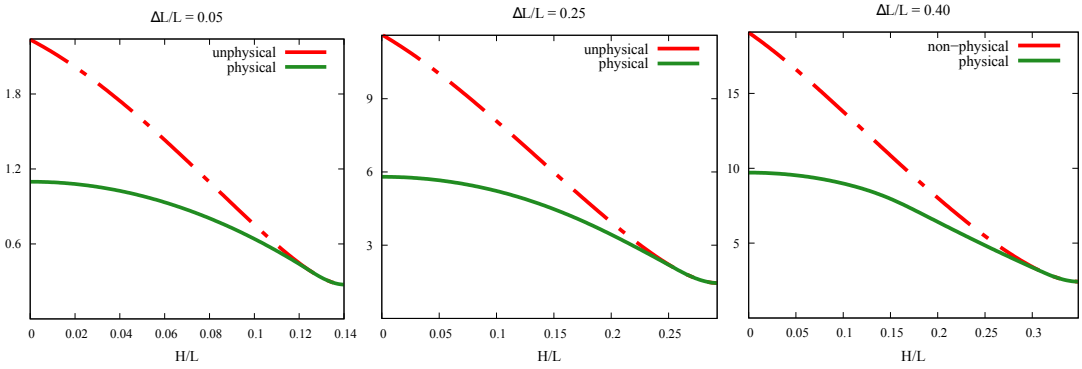

(a) $\Delta L/L = 0.05$ (b) $\Delta L/L = 0.25$ (c) $\Delta L/L = 0.40$

Figure 4.13: H/L vs. E_θ graphs for hinged beams for various $\Delta L/L$ values.

It can be seen from Fig. 4.5 through 4.8 that the dominant part of energy in high compression values comes from bending. This is of course a function of the amount of buckling: at the onset of buckling the bending energy is non existent but becomes more prominent as the beam buckles more. Bending energy graphs suggest that the ratio between non-physical and physical energies is higher for double clamped beams, as opposed to double hinged beams: this ratio is close to 4 for clamped beams and 2 for hinged supports. This reassures that forcing the beam to follow the higher energy states with the assistance of some additional external factors is more difficult for double clamped beams. Likewise, the bifurcation for transverse forces occur much earlier for clamped beams.

The stretch energies are similar to the vertical graphs in that they also have a bifurcation point which can be clearly seen. On the other hand, bending energies seem to depart in a smoother way. It is also interesting that the non-physical energy graphs assume identical forms, differing only by their scales, whereas this is not true for their physical counterparts.

Chapter 5

Conclusion and Future Work

The aim of this study was two-fold: in the first part, we analyzed silver nanowires' varying effective Young's Modulus as a function of diameter at the presence vertical forces. In the second part, we derived a model for nonlinear beam buckling and displayed the snap-through phenomenon. In order to perform these analyses, the surface and curve model extensions of continuum mechanics were implemented in a finite element setting and the derived buckling formulation was implemented in an ordinary differential equation solver.

Modeling the oxidation layers of a silver nanowire with surface parameters has shown that the trend of growing Young's Modulus with decreasing diameter can be replicated numerically without modeling the coatings in 3-D. Incorporating curves has shown a deficit of the theory: since the curves show no resistance against shear, the ratio of shear to bending stiffness rapidly decreases. In this case, on has to resort to Timoshenko's beam theory to compute effective Young's Modulus. The reason this is considered as a backdraw is that in nanowires and beams, oxidation layers bond with the beams thus it cannot be said that they do not support shear stresses. Similar behavior was also observed with surface layers to some extent in which case the top and bottom parts which contribute the most to bending stiffness do not support shear forces.

In the last chapter a nonlinear beam buckling model was derived based on material linearity and geometric nonlinearity assumptions. The model derived has some advantageous differences from similar formulations that allows the implementation of a robust solver. The solutions obtained by utilization of this solver was compared to the finite element model results. The comparisons were performed on double clamped silicon nanobeams both with and without silicon dioxide surface layers. The results were found to match perfectly, confirming the validity of the buckling theory. Moreover, the bifurcation points on the snap through problem were demonstrated. The lower energetic bifurcation behavior were demonstrated for both double clamped and double hinged beams.

Future works will include retrieval of shear correction factor numerically for surfaces. The ODE solver will be modified to accept mixed boundary conditions, distributed vertical load and most importantly implementing fixed force application positions in the deformed configuration.

Bibliography

[1] A. K. Naik, M. S. Hanay, W. K. Hiebert, X. L. Feng, and M. L. Roukes, "Towards single-molecule nanomechanical mass spectrometry," *Nature Nanotechnology*, vol. 4, no. 7, pp. 445–450, 2009.

[2] J. He and C. M. Lilley, "Surface effect on the elastic behavior of static bending nanowires," *Nano Letters*, vol. 8, no. 7, pp. 1798–1802, 2008.

[3] S. Cuenot, C. Frétigny, S. Demoustier-Champagne, and B. Nysten, "Surface tension effect on the mechanical properties of nanomaterials measured by atomic force microscopy," *Physical Review B*, vol. 69, no. 16, p. 165410, 2004.

[4] B. Charlot, W. Sun, K. Yamashita, H. Fujita, and H. Toshiyoshi, "Bistable nanowire for micromechanical memory," *Journal of Micromechanics and Microengineering*, vol. 18, no. 4, 2008.

[5] M. Taher A. Saif, "On a tunable bistable MEMS-theory and experiment," *Journal of Microelectromechanical Systems*, vol. 9, no. 2, pp. 157–170, 2000.

[6] A. Javili and P. Steinmann, "A finite element framework for continua with boundary energies. Part I: The two-dimensional case," *Computer Methods in Applied Mechanics and Engineering*, vol. 198, no. 27-29, pp. 2198–2208, 2009.

[7] A. Javili and P. Steinmann, "A finite element framework for continua with boundary energies. Part II: The three-dimensional case," *Computer Methods in Applied Mechanics and Engineering*, vol. 199, no. 9-12, pp. 755–765, 2010.

[8] A. Javili, A. McBride, P. Steinmann, and B. D. Reddy, "A unified computational framework for bulk and surface elasticity theory: A curvilinear-coordinate-based finite element methodology," *Computational Mechanics*, vol. 54, no. 3, pp. 745–762, 2014.

[9] A. Javili and P. Steinmann, "On thermomechanical solids with boundary structures," *International Journal of Solids and Structures*, vol. 47, no. 24, pp. 3245–3253, 2010.

[10] P. Steinmann, "On boundary potential energies in deformational and configurational mechanics," *Journal of the Mechanics and Physics of Solids*, vol. 56, no. 3, pp. 772–800, 2008.

[11] A. De Coninck, B. De Baets, D. Kourounis, F. Verbosio, O. Schenk, S. Maenhout, and J. Fostier, "Needles: Toward large-scale genomic prediction with marker-by-environment interaction," vol. 203, no. 1, pp. 543–555, 2016.

[12] F. Verbosio, A. D. Coninck, D. Kourounis, and O. Schenk, "Enhancing the scalability of selected inversion factorization algorithms in genomic prediction," *Journal of Computational Science*, vol. 22, no. Supplement C, pp. 99 – 108, 2017.

[13] D. Kourounis, A. Fuchs, and O. Schenk, "Towards the next generation of multiperiod optimal power flow solvers," *IEEE Transactions on Power Systems*, vol. PP, no. 99, pp. 1–10, 2018.

[14] P. R. Amestoy, A. Guermouche, J. Y. L'Excellent, and S. Pralet, "Hybrid scheduling for the parallel solution of linear systems," *Parallel Computing*, vol. 32, no. 2, pp. 136–156, 2006.

[15] J. Koster, "A fully asynchronous multifrontal solver using distributed dynamic scheduling," vol. 23, no. 1, pp. 15–41, 2001.

[16] K. Kupper, M. Frank, and S. Jin, "Viennacl—linear algebra library for multi- and many-core architectures," *SIAM Journal on Numerical Analysis*, vol. 54, no. 1, pp. 440–461, 2016.

[17] G. Y. Jing, H. L. Duan, X. M. Sun, Z. S. Zhang, J. Xu, Y. D. Li, J. X. Wang, and D. P. Yu, "Surface effects on elastic properties of silver nanowires: Contact atomic-force microscopy," *Physical Review B - Condensed Matter and Materials Physics*, vol. 73, no. 23, pp. 1–6, 2006.

[18] M. Ahmer Wadee, *Shear Deformable Beams and Plates: Relationships with Classical Solutions*, vol. 23. 2001.

[19] G. R. Cowper, "The Shear Coefficient in Timoshenko's Beam Theory," *Journal of Applied Mechanics*, vol. 33, no. 2, p. 335, 1966.

[20] Y. Chen, B. L. Dorgan, D. N. McIlroy, and D. E. Aston, "On the importance of boundary conditions on nanomechanical bending behavior and elastic modulus determination of silver nanowires," *Journal of Applied Physics*, vol. 100, no. 10, 2006.

[21] G. F. Wang and X. Q. Feng, "Effects of surface elasticity and residual surface tension on the natural frequency of microbeams," *Applied Physics Letters*, vol. 90, no. 23, pp. 1–4, 2007.

[22] C. Maurini, J. Pouget, and S. Vidoli, "Distributed piezoelectric actuation of a bistable buckled beam," *European Journal of Mechanics, A/Solids*, vol. 26, no. 5, pp. 837–853, 2007.

[23] W. Fang and J. A. Wickert, "Post buckling of micromachined beams," *Journal of Micromechanics and Microengineering*, vol. 4, no. 3, pp. 116–122, 1994.

[24] J. Zhao, J. Jia, X. He, and H. Wang, "Post-buckling and Snap-Through Behavior of Inclined Slender Beams," *Journal of Applied Mechanics*, vol. 75, no. 4, p. 041020, 2008.

[25] Y. L. Pi and N. S. Trahair, "Non-linear buckling and postbuckling of elastic arches," *Engineering Structures*, vol. 20, no. 7, pp. 571–579, 1998.

[26] B. Camescasse, A. Fernandes, and J. Pouget, "Bistable buckled beam and force actuation: Experimental validations," *International Journal of Solids and Structures*, vol. 51, no. 9, pp. 1750–1757, 2014.

[27] B. Camescasse, A. Fernandes, and J. Pouget, "Bistable buckled beam: Elastica modeling and analysis of static actuation," *International Journal of Solids and Structures*, vol. 50, no. 19, pp. 2881–2893, 2013.

[28] A. C. Hindmarsh, P. N. Brown, K. E. Grant, S. L. Lee, R. Serban, D. E. Shumaker, and C. S. Woodward, "SUNDIALS: Suite of nonlinear and differential/algebraic equation solvers," *ACM Transactions on Mathematical Software (TOMS)*, vol. 31, no. 3, pp. 363–396, 2005.

[29] H. Zhang, J. Tersoff, S. Xu, H. Chen, Q. Zhang, K. Zhang, Y. Yang, C. S. Lee, K. N. Tu, J. Li, and Y. Lu, "Approaching the ideal elastic strain limit in silicon nanowires," *Science Advances*, vol. 2, no. 8, pp. 2–10, 2016.

[30] J. Qiu, J. H. Lang, and A. H. Slocum, "A centrally-clamped parallel-beam bistable MEMS mechanism," *Proceedings of the IEEE Micro Electro Mechanical Systems (MEMS)*, no. 5, pp. 353–356, 2001.

[31] M. Vangbo, "An analytical analysis of a compressed bistable buckled beam," *Sensors and Actuators, A: Physical*, vol. 69, no. 3, pp. 212–216, 1998.

[32] I. M. Gelfand and S. V. Fomin, "Calculus of Variations," p. 232, 1963.

Appendix A

Functional variation

This appendix is a brief collection of information on functional derivatives. One may refer to [32] for a more in depth introduction.

Let X be a normed vector space over $\mathbb{R}$. The *(Frechet) derivative* of a functional $J : X \to \mathbb{R}$ is said to exist at a point $x \in X$ if

$$\lim_{h \to 0} \frac{J(x+h) - J(x) - A_x(h)}{\|h\|} = 0 \tag{A.1}$$

is satisfied for some bounded linear map $A_x : X \to \mathbb{R}$. In this case, the linear map A_x is the *(Frechet) derivative* of J at point x.

The fact that the variation of a functional at a point is unique is trivial. The position subscript attached to the derivative exists to remind the reader that while the derivative is unique as a bounded linear map at a point, it indeed depends on the point x.

A functional J may not necessarily have a derivative at a point but it might have derivatives along directions h, which allow one to define a linear functional. In this case, the Gateaux derivative is defined as such:

Let $J : X \to \mathbb{R}$ be a functional. If a linear map $B : X \to \mathbb{R}$ satisfies the

condition

$$\lim_{\lambda \to 0} \frac{J(x + \lambda h) - J(x) - \lambda B(h)}{\lambda} = 0 \tag{A.2}$$

for every $h \neq 0$, $h \in X$, then J is said to be *Gateaux differentiable* at x, and B is its *Gateaux derivative*.

The existence of *(Frechet)* derivative of a functional implies its continuity but the same cannot be said for Gateaux derivative. That is, a functional might have a Gateaux derivative at a point x, yet still be discontinuous at x. This fact would persist even if we assumed that Gateaux derivatives are bounded. The result is akin to the finite dimensional case where the existence of directional derivatives do not imply continuity of a function.

If a functional J has a derivative A_x at a point $x \in X$ then its Gateaux derivative at x also exists and moreover $A = B$. The proof is simple. Assume that the derivative of J at x, A exists. Then one has that, for any fixed $h \in X$

$$\begin{aligned} 0 = \lim_{\lambda \to 0} \frac{J(x + \lambda h) - J(x) - A_x(\lambda h)}{\|\lambda h\|} &= \lim_{\lambda \to 0} \frac{J(x + \lambda h) - J(x) - \lambda\, A_x(h)}{|\lambda| \cdot \|h\|} \\ &= \frac{1}{\|h\|} \lim_{\lambda \to 0} \frac{J(x + \lambda h) - J(x) - \lambda\, A_x(h)}{|\lambda|} \end{aligned} \tag{A.3}$$

then the desired result is obtained, where the derivative A_x is equal to the Gateaux derivative B_x.

In this thesis, the derivative of a functional J at the point x acted on h is denoted as $\delta J(x, h)$. Since the direction h is viewed as a virtual increment in the context of mechanics, it is replaced with δx, resulting in the expression $\delta J(x, \delta x)$. Because δJ has to be also equal to the Gateaux derivative, computing the general derivative is not difficult. This is because

$$\lim_{\lambda \to 0} \frac{J(x + \lambda \delta x) - J(x)}{\lambda} = \delta J(x, \delta x) \tag{A.4}$$

due to equation (A.2). Then assuming that the derivative exists, computing it is a rather straightforward task.

Appendix B

Surface and curve tension

Some surface and curve tension examples can be found in this appendix.

In figure B.1, the effect that increasing surface tension has over the deformation of the material can be observed. Note that the configurations presented in this appendix are pre-stressed. The net effect of surface tension is area minimization which can be clearly seen in the figures.

In figure B.2, the additional effects of curve tension can be observed. As the ratio of curve to surface tension increases, the shrinking on the edges become more pronounced.

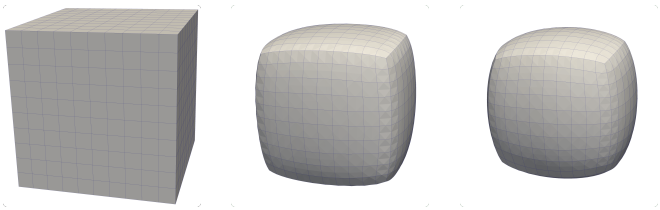

(a) $\widehat{\gamma}/\mu = 0$ (b) $\widehat{\gamma}/\mu = 0.2$ (c) $\widehat{\gamma}/\mu = 0.4$

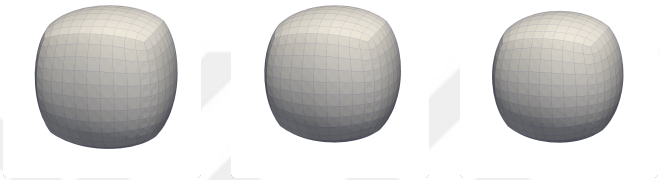

(d) $\widehat{\gamma}/\mu = 0.6$ (e) $\widehat{\gamma}/\mu = 0.8$ (f) $\widehat{\gamma}/\mu = 1$

Figure B.1: Effect of increasing surface tension $\widehat{\gamma}$ with fixed μ.

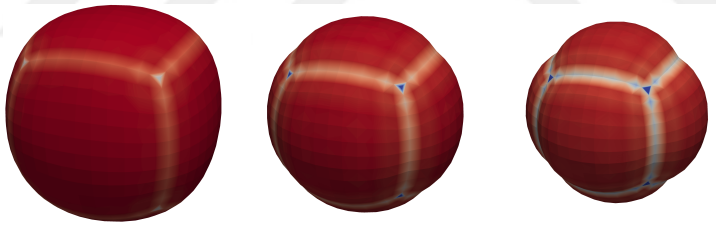

(a) 1 : 0.3 : 0.15 (b) 1 : 0.6 : 0.3 (c) 1 : 0.9 : 0.45

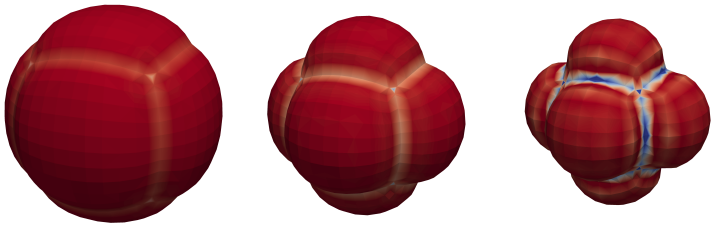

(d) 1 : 0.3 : 0.3 (e) 1 : 0.6 : 0.6 (f) 1 : 0.9 : 0.45

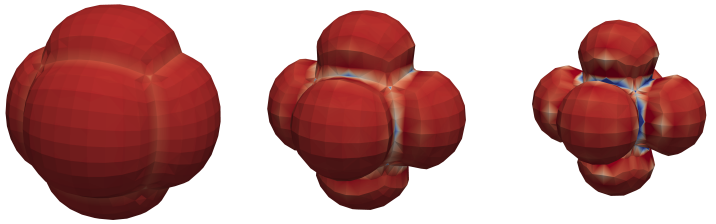

(g) 1 : 0.3 : 0.45 (h) 1 : 0.3 : 0.9 (i) 1 : 0.9 : 1.35

Figure B.2: Effect of increasing surface and curve tensions $\widehat{\gamma}$, $\widetilde{\gamma}$ with fixed μ. Ratios denote the quantity $\mu : \widehat{\gamma} : \widetilde{\gamma}$. Color map depicting $\mathrm{tr}(\boldsymbol{P})$.

Appendix C

Main function of the FEM code

This part includes the main function of the program used along with brief explanations to give the reader a general idea of the structure of the code.

```
#include <cstdio>
#include <vector>

#include "global_vars.hpp"

#include "element.hpp"
#include "node.hpp"
#include "edge.hpp"
#include "face.hpp"

#include "add_to_node.hpp"
#include "set_neighbours.hpp"
#include "create.hpp"
#include "face_edge.hpp"
#include "mesh_info.hpp"
#include "get_mesh.hpp"
#include "disp_element_info.hpp"
#include "write_info.hpp"
#include "set_boundary_conditions.hpp"
#include "set_dof.hpp"
#include "fem_solve.hpp"

int main() {

        /*
           1. First, vector that holds node coordinates and element relations are created,
                   get_mest reads the mesh file and sets the node coordinates and element-node
                   info
         */
        std::vector<std::vector<double> > node_coor(total_node, std::vector<double>(NDIM));
        std::vector<std::vector<int> > element_node(total_elem, std::vector<int>(NPE));

        get_mesh(file_name, NDIM, total_elem, total_node, NPE, node_coor, element_node);

        std::vector<Element> ElementList;
```

```
        std::vector<Node> NodeList;
        std::vector<Edge> EdgeList;
        std::vector<Face> FaceList;
        for (int i = 0; i < total_elem; ++i){
                ElementList.push_back(Element(element_node[i]));
        }
        for (int i = 0; i < total_node; ++i){
                NodeList.push_back(Node(node_coor[i]));
        }

        /*
           2. Next step is to set the topology. Each node is assigned to hold the info
              of all elements that it belongs to. Then using this neighbours of elements
              are set. This is an important step in order to preserve efficiency in the
              next procedures. The edge and face info are created, and these hold similar
              members to elements. The nodes are also updated with the addition of edge
              and faces. After face_edge() is called, the topology is set.
         */
        add_elem_to_node(ElementList, NodeList);
        set_neighbours(ElementList, NodeList);
        create_edges(mesh_type, NPG, ElementList, EdgeList);
        create_faces(mesh_type, NPF, ElementList, FaceList);
        add_edge_to_node(EdgeList, NodeList);
        add_face_to_node(FaceList, NodeList);
        face_edge(EdgeList, FaceList, NodeList);


        /*
           3. The global degree of freedoms (dof) and constraints (doc) are set after
           set_boundary_condition() is called. The set_boundary_conditions() function sets the
           global degree of freedoms while eliminating the constraints that are there due
           to displacement type boundary conditions. bulk_dof and surface_dof are the number
           of degrees of freedoms of the post-processing FEM code that finds the scalar field
           on the nodes which minimizes 2-norm distance to the actual solution found.
           fem_solve() sets up the assembly and linear solver routines.
         */
        int dof, doc;
        int bulk_dof, surface_dof;.

        set_boundary_conditions(NodeList, FaceList, EdgeList);
        set_dof(NDIM, &dof, &doc, &bulk_dof, &surface_dof, NodeList, FaceList);
        fem_solve(&postprocess, dof, doc, bulk_dof, surface_dof, ElementList,\
                        NodeList, FaceList, EdgeList);
        write_solution_mesh(ElementList, NodeList);

        /*
           3. The solutions are converted into .vtk files in this stage. At this stage the
              problem is solved, and postprocessing files are ready to be generated.
              First routine generates a 3D .vtk file with 3D bulk elements, while the latter
              generates a 3D .vtk file with 2D surface elements.
         */
        write_solution_mesh_paraview(1, ElementList, FaceList, NodeList);
        write_solution_mesh_paraview_surface(FaceList, NodeList);
    return 0;
}
```